Cell

Article

Glioblastoma hijacks neuronal mechanisms for brain invasion

Graphical abstract

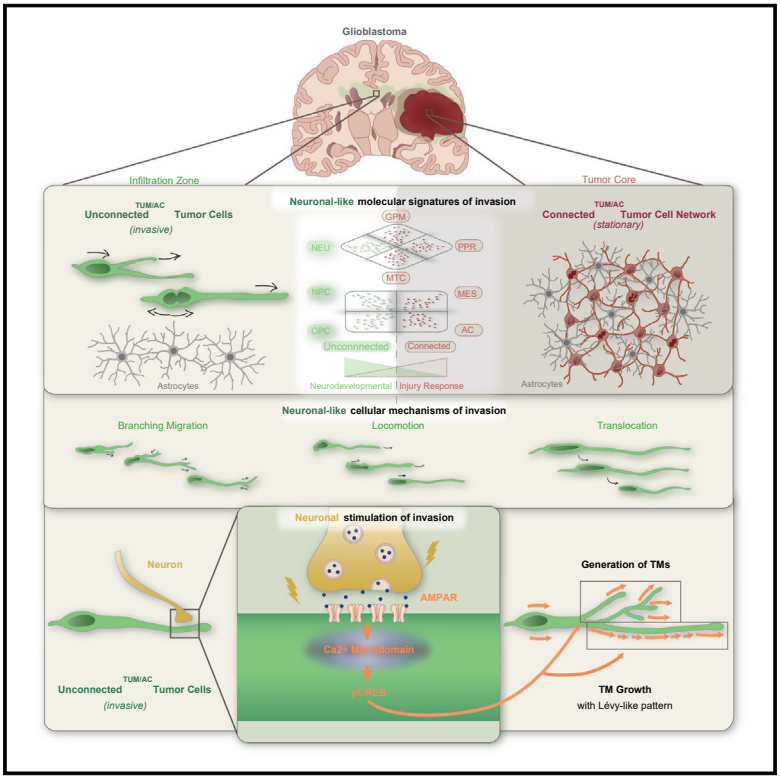

Highlights

- Molecular glioblastoma cell states are related to cell functions
- Neuronal-like, single-glioblastoma cells drive brain invasion
- Glioblastoma invasion resembles multiple traits of neuronal development
- Neurogliomal synapses stimulate neurite-like tumor microtubes crucial for invasion

Authors

Varun Venkataramani, Yvonne Yang, Marc Cicero Schubert, ..., Wolfgang Wick, Thomas Kuner, Frank Winkler

Correspondence

varun.venkataramani@med.uni-heidelberg.de (V.V.), thomas.kuner@uni-heidelberg.de (T.K.), frank.winkler@med.uni-heidelberg.de (F.W.)

In brief

Glioblastoma cells with neuronal features drive brain invasion.

Venkataramani et al., 2022, Cell *185*, 2899–2917
August 4, 2022
https://doi.org/10.1016/j.cell.2022.06.054

CellPress

Cell

CellPress

Article

Glioblastoma hijacks neuronal mechanisms for brain invasion

Varun Venkataramani,[1,2,3,*] Yvonne Yang,[3,11] Marc Cicero Schubert,[2,11] Ekin Reyhan,[3] Svenja Kristin Tetzlaff,[2] Niklas Wißmann,[2] Michael Botz,[2] Stella Judith Soyka,[2] Carlo Antonio Beretta,[2] Rangel Lyubomirov Pramatarov,[2] Laura Fankhauser,[3] Luciano Garofano,[4] Alexander Freudenberg,[5] Julia Wagner,[2] Dimitar Ivanov Tanev,[1,2] Miriam Ratliff,[3,6] Ruifan Xie,[1,3] Tobias Kessler,[1,3] Dirk C. Hoffmann,[1,3,7] Ling Hai,[1,3] Yvette Dörflinger,[2] Simone Hoppe,[2] Yahaya A. Yabo,[8] Anna Golebiewska,[8] Simone P. Niclou,[8] Felix Sahm,[9,10] Anna Lasorella,[4] Martin Slowik,[5] Leif Döring,[5] Antonio Iavarone,[4] Wolfgang Wick,[1,3] Thomas Kuner,[2,12,*] and Frank Winkler[1,3,12,13,*]

[1]Neurology Clinic and National Center for Tumor Diseases, University Hospital Heidelberg, 69120 Heidelberg, Germany
[2]Department of Functional Neuroanatomy, Institute for Anatomy and Cell Biology, Heidelberg University, 69120 Heidelberg, Germany
[3]Clinical Cooperation Unit Neurooncology, German Cancer Consortium (DKTK), German Cancer Research Center (DKFZ), 69120 Heidelberg, Germany
[4]Institute for Cancer Genetics, Columbia University Medical Center, New York, NY 10027, USA
[5]Institute of Mathematics, University of Mannheim, 68131 Mannheim, Germany
[6]Neurosurgery Clinic, University Hospital Mannheim, 68167 Mannheim, Germany
[7]Faculty of Biosciences, Heidelberg University, 69120 Heidelberg, Germany
[8]NORLUX Neuro-Oncology Laboratory, Department of Cancer Research, Luxembourg Institute of Health, 1526 Luxembourg, Luxembourg
[9]Department of Neuropathology, Institute of Pathology, University Hospital Heidelberg, 69120 Heidelberg, Germany
[10]Clinical Cooperation Unit Neuropathology, German Cancer Consortium (DKTK), German Cancer Research Center (DKFZ), 69120 Heidelberg, Germany
[11]These authors contributed equally
[12]These authors contributed equally
[13]Lead contact
*Correspondence: varun.venkataramani@med.uni-heidelberg.de (V.V.), thomas.kuner@uni-heidelberg.de (T.K.), frank.winkler@med.uni-heidelberg.de (F.W.)
https://doi.org/10.1016/j.cell.2022.06.054

SUMMARY

Glioblastomas are incurable tumors infiltrating the brain. A subpopulation of glioblastoma cells forms a functional and therapy-resistant tumor cell network interconnected by tumor microtubes (TMs). Other subpopulations appear unconnected, and their biological role remains unclear. Here, we demonstrate that whole-brain colonization is fueled by glioblastoma cells that lack connections with other tumor cells and astrocytes yet receive synaptic input from neurons. This subpopulation corresponds to neuronal and neural-progenitor-like tumor cell states, as defined by single-cell transcriptomics, both in mouse models and in the human disease. Tumor cell invasion resembled neuronal migration mechanisms and adopted a Lévy-like movement pattern of probing the environment. Neuronal activity induced complex calcium signals in glioblastoma cells followed by the *de novo* formation of TMs and increased invasion speed. Collectively, superimposing molecular and functional single-cell data revealed that neuronal mechanisms govern glioblastoma cell invasion on multiple levels. This explains how glioblastoma's dissemination and cellular heterogeneity are closely interlinked.

INTRODUCTION

Glioblastomas (GBs) are incurable brain tumors characterized by their cellular heterogeneity (Garofano et al., 2021; Neftel et al., 2019), invasion, and colonization of the entire brain (Drumm et al., 2020; Sahm et al., 2012), rendering these tumors incurable. GBs also show considerable resistance against standard-of-care treatment with radio- and chemotherapy as well as surgical resection (Wick et al., 2018). A large subpopulation of GB cells (GBCs) can organize in networks where they are connected with each other via ultralong and thin membrane protrusions, tumor microtubes (TMs), that are the anatomical basis of a highly functional tumor cell network coupled via gap junctions. This network is a key mediator of therapeutic resistance (Osswald et al., 2015; Weil et al., 2017). Furthermore, neuronal activity—via paracrine signaling and glutamatergic synapses that are formed onto GBC networks—can activate these networks and are associated with increased tumor cell proliferation and invasion (Venkataramani et al., 2019; Venkatesh et al., 2015, 2017, 2019). This could imply that mutually connected GBCs also drive

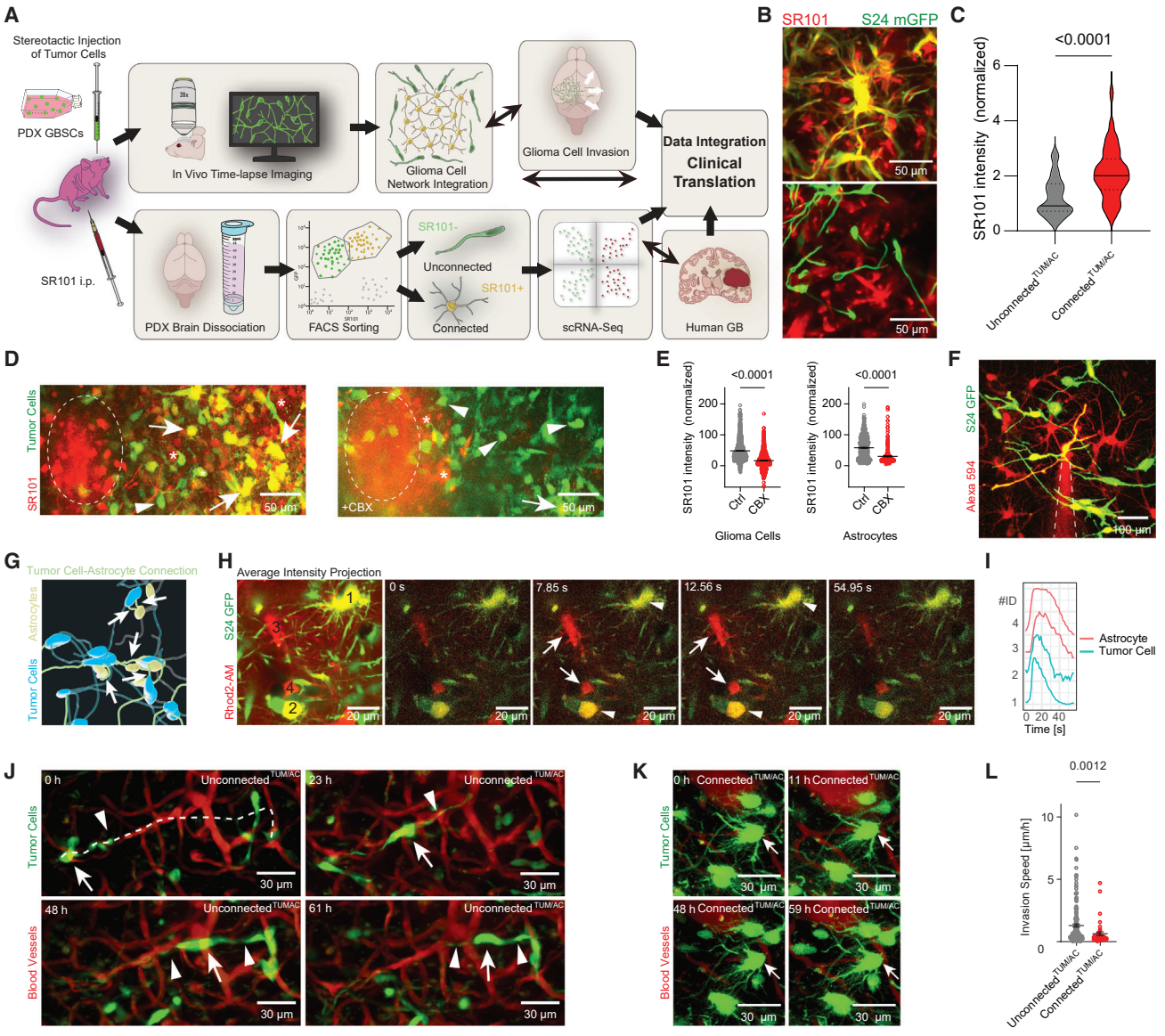

Figure 1. GBCs unconnected to other tumor cells or astrocytes drive tumor invasion

(A) Scheme of the multidimensional analysis workflow.

(B) Intravital two-photon microscopy (IV2PM) of tumor-connected GBCs (yellow, SR101 and GFP), tumor-unconnected GBCs (green, only GFP) and astrocytes (red, only SR101). Post-processed with enhance.ai.

(C) Normalized SR101 gray values per dataset as shown in (B) (n = 125 GBCs from 4 mice, Mann-Whitney test).

(D) IV2PM of SR101 uptake after microinjection into the brain without (left) and with (right) simultaneous carbenoxolone (CBX) microinjection (circle). Arrows = SR101+/connected$^{TUM/AC}$ GBCs (yellow), arrowheads = SR101−/unconnected$^{TUM/AC}$ GBCs (green), asterisks = brain astrocytes (red).

(E) Normalized SR101 gray values per dataset as shown in (D) (n = 2,374 GBCs and n = 807 astrocytes from 3 mice, Mann-Whitney test).

(F) Confocal image of GFP-positive GBCs in neuron/astrocyte co-culture. Unconnected$^{TUM/AC}$ (green), connected$^{TUM/AC}$ GBCs (yellow), astrocytes (red), Alexa-594-filled micropipette (dashed lines).

(G) IV2PM 3D rendering (z dimension = 90 µm). Tumor cell somata (blue), astrocyte somata (yellow), tumor-astrocyte connections via TM (green, arrows), tumor-tumor connections via TM (light blue), astrocytic protrusions (gray).

(H) IV2PM time-lapse calcium imaging of GBCs and astrocytes. GBCs (green, 1 and 2), astrocytes (red, 3 and 4), calcium transients in astrocytes (arrows), calcium transients in GBCs (arrowheads).

(I) Representative calcium traces of a co-active calcium wave in tumor cells (1, 2) and astrocytes (3, 4) from (H).

(J) 61h IV2PM time-lapse imaging of a morphologically unconnected$^{TUM/AC}$ GBC (green, arrow), blood vessels (red), TM (arrowheads), invasion route (dashed line). Representative of 5 experiments in 5 mice. Post-processed with denoise.ai and "remove outliers" function in ImageJ/Fiji.

(K) 59h IV2PM time-lapse of a morphologically connected$^{TUM/AC}$ stationary GBC (arrow, green).

(legend continued on next page)

invasion (Gritsenko et al., 2020), similar to collective migration in other cancer entities (Friedl et al., 2012). Alternative current models describe GBC invasion along blood vessels, nerve and astrocytic tracts, and diffusely through the extracellular matrix (Cuddapah et al., 2014). In light of these data, two important questions remain: what are the mechanisms of GB brain invasion? And what is the role of GBCs not connected to other tumor cells? How the latter contribute to tumor progression and interact with other cells of the tumor microenvironment, such as astrocytes and neurons, remains unclear.

The heterogeneous molecular composition of GBCs has been recently classified using pathway-based and gene-expression-based cell states (Garofano et al., 2021; Neftel et al., 2019; Richards et al., 2021; Wang et al., 2019a). It remains an open question how these molecular cell states are related to tumor biology, which includes the recently discovered neuronal GBC state (Garofano et al., 2021). Particularly, how those GBC states are functionally related to tumor cell connectivity and ability to invade the normal brain is unclear. In addition, it is still controversial what kind of trajectories brain tumor cell states follow (Chaligne et al., 2021; Wang et al., 2019a) and how these cell states might change with disease progression.

Here, we integrate molecular and functional states of GBCs to lay the ground for insights into multidimensional tumor cell heterogeneity and its relation to multicellular connectivity and propensity of brain invasion. Longitudinal time-lapse imaging of migrating GBCs *in vivo* revealed that single GBCs lacking connections to other GBCs and astrocytes are main drivers of diffuse brain tumor invasion. These GBCs were enriched for neuronal, neural-progenitor-like, and non-mesenchymal-like (MES-like) cell states. Infiltrative regions enriched with such tumor cell and astrocyte-unconnected, invasive GBCs transition over time into regions with predominantly tumor cell and astrocyte-connected, stable GBC networks. GBC invasion resembled mechanisms of neuronal migration during development. Lastly, activation of glutamatergic neurogliomal synapses increased GBC invasiveness by stimulating the formation and dynamics of TMs. In summary, three layers of neuronal features governing GBC invasion illustrate parallels between brain development and incurable GB.

RESULTS

GB networks are functionally connected to astrocytic networks

To comprehensively characterize intratumoral heterogeneity, we established a workflow integrating longitudinal 3D *in vivo* imaging of patient-derived human GBCs in the living mouse with single-cell RNA sequencing (scRNA-seq) data (Figure 1A, patient-derived gliobastoma xenograft [PDX] models and human GB from resected tissue; Figure S1A; Table S1). GBCs were separated into two groups based on their *in vivo* uptake of the gap junction-permeable dye SR101 (Nimmerjahn et al., 2004): GBCs that were anatomically connected with each other via TMs and gap junctions (Osswald et al., 2015) took up SR101 and dynamically spread it across the tumor cell network, while GBCs lacking anatomical connections barely took up SR101 (Figures 1B and 1C). These mutually connected GBCs showed multicellular co-active calcium events indicating functional connectivity across this GBC subpopulation, while calcium events remained local in GBCs not exhibiting connecting TMs suggesting that they are disconnected from other GBCs (Figures S1B–S1D). SR101 accumulated rapidly in astrocytes after intraperitoneal injection while a subpopulation of neighboring GBCs was stained after a delay (Figures S1E–S1H). After injection into tumor microregions, SR101 was taken up both by astrocytes and GBCs, which was inhibited by pharmacological gap junction blockade (Figures 1D and 1E). To further confirm gap junctional coupling of GBCs with each other, with astrocytes, or with both (from here on termed "connected$^{TUM/AC}$"), single GBCs expressing GFP were filled with Alexa 594 via whole-cell patch-clamp recordings performed in co-cultures. This gap junction-permeable dye was dynamically distributed to GBCs and to morphologically distinct astrocytes not expressing GFP (Figures 1F, S1I, and S1J). Consistent with gap junctional coupling, connected$^{TUM/AC}$ GBCs had a significantly decreased input resistance as compared with unconnected$^{TUM/AC}$ GBCs (McKhann et al., 1997; Figure S1K). This coupling was reflected in TM-mediated morphological connectivity between GBCs and astrocytes *in vitro* and *in vivo* (Figures 1G and S1L). To test whether these two cell populations were also functionally coupled, astrocytes and GBCs were loaded with Rhod-2AM applied at the brain surface. Subsequent intravital calcium imaging revealed co-active events in astrocytes and GBCs (Figures 1H and 1I), indicating functional coupling of a GBC subpopulation with astrocytes. In summary, GBCs are not only gap-junction-connected among themselves, but also with astrocytes. The discovery of this GB-astrocyte network extends the tumor network concept: from a purely homotypic to an even larger, heterotypic, connected$^{TUM/AC}$ network.

Unconnected$^{TUM/AC}$ GBCs are the main drivers of tumor invasion

By functionally separating connected$^{TUM/AC}$ and unconnected$^{TUM/AC}$ GBCs, we first sought to define which of them drive diffuse brain colonization. Time-lapse intravital two-photon microscopy revealed that unconnected$^{TUM/AC}$ GBCs are invasive, whereas connected$^{TUM/AC}$ GBCs remained mostly stationary (Figures 1J and 1K). Migration speed significantly differed in connected$^{TUM/AC}$ (as evidenced by SR101 uptake or by morphological connectivity) versus unconnected$^{TUM/AC}$ GBCs (Figures 1L and S1M–S1O), demonstrating that GB invasion is dominated by unconnected$^{TUM/AC}$ GBCs.

Invasive GBCs harbor neural gene expression signatures

To molecularly characterize these functionally distinct tumor cell subpopulations, GFP/SR101-labeled GBCs were isolated using

(L) GBC invasion speed over 4 h for SR101+/connected$^{TUM/AC}$ and SR101−/unconnected$^{TUM/AC}$ GBCs (n = 167 unconnected$^{TUM/AC}$ and n = 40 connected$^{TUM/AC}$ GBCs from 9 mice, Mann-Whitney test).

(C, E, and L) Data represented as mean ± SEM. S24 GBCs used for all experiments.

See also Figure S1 and Table S1.

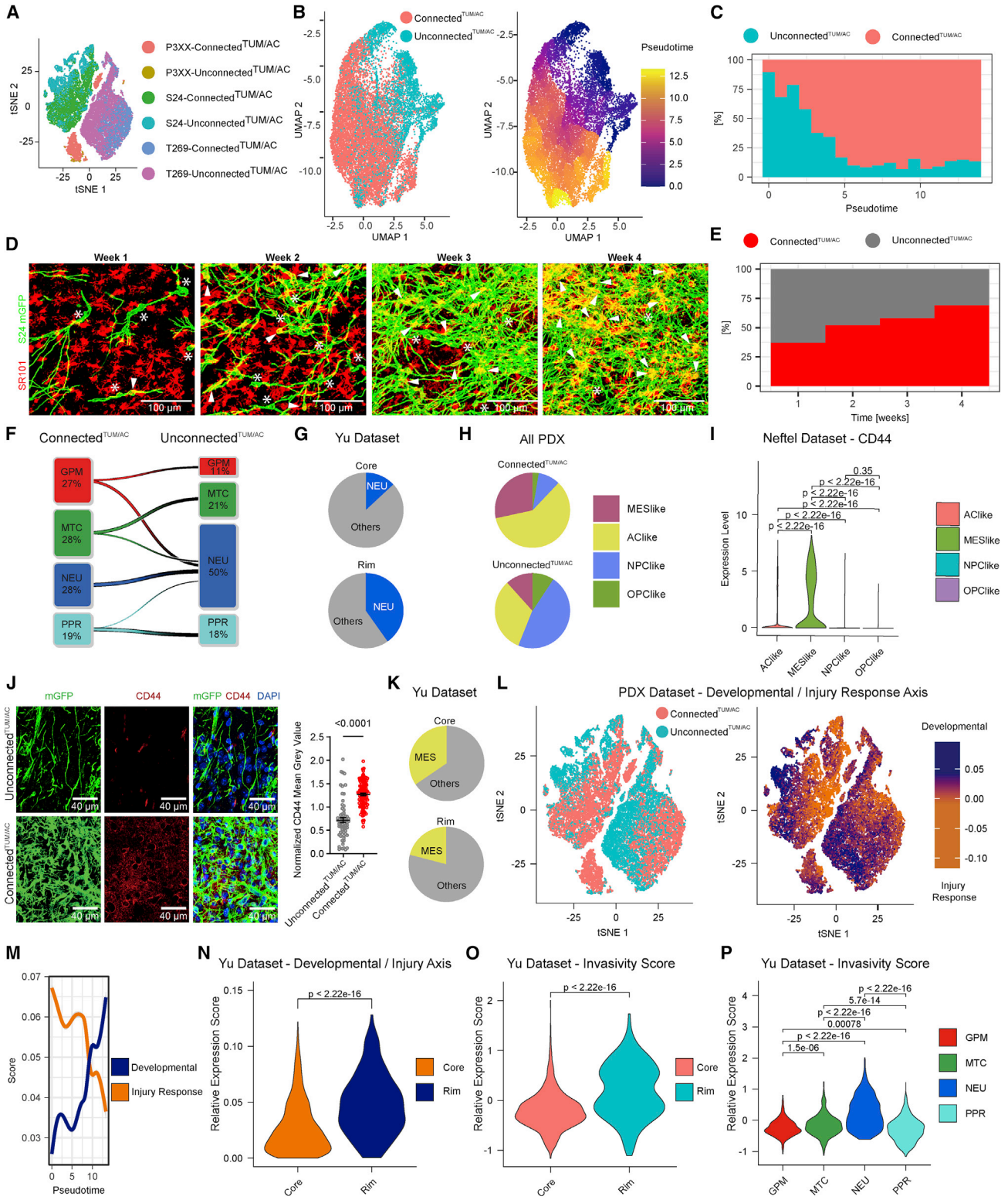

Figure 2. Neuronal-like cell states govern brain tumor invasion

(A) tSNE plot of cells sorted according to SR101 uptake into connected$^{TUM/AC}$ or unconnected$^{TUM/AC}$ GBCs.

(B) UMAP plot comparing connected$^{TUM/AC}$ and unconnected$^{TUM/AC}$ GBCs (left) and pseudotime (right).

(C) Bar plot of connected$^{TUM/AC}$ and unconnected$^{TUM/AC}$ GBCs based on pseudotime.

(legend continued on next page)

cell sorting and submitted to scRNA-seq (Hai et al., 2021). Connected$^{TUM/AC}$ and unconnected$^{TUM/AC}$ GBCs could be distinguished by their gene expression profiles in three PDX models (Figures 2A and S2A–S2D). To quantitatively characterize changes in cellular transcriptional programs in the context of potential temporal trajectories between connected$^{TUM/AC}$ and unconnected$^{TUM/AC}$ GBCs, they were sorted according to pseudotime (Cao et al., 2019). In all three PDX models used here, transcriptional changes appear along the axis from unconnected$^{TUM/AC}$ to connected$^{TUM/AC}$ GBCs (Figures 2B, 2C, and S2E–S2H). However, this approach does not allow to infer a directionality of the respective trajectories. Therefore, longitudinal intravital two-photon imaging (IV2PM) was used to follow invasion and network formation in a defined brain area at the rim of the tumor (Figure 2D). Quantitative analysis confirmed an increase of connected$^{TUM/AC}$ cells over time and with increasing tumor cell density (Figures 2E and S2I–S2Q; Video S1). Taken together, combined scRNA-seq and IV2PM suggest a concept of how brain colonization is achieved by brain tumors: unconnected$^{TUM/AC}$ GBCs are taking the lead, colonize new brain regions, and over time interconnect with other GBCs and astrocytes, transitioning to connected$^{TUM/AC}$ GBCs.

Next, we superimposed intravital imaging and scRNA-seq results to identify key molecular and functional cellular states driving tumor progression. Unconnected$^{TUM/AC}$ cells were predominately enriched for the neuronal (NEU) (Figures 2F, 2G, and S2R; Garofano et al., 2021) and the oligodendrocyte precursor-like (OPC-like)/neural precursor-like (NPC-like) cell states (Figures 2H–2K and S2S; Neftel et al., 2019), and neurodevelopmental transcriptional signatures (Richards et al., 2021; Figures 2F, 2L–2N, and S2T). In contrast, connected$^{TUM/AC}$ GBCs were enriched for the non-neuronal cell states (glycolytic/plurimetabolic [GPM], mitochondrial [MTC], proliferative/progenitor [PPR]) (Garofano et al., 2021; Figure 2F), and astrocyte-like (AC-like)/MES-like cell states (Neftel et al., 2019; Figures 2H–2K and S2S). Furthermore, connected$^{TUM/AC}$ GBCs exhibited an injury response transcriptional signature (Richards et al., 2021) in three different PDX models, confirmed in human scRNA-seq datasets of GB core and infiltration zones (Figures 2L–2N and S2T). The predominance of the neuronal cell state in unconnected$^{TUM/AC}$ GBCs is consistent with an enriched neuronal cell state in the tumor rim versus the core in human GB (Garofano et al., 2021; Yu et al., 2020; Figure 2G). Together, the neuronal cell state coincides with invasion at the infiltration zone.

Accordingly, the mesenchymal marker CD44 (Hara et al., 2021; Neftel et al., 2019) stained high in densely connected$^{TUM/AC}$ GBC regions, but not unconnected$^{TUM/AC}$ ones (Figure 2J), and also in the GB core versus rim (Figure 2K), consistent with an enrichment in MES-like and non-neuronal cell states (Figures 2I and S3A–S3D). This contrasts with work suggesting a major role for the mesenchymal cell state in GBC invasion (Iwadate, 2016) but agrees with early observations that mesenchymal development was accompanied by multicellular network formation via long membrane protrusions (Lewis, 1922). Moreover, the gap junction gene GJA1 was also enriched in non-neuronal cell states (Figures S3E–S3H) and in MES/AC-like cell states, consistent with broad gap junctional coupling found in mesenchymal cells and astrocytes (Bodi et al., 2004; Dorshkind et al., 1993; Valiunas et al., 2004).

In addition, a transcriptional gradient between neurodevelopmental and injury response was linked to molecular GB heterogeneity (Richards et al., 2021). In line with findings showing that connected$^{TUM/AC}$ GBCs increased TM formation and self-repair after surgical lesions, photoablation and radio/chemotherapy (Osswald et al., 2015; Weil et al., 2017), single-cell RNA-seq in PDX models showed a high transcriptional injury signature in connected$^{TUM/AC}$ GBCs, whereas unconnected$^{TUM/AC}$ cells were enriched for a neurodevelopmental transcriptional signature (Figures 2L–2N and S2T).

In conclusion, neuronal, OPC/NPC-like cell states and a neurodevelopmental transcriptional signature were enriched in unconnected$^{TUM/AC}$ GBCs, whereas MES-like, non-neuronal cell states, and a transcriptional injury signature were enriched in connected$^{TUM/AC}$ GBCs.

To define molecular changes occurring during tumor evolution from unconnected$^{TUM/AC}$ to connected$^{TUM/AC}$ cellular states, we

(D) Probability maps of IV2PM of same region over 4 weeks. Unconnected$^{TUM/AC}$ (green, asterisks, SR101-negative) and connected$^{TUM/AC}$ (yellow, arrowhead, SR101-positive) S24 GBCs, astrocytes (red).
(E) Bar plot of average distribution of unconnected$^{TUM/AC}$ and connected$^{TUM/AC}$ S24 GBCs in regions from (D) over 4 weeks (n = 3,169 GBCs in 24 datasets of 6 S24 PDX mice).
(F) River plots from pathway-based cell states including cells analyzed for unconnected $^{TUM/AC}$ and connected$^{TUM/AC}$ GBCs.
(G) Distribution of neuronal cell state in core versus rim.
(H) Pie chart for gene-based cell states for connected$^{TUM/AC}$ and unconnected$^{TUM/AC}$ cells.
(I) CD44 gene expression in Neftel dataset classified according to the gene-based cell states (n = 6,576 cells).
(J) Confocal maximum intensity projection (z = 15 μm) of S24 PDX with CD44 staining (red) and mGFP (green) in mostly unconnected$^{TUM/AC}$ and connected$^{TUM/AC}$ GBC-rich regions. Comparison of normalized staining intensity (n = 164 GBCs from 5 S24 PDX mice, Mann-Whitney test, data are represented as mean ± SEM).
(K) MES-like GBC distribution in human GB core compared with rim.
(L and M) tSNE plots based on their neurodevelopmental and injury response transcriptional signatures with connectivity (L) and plotted against the pseudotime (M).
(N) Neurodevelopmental and injury response signatures in comparison of core and rim.
(O) Invasivity score in single cells of core and rim.
(P) Invasivity score classified according to pathway-based cell states.
Connected$^{TUM/AC}$ GBCs determined by their SR101 uptake (A–F), (H), (L), or by morphological connectivity (J).
(A, F, H, and L) PDX models (S24, P3XX, T269, n = 35,822 GBCs).
(B, C, and M) S24 PDX model (n = 15,269 GBCs).
(G, K, N, O, and P) Yu dataset (n = 2,795 GBCs).
See also Figures S2, S3, and S4, Table S2, and Video S1.

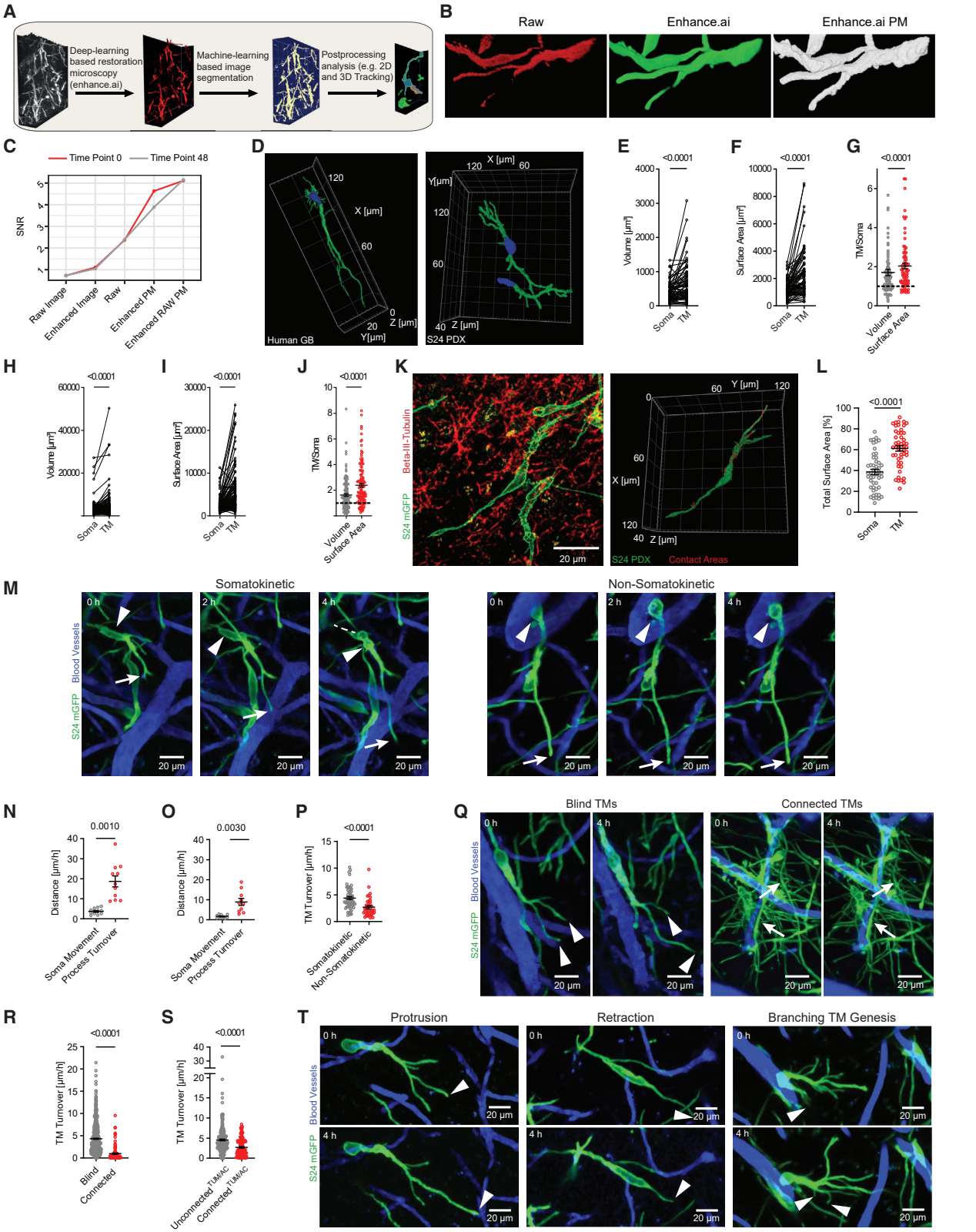

(legend on next page)

derived an invasivity gene expression signature from three PDX models based on genes changing as a function of pseudotime from unconnected$^{TUM/AC}$ to connected$^{TUM/AC}$ cells (Figure S3I; Table S2). This signature was enriched in the tumor rim versus core of tissue obtained from GB patients (Figures 2O, S3J, and S3K), as well as in the neuronal cell state and OPC/NPC-like cell states (Figures 2P and S3L–S3N). Furthermore, the invasivity score correlated well with the distribution of connected$^{TUM/AC}$ and unconnected$^{TUM/AC}$ GBC states, the distribution of the neuronal cell state, and morphological invasiveness (Figures S4A–S4F). Lastly, the gene signatures of the invasivity score were positively correlated with genes and GO terms of neuronal features, migration, and invasion (Figures S4G–S4J; Table S2; STAR Methods).

DeepISTI: A workflow to study TM dynamics in high resolution

As neuronal and neural progenitor-like cell states were associated with invasivity of GBCs, we next wanted to understand how cellular neuronal features relate to brain tumor invasion. GBCs stably expressing mGFP to reveal finest structural details such as filopodia were intravitally time-lapse-imaged at reduced phototoxicity while maintaining spatial and temporal resolution using deep learning image restoration (Weigert et al., 2018). We refer to this approach as deep-learning-enabled intravital subcellular time-lapse imaging (DeepISTI, Figures 3A, 3B, and S5A; Video S2; see STAR Methods). The signal-to-noise ratio strongly increased with DeepISTI, providing a basis for subsequent automated image analyses (Figures 3B, 3C, S5A, and S5B).

Before using DeepISTI, we determined the contribution of cellular compartments to cell volume and surface because these parameters govern the interaction of GBC with the brain parenchyma. A quantitative morphometric analysis showed that in single GBCs, TMs contributed mainly to GBC volume and surface area and served as the predominant site of interaction with neurons in the brain (Figures 3D–3L and S5C).

GBCs use neuronal cellular mechanisms for migration and invasion

To assess the dynamics of GBCs and their processes, we used DeepISTI to intravitally follow individual cells over several hours in PDX models. Figure 3M shows an unconnected$^{TUM/AC}$ GBC that extended two processes and moved the soma in the same direction, while retracting the trailing process. In contrast, the soma remained at the same position in non-somatokinetic cells while the TM extended further only little (Figure 3M). Somatokinetic cells exhibited a higher TM turnover (Figures 3N–3P). To understand whether all TMs contribute to the invasive process, we subclassified them based on whether they are connected to other TMs or whether they are blind-ending (Figure 3Q). We found that blind-ending TMs contribute largely to TM invasion, as they showed a much higher turnover than tumor-connected TMs (Figure 3R). As expected, unconnected$^{TUM/AC}$ GBCs showed a higher TM turnover than connected$^{TUM/AC}$ ones (Figure 3S). When focusing on invasive, blind-ending TMs we found three main mechanisms of TM movement patterns consisting of protrusion, retraction, and TM generation via TM branching (Figures 3T and S5D–S5K; Video S2). Interestingly, these mechanisms were reminiscent of dynamics occurring during migration of immature neurons (Marín et al., 2010; Martini et al., 2009). On a smaller spatial scale we found filopodial extensions (Figures 4A–4C, S5L, and S5M), with only a few converting into TM-like protrusions (Figures 4A, 4D, and S5N–S5P; Video S2). TM-like

Figure 3. Heterogeneous cell soma and TM mechanisms drive GBC invasion

(A) Scheme of the DeepISTI workflow.
(B) Raw IV2PM image compared with restored, enhance.ai (green), enhance.ai merged with probability map (white).
(C) Signal-to-noise ratio at different steps of the image processing workflow and different IV2PM time points of the same GBC.
(D) 3D renderings of a segmented human GBC resected from a GB patient (left, confocal microscopy) and segmented GBCs from PDX model (right, IV2PM). TMs (green), GBC somata (blue).
(E–G) Characterization of TM versus soma volume per GBC, surface area per TMs and GBC soma, as well as relative contribution of surface area compared with volume from TMs to somata (n = 79 GBCs from 10 patients, Wilcoxon matched-pairs signed rank test).
(H–J) Characterization of TMs versus somata volume per GBC (H), surface area per TM and GBC soma (I), as well as the relative contribution of surface area compared with volume from TMs to somata (J) in the S24 PDX model (n = 123 GBCs from 7 S24 PDX mice, Wilcoxon matched-pairs signed rank test).
(K) Probability map of *ex vivo* confocal imaging, PDX mouse, brain slices stained with anti-beta-III-tubulin antibody, a pan-neuronal marker (red, average intensity projection). 3D rendering of the same region, segmented GBC (green), contact areas with neurons (red).
(L) Morphometry of the relative contact surface area between GBC and neurons in TMs versus somata (n = 50 GBCs from 3 mice, Wilcoxon matched-pairs signed rank test).
(M) IV2PM of TM dynamics in somatokinetic and non-somatokinetic cells in S24 PDX. GBC soma (arrowhead), blind-ending TM (arrows).
(N) Comparison of soma movement with process turnover in somatokinetic GBC (n = 11 GBCs with their respective soma and processes from 5 mice, Wilcoxon test).
(O) As in (H) but non-somatokinetic GBC (n = 10 GBCs with their respective soma and processes from 3 mice, paired t test).
(P) Comparison of TM turnover per TM in somatokinetic versus non-somatokinetic GBCs (n = 103 TMs from 4 mice, Mann-Whitney test).
(Q) IV2PM of TM dynamics in blind-ending and connected TMs.
(R) TM turnover in blind-ending versus connected TMs per TM (n = 586 blind TMs versus n = 110 connected TMs from 9 mice, Mann-Whitney test).
(S) TM turnover in unconnected$^{TUM/AC}$ and connected$^{TUM/AC}$ GBCs (n = 245 TMs of unconnected$^{TUM/AC}$ and n = 125 of connected$^{TUM/AC}$ GBCs from 9 mice, Mann-Whitney test). Connectivity based on morphology.
(T) IV2PM of TM dynamics in blind-ending TM (arrowhead) of GBC (green, mGFP) in 4 h.
(G, J, L, N–P, R, and S) Data represented as mean ± SEM.
(M, Q, and T) Post-processed with enhance.ai and the "remove outliers" function in ImageJ/Fiji.
S24 GBCs used for all experiments.
See also Figure S5 and Video S2.

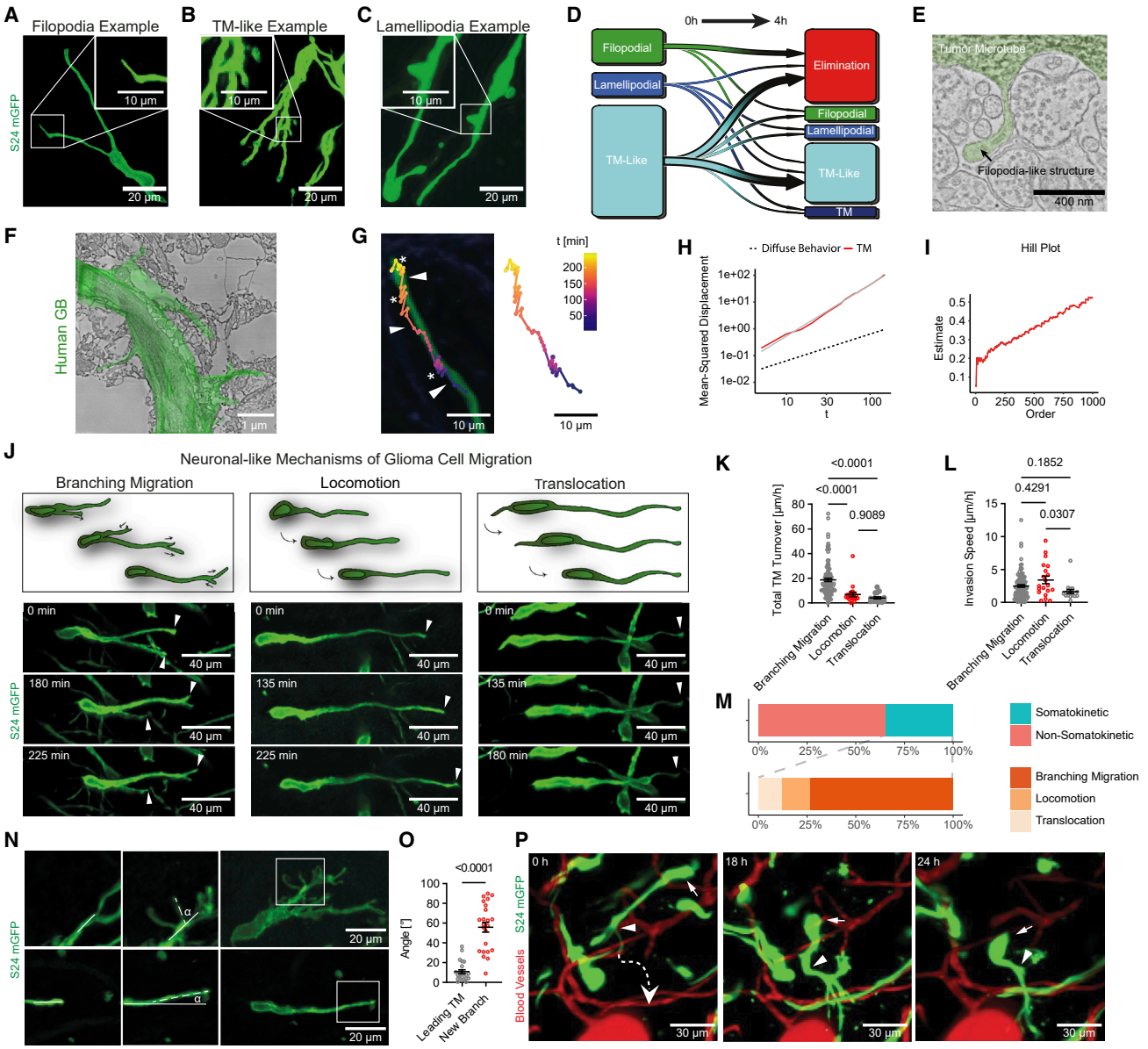

Figure 4. Neuronal-like cellular mechanisms of brain tumor invasion

(A–C) IV2PM post-processed using probability maps showing small process dynamics of GBCs (green).

(D) Transition plot of GBC protrusions over 4 h analyzed with DeepISTI (n = 226 processes from 7 mice).

(E and F) Electron microscopy images of small protrusions (E) (n = 45 small protrusions in n = 11 GBCs from 7 PDX mice) and resected GB patient material (F) (n = 13 small protrusions in n = 4 GBCs).

(G) IV2PM of the tip of a TM with projected TM track indicating dynamics over 4 h (asterisk, stationary phases; arrow head, invasive phases).

(H) Mean-squared displacement of GB TM step lengths (*in vivo* TM tracking). Red line: same in control paradigm. Gray line: best-fit linear regression. Dotted: mean-squared displacement of a diffusive process.

(I) Hill plot of TM track step sizes.

(J) Schematic and examples of 3 neuronal-like mechanisms of GBC invasion in PDX mice. Leading edge of TM (arrowhead). Post-processed with enhance.ai.

(K) Total TM turnover per GBC of different invasion mechanisms (n = 140 GBCs of 16 mice, Kruskal-Wallis test).

(L) *In vivo* invasion speed of different migration patterns (n = 140 GBCs from 16 mice, Kruskal-Wallis test).

(M) Percentage of somatokinetic cells and relative abundance of distinct invasion mechanisms in somatokinetic GBCs (n = 400 GBCs, of these n = 140 invasive GBCs from 16 mice).

(N) *In vivo* example of a GBC showing different leading TM angles.

(legend continued on next page)

protrusions were thicker and longer than filopodia, and more stable, yet about 50% of them were eliminated (Figures 4B and 4D; Figure S5L). Finally, lamellipodial protrusions could transform into TM-like protrusions, persist, or get eliminated at equal chance (Figures 4C and 4D). We also identified these small processes on the ultrastructural level (Figures 4E and 4F). When compared with classical TMs, small protrusions were shorter, more dynamic, and less efficient in their growth (Figures S5M and S5P). In summary, we suggest that TMs and associated small membrane protrusions mediate the dynamic scanning of the brain microenvironment.

When TMs were manually tracked over time (Figure 4G), the analysis revealed small steps interspersed with bigger steps, characteristic of Lévy-like movement (Huda et al., 2018; Zaburdaev et al., 2015). Several mathematical approaches confirmed that GB TM growth follows a stochastic process with a heavy-tailed step-length distribution. This can be interpreted as Lévy-like (Figures 4H and 4I, STAR Methods), a pattern that has been described in animal predators looking for scarce sources of food (Humphries et al., 2012; Sims et al., 2008, 2014) and may reflect an optimal search strategy for sparsely distributed targets (Raposo et al., 2003; Viswanathan et al., 1999, 2008). Hence, TM invasion follows a search-efficient mechanism.

To understand patterns of GBC invasion in more depth, we further examined the dynamics of TMs and somata of invading, unconnected$^{TUM/AC}$, somatokinetic GBCs using DeepISTI. We found three major invasion mechanisms of GBCs: branching migration, locomotion, and translocation (Figures 4J and S5Q–S5T). Branching migration showed extensive branching, protrusion and retraction of the TMs during the invasion of these cells, whereas locomotion appeared in uni- or bipolar cells where the leading TM was protruding, and the soma was following the leading TM. Lastly, translocation occurred with the TM stably anchored and the soma translocating with the length of the TM shortening during this process (Figures 4J and S5U). These three mechanisms of GBC invasion were comparable to neuronal progenitor (Nadarajah et al., 2001, 2003; Tabata and Nakajima, 2003) and other neural progenitor cells (Tsai et al., 2016) migrating during brain development. Quantitative analyses of these processes revealed that branching migration was the mechanism with the highest TM turnover, and also the predominant mechanism of GB invasion (Figures 4K–4M and S5V). We hypothesized that TM branching during GBC invasion may induce directionality changes during invasion. Indeed, GBCs followed newly formed leading TM branches during migration (Figures 4N–4P and S5W–S5Y). Furthermore, the directionality change of leading TMs during protrusion and retraction was significantly lower than in branched TMs (Figures 4O and S5W–S5Y). This mechanism differs from axonal growth cone pathfinding but resembles interneuron movement during tangential migration (Martini et al., 2009; Valiente and Martini, 2009). Hence, GBCs adopt migration strategies initially described for neuronal progenitor cells during development, a feature that is likely related to their neuronal- and neural progenitor-like transcriptional states.

Neuronal activity drives TM formation and TM growth

Next, we asked how neurogliomal synapses (Venkataramani et al., 2019; Venkatesh et al., 2019) would impact the formation and growth of TMs and tumor invasion. For this, neuronal activity was modulated either by varying anesthesia depth or by *in vivo* optogenetic activation of neurons (Figures S6A–S6C). We found that neuronal activity increased the number of TM branching events and TM turnover (Figures 5A–5F), implying that neuronal input drives TM dynamics in the context of invasion. Neuronal activity also increased the average step length of TM movements per GBC (Figures 5G and 5H), and Lévy-like movements were significantly accelerated (Figures 5I, 5J, and S6D–S6K). In effect, these mechanisms lead to a neuronal-activity-related significant increase in invasion speed of GBCs (Figures 5K and 5L).

To identify contributing cellular mechanisms, we tested whether TMs of unconnected$^{TUM/AC}$ GBCs receive direct synaptic input. Using correlative light and electron microscopy (CLEM) to create 3D reconstructions of GBC processes, we unequivocally identified unconnected$^{TUM/AC}$ GBCs in xenograft models and found neurogliomal synapses on these cells (Figure 5M). Functionality of synaptic inputs was established *ex vivo* and *in vitro* via whole-cell patch-clamp recordings from unconnected$^{TUM/AC}$ GBCs, identified by dye filling (Figure 5N). Spontaneous excitatory post-synaptic currents (EPSCs) demonstrated functional synaptic input to unconnected$^{TUM/AC}$ GBCs (Figures 5O and S6L). Additionally, using the same approach, we could show that also connected$^{TUM/AC}$ GBCs can receive synaptic input (Figure S6M–S6V). Lastly, we studied the dynamics of neurogliomal synapses on unconnected$^{TUM/AC}$ GBCs. We found that neurogliomal synaptic boutons are predominately transient on invasive, unconnected$^{TUM/AC}$ GBCs (Figures S6W–S6Z). Together, these findings demonstrate that synaptic input stimulates unconnected$^{TUM/AC}$ GBCs to invade the brain.

Calcium transients in GBCs control TM dynamics and invasion speed

To understand whether neuronal activity was also functionally relevant for putative downstream mechanisms such as calcium transients, we established 3D *in vivo* calcium imaging of GBCs, similar to Bindocci et al. (2017) (Figure 6A; Video S3). We found complex calcium signals including microdomains in TMs and somata (Figures S7A–S7F). Neuronal activity drove these complex calcium dynamics in single GBCs. Optogenetic activation of neurons *in vivo* and *in vitro* glutamate puffing in co-cultures increased calcium event area and frequency in GBCs (Figures 6B–6E and S7G–S7J). To identify functional consequences of these single-cell calcium dynamics increased by neuronal activity, calcium events were ablated in GBCs using the calcium

(O) Comparison of leading TM angles during elongation and branching TM angles (n = 151 TM from 7 mice, Mann-Whitney test).
(P) Example of a GBC *in vivo* with branching migration and directionality change during 24 h. Soma (arrow), TM tree (arrow head), migration path (dashed line).
(K, L, and O) Data represented as mean ± SEM.
S24 GBCs used for all experiments.
See also Figure S6 and Video S2.

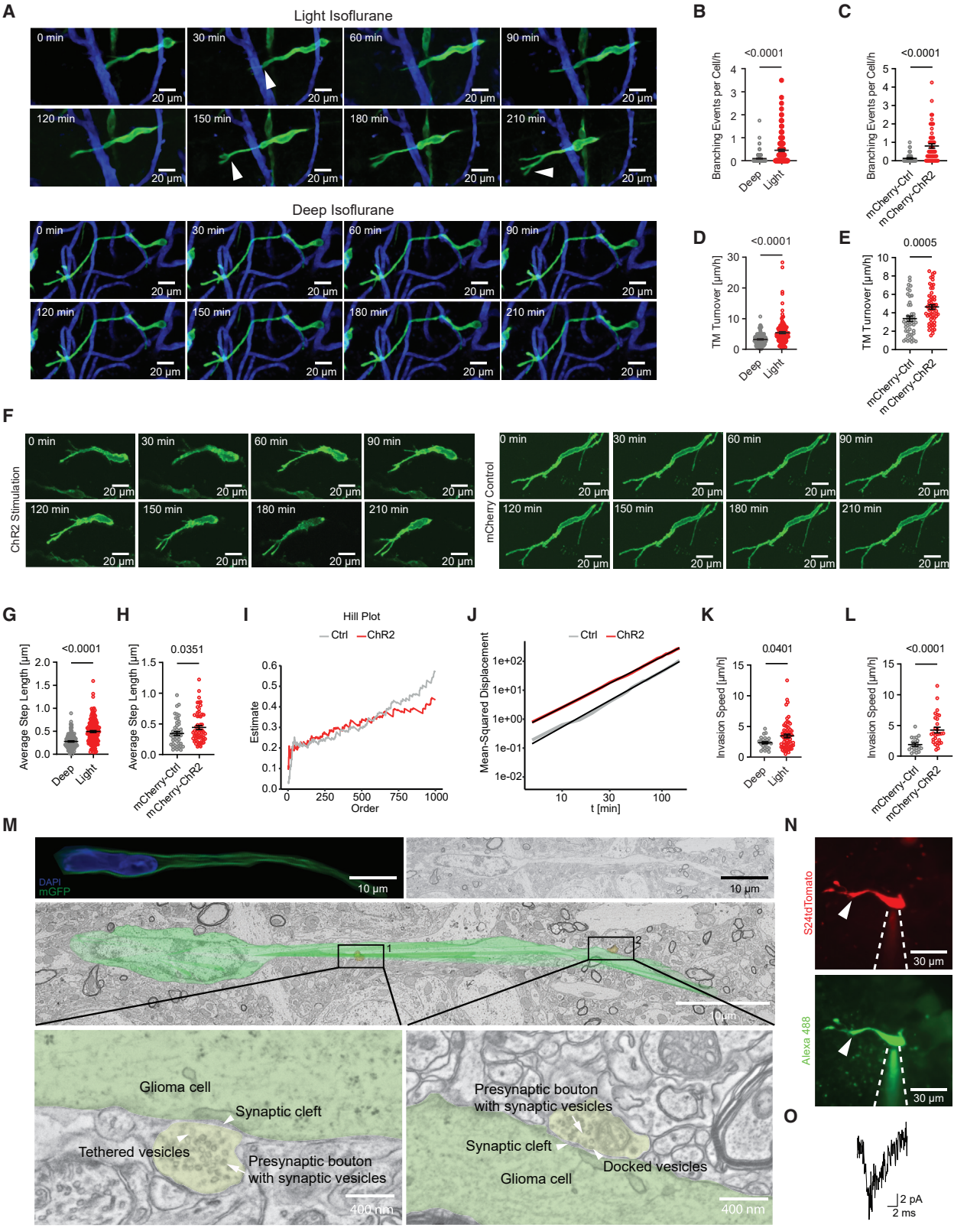

(legend on next page)

chelator BAPTA-AM (1,2-bis(*o*-aminophenoxy)ethane-*N*,*N*,*N*′,*N*′-tetraacetic acid). TM generation as well as GBC invasion were significantly reduced (Figures 6F–6I and S7K–S7O). To identify downstream mechanisms, a transcription factor analysis (Yu et al., 2020) revealed cAMP response element-binding protein (CREB) as a potential neuronal-activity-dependent and calcium-regulated target (Figures 6J, S7P, and S7Q). CREB was targeted with the inhibitor 666-15 (Middei et al., 2013; Zirpel et al., 2000), resulting in reduced TM generation and GBC invasion (Figures 6K–6M). Thus, these analyses together with the discovery of neurogliomal synapses on unconnected$^{TUM/AC}$ tumor cells provide a crucial link between neuronal activity, calcium signaling, and TM-dependent tumor invasion, connecting three key biological factors of brain tumor biology.

Neurogliomal synapses containing AMPA-type glutamate receptors drive TM generation

To understand how neuronal synaptic input to GBCs affects TM dynamics, we investigated the spatial distribution of α-amino-3-hydroxy-5-methyl-4-isoxazolepropionic acid receptor-type glutamate receptors (AMPARs) (Venkataramani et al., 2019; Venkatesh et al., 2019). An AMPAR gene expression score was applied to bulk RNA-seq data (Puchalski et al., 2018) as well as scRNA-seq data of spatially defined GB regions (Yu et al., 2020). Both analyses showed that AMPAR gene expression is enriched at the tumor rim compared with the core (Figures 7A–7C and S8A), supporting a key role of neurogliomal synapses for tumor invasion. In line, AMPAR gene expression scores are significantly enriched in unconnected$^{TUM/AC}$ GBCs compared with connected$^{TUM/AC}$ GBCs (Figures 7D and S8B; Hai et al., 2021). Correlating these analyses back to the gene- and pathway-based cell states discussed before unveiled enriched AMPAR gene expression in neuronal-like, non-MES-like, and neurodevelopmental cell states (Figures 7E–7I and S8C–S8G). Lastly, we found two cell clusters in the rim of human GB to be enriched for the AMPAR gene expression score, synaptic and cell projection GO terms and associated with a high invasivity gene expression score (Figures S8H–S8J). In summary, AMPAR expression in unconnected$^{TUM/AC}$ GBCs of the neuronal and non-MES-like cell states is associated with activity-dependent TM dynamics and invasion.

To link AMPAR-mediated responses to changes in cell morphology, co-cultures of neurons and GBCs were investigated by electrophysiology and confocal microscopy. GBCs exhibiting spontaneous EPSCs when co-cultured with neurons had longer TMs and more branches/filopodia than GBCs without neuronal input, suggesting that synaptic input drove TM formation and growth (Figures 7J–7L and S8K). The frequency and magnitude of GBC calcium events elicited by glutamate puffing was reversibly decreased by CNQX in a GBC subpopulation (Figures 7M, 7N, and S8L). To further support a contribution of AMPARs to TM formation and growth, we expressed dominant-negative AMPAR in GBCs and evaluated the structural consequences by IV2PM (Figure 7O). The total length and number of TMs and number of branching points were significantly reduced (Figures 7P, 7Q, S8M, and S8N), consistently demonstrating that synaptic input via AMPAR is required for TM formation and growth. As a first step toward clinical translation, mice received the FDA-approved AMPAR inhibiting antiepileptic drug

Figure 5. Neuronal activity stimulates genesis and growth of invasive TMs

(A) Comparison of unconnected$^{TUM/AC}$ GBC under light versus deep anesthesia with IV2PM. GBC (green), blood vessels (blue). Dynamic TMs and TM genesis of the unconnected$^{TUM/AC}$ GBCs under light anesthesia (arrow heads). Post-processed with enhance.ai and "remove outliers" function in ImageJ/Fiji.

(B) Branching events per GBC *in vivo* under isoflurane anesthesia (n = 122 GBCs under deep and n = 158 GBCs under light anesthesia from 6 versus 6 mice, Mann-Whitney test).

(C) As in (B) but neuronal channelrhodopsin stimulation compared with control (n = 45 GBCs under mCherry control conditions and n = 57 GBCs under mCherry-ChR2 conditions from 3 versus 4 mice, Mann-Whitney test).

(D) TM turnover per GBC and TM under isoflurane anesthesia (n = 122 GBCs under deep and n = 158 GBCs under light anesthesia from 6 versus 6 mice, Mann-Whitney test).

(E) As in (D), but neuronal channelrhodopsin stimulation as compared with control (n = 45 GBCs under mCherry control conditions and n = 57 GBCs under mCherry-ChR2 conditions from 3 versus 4 mice, Mann-Whitney test).

(F) Exemplary time-lapse IV2PM of somatokinetic S24 GBCs after neuronal channelrhodopsin stimulation and control conditions.

(G) Average step length of TM dynamics per GBC under isoflurane anesthesia (n =122 GBCs under deep and n = 158 under light anesthesia GBCs from 6 versus 6 mice, Mann-Whitney test).

(H) As in (F), but neuronal channelrhodopsin stimulation as compared with control (n = 45 GBCs under mCherry control conditions and n = 57 GBCs under mCherry-ChR2 conditions from 3 versus 4 mice, Mann-Whitney test).

(I) Hill plot of TM movement steps of neuronal channelrhodopsin stimulation compared with mCherry control.

(J) Mean-squared displacement of TM movement steps of a neuronal channelrhodopsin stimulation paradigm compared with control conditions. The black lines illustrate the best-fit linear regression.

(K) Invasion speed of somatokinetic GBCs under isoflurane anesthesia n = 26 under deep and n = 60 GBCs under light anesthesia from 6 versus 6 mice, Mann-Whitney test).

(L) Invasion speed of somatokinetic GBCs after neuronal channelrhodopsin stimulation versus control (n = 19 GBCs under mCherry control conditions and n = 29 GBCs under mCherry-ChR2 conditions from 3 versus 4 mice, Mann-Whitney test).

(M) Unconnected$^{TUM/AC}$ GBC identified using *ex vivo* correlative light and electron microscopy. Pre-synaptic axons are shown in sepia, and post-synaptic GBC TMs are shown in green. Confocal images post-processed with denoise.ai.

(N) Confocal image of unconnected$^{TUM/AC}$ GBC (red, expression of tdTomato) in co-culture. Cell filled with Alexa488 (green), no connected$^{TUM/AC}$ cells detectable.

(O) Representative spontaneous EPSC recorded from unconnected$^{TUM/AC}$ GBC shown in (M) (n = 12 GBCs from 7 mice).

(B–E, G, H, K, and L) Data represented as mean ± SEM.

S24 GBCs used for all experiments.

See also Figure S6.

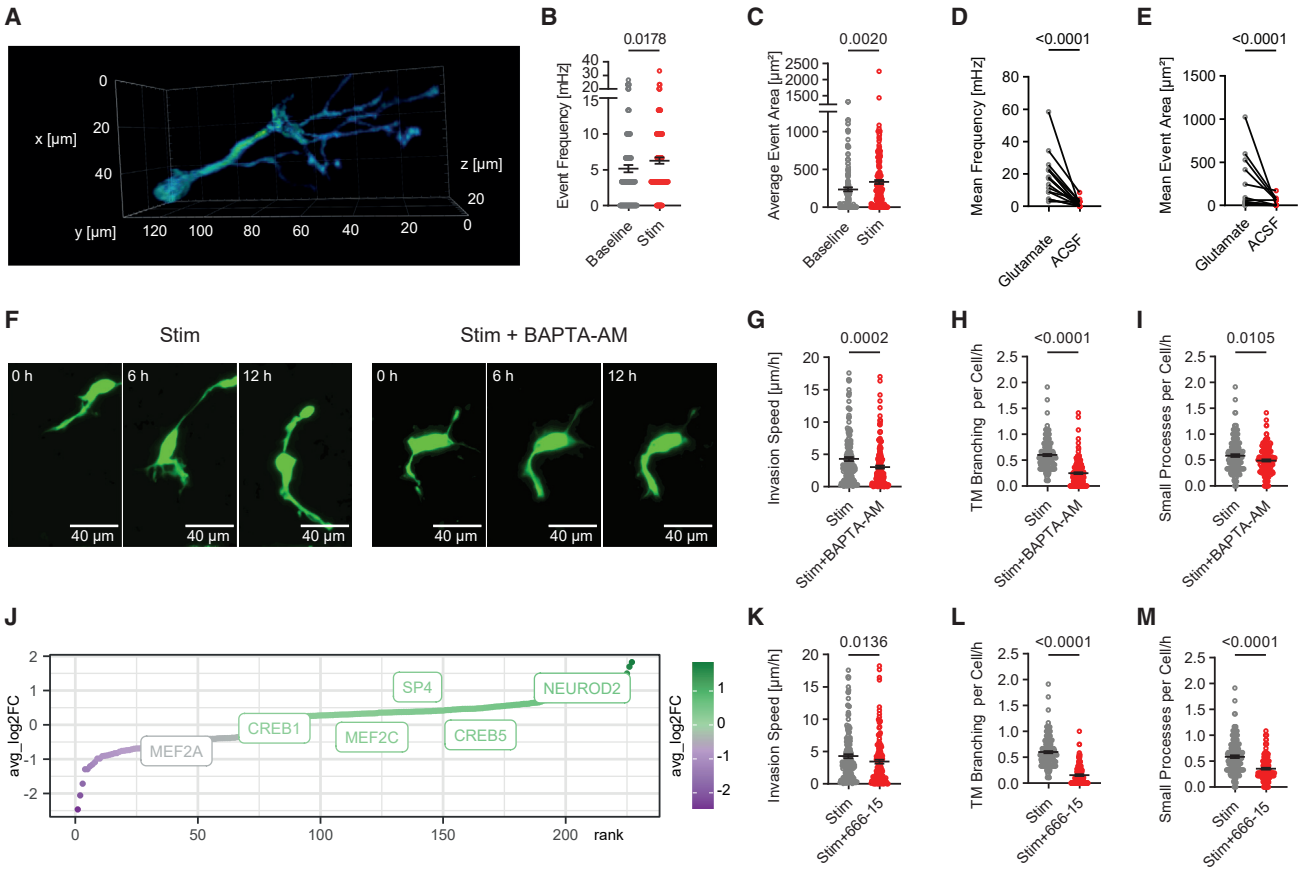

Figure 6. Distinct calcium transient patterns mediate GBC invasion

(A) 3D rendering of *in vivo* 3D calcium imaging of a GBC.

(B) Frequency of calcium events after intravital neuronal channelrhodopsin stimulation compared with baseline.

(C) As in (B), but area of calcium events (n = 157 GBCs in 6 mice [2 with neuronal ChR2(H134R)-mCherry and 4 with neuronal ChrimsonR-mScarlet] in B and C, two-tailed Wilcoxon test).

(D) Mean frequency of calcium events in GBCs, *in vitro* neuron/astrocyte co-cultures after puffing of glutamate versus aCSF only (n = 17 S24 GBCs, two-tailed Wilcoxon test).

(E) As in (D), but mean area of calcium events (n = 17 S24 GBCs, two-tailed Wilcoxon test).

(F–I) S24 GBCs in neuron/astrocyte co-cultures with neuronal stimulation via gabazine (Stim, left) or gabazine and preincubated with BAPTA-AM (Stim + BAPTA-AM, right). (F) Confocal time-lapse imaging series of representative GBCs. Post-processed with denoise.ai. (G) GBC invasion speed, (H) TM branching events per GBC per hour, and (I) small process turnover per GBC per hour (n =170 in control and n = 335 S24 GBCs under BAPTA-AM preincubated conditions in n = 4 independent experiments, Mann-Whitney test).

(J) Marker regulons of neuronal rim cells compared with other cells in the Yu dataset.

Transcription factors previously described to be responsive upon neuronal activity and mediators of neuronal morphology highlighted.

(K–M) GBC invasion speed (K), TM branching events per GBC per hour (L) and small process turnover per GBC per hour (M) under 666-15 (CREB inhibitor) preincubation and additional neuronal stimulation with gabazine compared with stimulated control in co-cultures (n = 61 cells in control and n = 120 S24 GBCs under 666-15 preincubation in n = 3 independent experiments, Mann-Whitney test).

(B, C, G–I, K, L, and M) Data represented as mean ± SEM.

See also Figure S7 and Video S3.

perampanel, and comparable tumor regions of treated and control mice were assessed intravitally (Figure 7R). TM length and branching points were significantly reduced by perampanel treatment (Figures 7S–7V and S8O–S8Z).

DISCUSSION

Our work demonstrates that a distinct subpopulation of GBCs, transcriptionally residing in neuronal- and neural-progenitor-like cell states and not connected to other tumor cells or astrocytes, but receiving neuronal synaptic input, is driving brain invasion via adaptation of cellular neuronal mechanisms. This mechanism of tumor cell migration allows effective brain colonization and thus contributes to GB's incurability.

In this study, we connected recently described gene- and pathway-based classifications (Garofano et al., 2021; Neftel et al., 2019) with their functional relevance for GBC invasion of the brain. Previous work was focused on tumor-connected

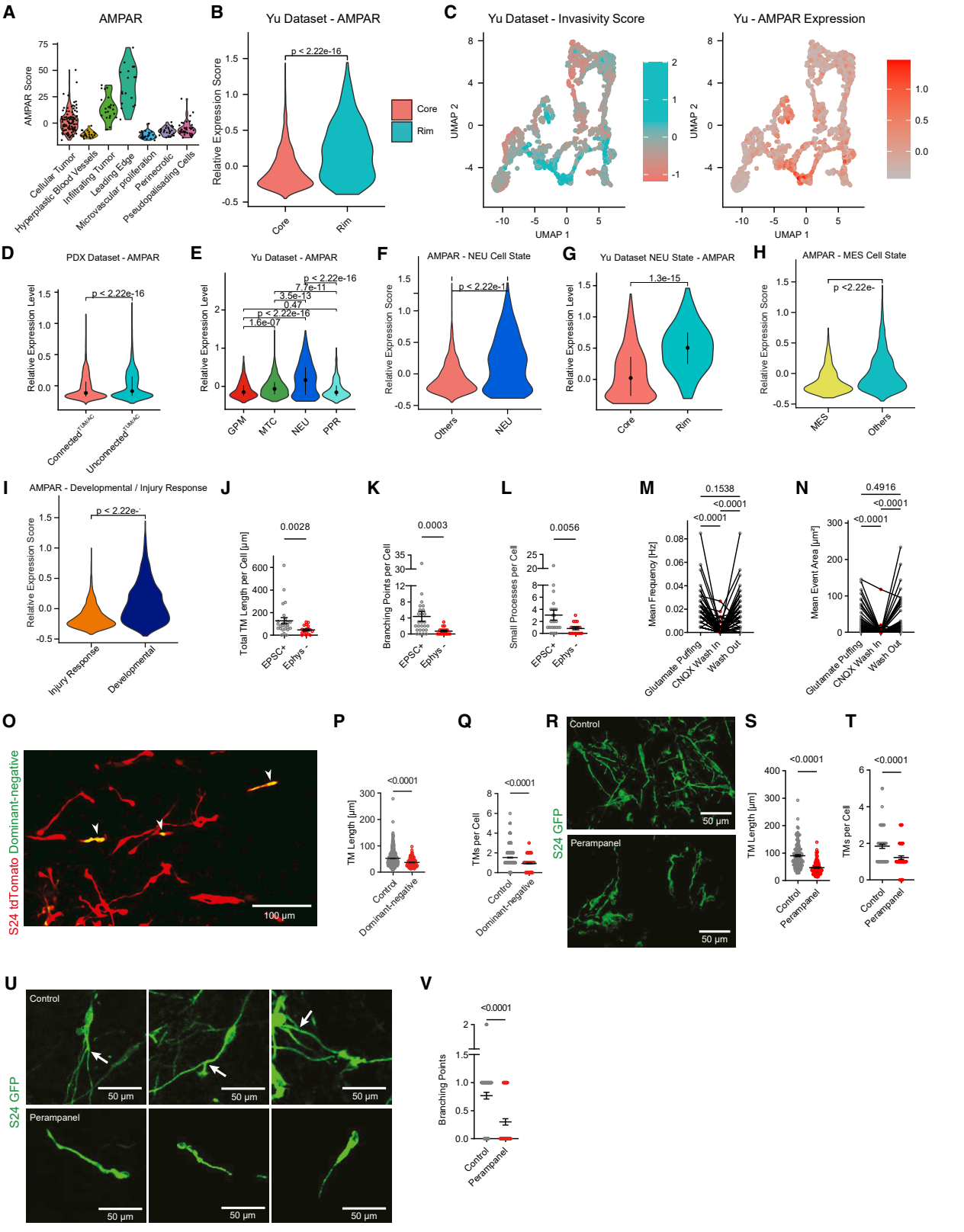

(legend on next page)

GBCs and their networks connected via TMs (Jung et al., 2017; Osswald et al., 2015; Weil et al., 2017; Xie et al., 2021), with therapeutic resistance governed by this homotypic tumor cell network (Jung et al., 2021; Osswald et al., 2015; Weil et al., 2017). Here, we extended this concept of the "GB connectome" to astrocytes *in vivo*, with direct gap junction-mediated heterotypic contacts between both cell types (Sin et al., 2016; Zhang et al., 1999).

In contrast to previous work suggesting collective network invasion of GBCs (Gritsenko et al., 2020) and our own hypotheses (Osswald et al., 2015), we found that unconnected$^{TUM/AC}$ GBCs receiving neurogliomal synaptic input drive brain invasion and colonization. This could be explained by *in vitro* models that were previously used (Gritsenko et al., 2017). Furthermore, a sufficient temporal and spatial resolution was obligatory to uncover the role of unconnected$^{TUM/AC}$ GBCs, as these cell states transition into connected$^{TUM/AC}$ GBCs. Thus, unconnected$^{TUM/AC}$ and connected$^{TUM/AC}$ GBCs represent opposite ends of a cell state gradient.

As connected$^{TUM/AC}$ and unconnected$^{TUM/AC}$ GBCs could be functionally separated and subsequently characterized with scRNA-seq, we could overlay their tumor biological differences with the molecular cell states for gene- and pathway-based classification. The neuronal, OPC/NPC and neurodevelopmental-like cell states were enriched in the unconnected$^{TUM/AC}$ GBCs, whereas the connected$^{TUM/AC}$ GBCs were enriched for AC/MES-like and non-NEU cell states as well as those associated with an injury response. In contrast to previous work suggesting a role for epithelial-to-mesenchymal transition in invasion of GB (Iwadate, 2016; Siebzehnrubl et al., 2013), we found that MES-like cell states were enriched in the core of GB samples where tumor networks prevail.

This is in line with a recent publication demonstrating that upregulation of neuronal signaling programs is associated with brain tumor invasiveness at recurrence in isocitrate dehydrogenase (IDH)-wild-type gliomas, including GBs (Varn et al., 2022).

We also demonstrate a transition of cell states in GB: with expansion of the tumor mass and as tumor cellularity increases, unconnected$^{TUM/AC}$ GBCs were progressively integrating into a tumor cell/astrocyte-connected network, suggesting an ordered evolution of cell states during the progression of GB. This context-dependent transition of GBC states in the infiltration zone adds another layer of complexity to the recent debate of brain tumor cell state transitions (Chaligne et al., 2021; Fine, 2019; Wang et al., 2019a). Importantly, the framework developed here for GB points toward fruitful opportunities for other tumor entities where molecular intratumoral heterogeneity is increasingly well understood, but without clear links to tumor biology yet.

Analogous mechanisms to neuronal migration during neurodevelopment demonstrate a second layer of neuronal features. The three different mechanisms of GB single-cell invasion *in vivo* reported here enhance current ideas of GB invasion obtained *in vitro* (Bhaduri et al., 2020). This extends the concept of how basic neurodevelopmental pathways are hijacked to further brain tumor progression.

The last layer of neuronal features was the observation that neuron-GBC synaptic activity can generate new TMs and also makes their brain scanning behavior more efficient, ultimately driving GB invasion and progression. In addition to previous work suggesting synapses mainly on tumor-connected GBCs (Venkataramani et al., 2019; Venkatesh et al., 2019), we now found that glutamatergic synaptic contacts are present on unconnected$^{TUM/AC}$ GBCs as well; here, neurogliomal synapses drive efficient migration and brain colonization of GBCs. Together this advances our understanding of how heterotypic multicellular networks in brain tumors are differentially regulating tumor biological functions. Finally, targeting specific subcellular mechanisms of TM dynamics and TM formation decreased overall invasion in

Figure 7. Pharmacological and genetic perturbation of AMPA receptors inhibits TM-related mechanisms of invasivity

(A) AMPAR gene expression score (see STAR Methods) in different tumor regions (Ivy GB Atlas, n = 270 human GB samples).
(B) AMPAR gene expression score in GB core versus rim regions (Yu dataset).
(C) UMAP plots with invasivity expression score (left) and AMPAR expression score (right).
(D) Violin plot displaying AMPAR gene expression scores between connected$^{TUM/AC}$ and unconnected$^{TUM/AC}$ GBCs in the PDX dataset (n = 35,822 cells).
(E) Violin plot displaying the AMPAR gene expression score in Yu dataset sorted by the pathway-based cell states.
(F) AMPAR gene expression score in the neuronal cell state compared with all non-neuronal cell states.
(G) Violin plot displaying AMPAR expression in the neuronal cell state of the GB core as compared with the GB rim in the Yu dataset.
(H) AMPAR gene expression score in the MES-like cell state compared with all non-MES-like cell states.
(I) AMPAR gene expression score in injury response transcriptional signature-enriched GBCs compared with neurodevelopmental transcriptional signature-enriched GBCs.
(J and K) Comparison of EPSC-positive S24 GBCs compared with GBCs not receiving neuronal input with regard to total TM length per cell (J) and branching points (K) (n = 44 GBCs, Mann-Whitney test).
(L) Small processes per cell of EPSC-positive S24 GBCs compared with GBCs not receiving neuronal input (n = 44 GBCs, Mann-Whitney test).
(M and N) Mean frequency (M) and mean event area (N) of calcium transients in BG5 GBCs *in vitro* during glutamate puffing and effect of cyanquixaline (CNQX) in a subpopulation (n = 70 GBCs, Friedman test).
(O) IV2PM of S24 tdTomato GBCs expressing dominant-negative AMPARs (yellow, arrow heads) and S24 tdTomato GBCs that do not express them (red).
(P and Q) TM length per cell (P) (n = 718 TMs from 6 S24 PDX mice, Mann-Whitney test) and TMs per cell (Q) of control versus dominant-negative S24 GBCs (n = 593 TMs from 6 S24 PDX mice, Mann-Whitney test).
(R) IV2PM of tumor microregions of S24 PDX mice under control and perampanel-treated conditions.
(S and T) TM length per cell (S) (n = 243 TMs from 6 S24 PDX mice, Mann-Whitney test) and number of TMs per cell (T) (n = 142 TMs from 6 S24 PDX mice, Mann-Whitney test) under control and perampanel conditions.
(U) IV2PM of single GBC in control versus perampanel treatment in S24 PDX mice. Arrows at branching points of TMs.
(V) Branching points per GBC under control and perampanel conditions (n = 184 GBCs from 7 S24 PDX mice, Mann-Whitney test).
(B–F) (Yu dataset, n = 2,795 cells). (J–L, P,Q, S, T, and V) Data represented as mean ± SEM.
See also Figure S8.

GB by mechanisms downstream of AMPAR signaling. Synaptic input stimulating the migration of unconnected$^{TUM/AC}$ GBCs is mirrored by synaptic input driving neuronal progenitor cell migration during brain development (Ohtaka-Maruyama et al., 2018; Wefers et al., 2017).

In conclusion, we present a model of how three layers of neuronal features drive GBC invasion, reaching from molecular cell states over cellular mechanisms that resemble neuronal progenitor-like migration to functional effects of synaptic communication of neurons with migrating tumor cells. This explains how dissemination and cellular heterogeneity of brain tumors, two crucial hallmarks of the disease, are closely interlinked and identifies specific vulnerabilities that can be clinically tested, such as the dependency of migrating tumor cells on AMPAR signaling.

Limitations of the study

In this study, the nature of tumor progression and evolution of cell states was analyzed using multiple PDX models. However, the effects of therapeutic pressures including radio- and chemotherapy and effects of surgical resection were not analyzed. Thus, to completely characterize tumor heterogeneity, its biological functions, its interrelations with invasion, proliferation, and therapeutic resistance will require further studies. As the IV2PM cell state analysis showed that unconnected$^{TUM/AC}$ GBCs evolve over time into connected$^{TUM/AC}$ GBCs, it will be important to further understand whether and how many intermediary cell states might exist, and how they might interchange during brain tumor progression. Furthermore, it is yet unclear which factors drive this cell state evolution, including the role of neuroglioma synapses. Although neuroglioma synapses exist on both unconnected$^{TUM/AC}$ and connected$^{TUM/AC}$ GBCs, the role for the latter is less well understood; it is reasonable to assume that synaptic input activates intercellular Ca^{2+} waves and promotes growth and potentially resistance of the main tumor mass. Interestingly, on a broad gene expression level, unconnected$^{TUM/AC}$ GBCs are enriched for synaptic gene signatures such as the AMPAR gene expression score. However, this is likely due to the large heterogeneity of connected$^{TUM/AC}$ GBCs. Therefore, the characterization of GBCs receiving neuroglioma synapses with respect to their connectivity to other GBCs and astrocytes will be an important line of future investigations. Furthermore, the timescale on which synaptic input effects tumor biology and cell state transitions remains unclear. For this purpose, further technological innovation that can directly link connectivity, molecular, and functional analyses on a single-cell level is needed. It will be interesting to learn whether additional cell types of the brain tumor microenvironment can interconnect with GBCs and heterotypic tumor cell networks. Lastly, the clinical translation of the basic research findings reported here will require further studies in GB patient cohorts and further technological development to monitor the diffuse brain tumor infiltration zone with clinical imaging.

STAR★METHODS

Detailed methods are provided in the online version of this paper and include the following:

- Acute brain slice preparation
- Electrophysiology
- Electrophysiological validation of neuronal channelrhodopsin activation
- Perampanel treatment effects on GBC morphology over time
- Validation of the invasivity score
- Lévy-like walk analysis of GB motility
- Sensitivity analysis of Lévy-like walk analysis
- Fractional Compound Poisson Process
- Fractional Brownian Motion
- Other Gaussian processes
- Numerical Experiments

● QUANTIFICATION AND STATISTICAL ANALYSIS

SUPPLEMENTAL INFORMATION

Supplemental information can be found online at https://doi.org/10.1016/j.cell.2022.06.054.

ACKNOWLEDGMENTS

V.V. received financial support from the German Research Foundation (DFG: VE1373/2-1), the Else Kröner-Fresenius-Stiftung (2020-EKEA.135) and the Medical Faculty of Heidelberg University (Physician-Scientist-Program, Krebs-und Scharlachstiftung). Y.Y., M.C.S., S.K.T., E.R., and D.I.T. were supported by the Deutsche Krebshilfe/German Cancer Aid (Mildred-Scheel-Scholarship for MD students). V.V., T. Kessler, W.W., and F.W. were supported by a grant from the German Research Foundation (DFG: SFB 1389). Y.A.Y., A.G., and S.P.N. were supported by GLIOTRAIN ITN H2020 grant no. 766069. We gratefully acknowledge the data storage service SDS@hd supported by the Ministry of Science, Research, and the Arts Baden-Württemberg (MWK).

We thank M. Kaiser, M. Schmitt, C. Kocksch, D. Domínguez Azorín, M. Karreman, S. Wendler, and C. Löb for technical assistance. We thank T. Chopurian and C. Strahle for initial contributions. We thank K. Kandere-Grzybowska and K. Polev for initial discussions. We thank F. Blum, T. Rubner, M. Eich, K. Hexel, and S. Schmitt from the Flow Cytometry Core Facility of the German Cancer Research Center for their assistance in performing FACS experiments. We thank K. Becker, K. Dell, K. Schmidt, and A. Berdel for providing support and assistance in animal care and design of animal experiments. We thank the EM Core Facility of the Heidelberg University, the EM and Microscopy Core Facility of the German Cancer Research center for their support.

AUTHOR CONTRIBUTIONS

Supervision, V.V., L.D., A.I., W.W., T. Kuner, and F.W.; conceptualization, V.V., T. Kuner, and F.W.; methodology, V.V., Y.Y., M.C.S., S.K.T., C.A.B., N.W., and M.R.; software, V.V., M.C.S., C.A.B., and N.W.; project administration, V.V.; investigation, V.V., Y.Y., M.C.S., S.K.T., M.B., L.F., E.R., N.W., R.L.P., J.W., S.J.S., D.C.H., D.I.T., Y.A.Y., A.G., S.P.N., Y.D., and S.H.; formal analysis, V.V., Y.Y., M.C.S., S.K.T., M.B., C.A.B., L.F., L.G., E.R., N.W., R.L.P., J.W., S.J.S., D.C.H., L.H., T. Kessler, D.I.T., Y.A.Y., A.G., S.P.N., Y.D., S.H., A.L., M.S., L.D., and A.I.; resources, M.R., W.W., T. Kuner, and F.W.; visualization, V.V., Y.Y., M.C.S., S.K.T., M.B., L.F., E.R., N.W., R.L.P., J.W., S.J.S., and D.I.T.; writing – original draft, V.V., T. Kuner, and F.W.; writing – review & editing, V.V., Y.Y., M.C.S., S.K.T., M.B., L.F., E.R., N.W., R.L.P., J.W., S.J.S., D.I.T., M.S., W.W., A.I., T. Kuner, and F.W.; funding acquisition, V.V., W.W., T. Kuner, and F.W.

DECLARATION OF INTERESTS

F.W. and W.W. report the patent (WO2017020982A1) "Agents for use in the treatment of glioma." F.W. is co-founder of DC Europa Ltd (a company trading under the name Divide & Conquer) that is developing new medicines for the treatment of glioma. Divide & Conquer also provides research funding to F.W.'s lab under a research collaboration agreement.

Received: November 12, 2021
Revised: April 10, 2022
Accepted: June 28, 2022
Published: July 27, 2022

REFERENCES

Arnold, L.M.D., and Laurens De, H. (1989). On the estimation of the extreme-value index and large quantile estimation. Ann. Stat. *17*, 1795–1832.

Berg, S., Kutra, D., Kroeger, T., Straehle, C.N., Kausler, B.X., Haubold, C., Schiegg, M., Ales, J., Beier, T., Rudy, M., et al. (2019). ilastik: interactive machine learning for (bio)image analysis. Nat. Methods *16*, 1226–1232.

Bhaduri, A., Di Lullo, E., Jung, D.N., Müller, S., Crouch, E.E., Espinosa, C.S., Ozawa, T., Alvarado, B., Spatazza, J., Cadwell, C.R., et al. (2020). Outer radial glia-like cancer stem cells contribute to heterogeneity of glioblastoma. Cell Stem Cell *26*, 48–63.e6.

Bindocci, E., Savtchouk, I., Liaudet, N., Becker, D., Carriero, G., and Volterra, A. (2017). Three-dimensional Ca(2+) imaging advances understanding of astrocyte biology. Science *356*. eaai8185.

Bodi, E., Hurtado, S.P., Carvalho, M.A., Borojevic, R., and De Carvalho, A.C.C. (2004). Gap junctions in hematopoietic stroma control proliferation and differentiation of blood cell precursors. An. Acad. Bras. Cienc. *76*, 743–756.

Bruce, M.H. (1975). A simple general approach to inference about the tail of a distribution. Ann. Stat. *3*, 1163–1174.

Cahoy, D.O., Uchaikin, V.V., and Woyczynski, W.A. (2010). Parameter estimation for fractional Poisson processes. J. Stat. Plan. Inference *140*, 3106–3120.

Cao, J., Spielmann, M., Qiu, X., Huang, X., Ibrahim, D.M., Hill, A.J., Zhang, F., Mundlos, S., Christiansen, L., Steemers, F.J., et al. (2019). The single-cell transcriptional landscape of mammalian organogenesis. Nature *566*, 496–502.

Capper, D., Jones, D.T.W., Sill, M., Hovestadt, V., Schrimpf, D., Sturm, D., Koelsche, C., Sahm, F., Chavez, L., Reuss, D.E., et al. (2018). DNA methylation-based classification of central nervous system tumours. Nature *555*, 469–474.

Cardona, A., Saalfeld, S., Schindelin, J., Arganda-Carreras, I., Preibisch, S., Longair, M., Tomancak, P., Hartenstein, V., and Douglas, R.J. (2012). TrakEM2 software for neural circuit reconstruction. PLoS One *7*, e38011.

Chaligne, R., Gaiti, F., Silverbush, D., Schiffman, J.S., Weisman, H.R., Kluegel, L., Gritsch, S., Deochand, S.D., Gonzalez Castro, L.N., Richman, A.R., et al. (2021). Epigenetic encoding, heritability and plasticity of glioma transcriptional cell states. Nat. Genet. *53*, 1469–1479.

Chen, C.Y., Matt, L., Hell, J.W., and Rogawski, M.A. (2014). Perampanel inhibition of AMPA receptor currents in cultured hippocampal neurons. PLoS One *9*, e108021.

Cuddapah, V.A., Robel, S., Watkins, S., and Sontheimer, H. (2014). A neurocentric perspective on glioma invasion. Nat. Rev. Neurosci. *15*, 455–465.

Dana, H., Sun, Y., Mohar, B., Hulse, B.K., Kerlin, A.M., Hasseman, J.P., Tsegaye, G., Tsang, A., Wong, A., Patel, R., et al. (2019). High-performance calcium sensors for imaging activity in neuronal populations and microcompartments. Nat. Methods *16*, 649–657.

Dirkse, A., Golebiewska, A., Buder, T., Nazarov, P.V., Muller, A., Poovathingal, S., Brons, N.H.C., Leite, S., Sauvageot, N., Sarkisjan, D., et al. (2019). Stem cell-associated heterogeneity in Glioblastoma results from intrinsic tumor plasticity shaped by the microenvironment. Nat. Commun. *10*, 1787.

Dondzillo, A., Sätzler, K., Horstmann, H., Altrock, W.D., Gundelfinger, E.D., and Kuner, T. (2010). Targeted three-dimensional immunohistochemistry reveals localization of presynaptic proteins Bassoon and Piccolo in the rat calyx of Held before and after the onset of hearing. J. Comp. Neurol. *518*, 1008–1029.

Dorshkind, K., Green, L., Godwin, A., and Fletcher, W.H. (1993). Connexin-43 type gap-junctions mediate communication between bone-marrow stromal cells. Blood *82*, 38–45.

Drumm, M.R., Dixit, K.S., Grimm, S., Kumthekar, P., Lukas, R.V., Raizer, J.J., Stupp, R., Chheda, M.G., Kam, K.L., McCord, M., et al. (2020). Extensive brainstem infiltration, not mass effect, is a common feature of end-stage cerebral glioblastomas. Neuro. Oncol *22*, 470–479.

Dubbs, A., Guevara, J., and Yuste, R. (2016). moco: fast Motion Correction for Calcium Imaging. Front. Neuroinform. *10*, 6.

Fantuzzo, J.A., Mirabella, V.R., Hamod, A.H., Hart, A.H., Zahn, J.D., and Pang, Z.P. (2017). *Intellicount*: High-Throughput Quantification of Fluorescent Synaptic Protein Puncta by Machine Learning. eNeuro *4*, ENEURO.0219-17.2017.

Fine, H.A. (2019). Malignant gliomas: simplifying the complexity. Cancer Discov. *9*, 1650–1652.

Fogarty, M.J., Hammond, L.A., Kanjhan, R., Bellingham, M.C., and Noakes, P.G. (2013). A method for the three-dimensional reconstruction of Neurobiotin™-filled neurons and the location of their synaptic inputs. Front. Neural Circuits *7*, 153.

Friedl, P., Locker, J., Sahai, E., and Segall, J.E. (2012). Classifying collective cancer cell invasion. Nat. Cell Biol. *14*, 777–783.

Garofano, L., Migliozzi, S., Oh, Y.T., D'Angelo, F., Najac, R.D., Ko, A., Frangaj, B., Caruso, F.P., Yu, K., Yuan, J., et al. (2021). Pathway-based classification of glioblastoma uncovers a mitochondrial subtype with therapeutic vulnerabilities. Nat. Cancer *2*, 141–156.

Ge, S.X., Jung, D., and Yao, R. (2020). ShinyGO: a graphical gene-set enrichment tool for animals and plants. Bioinformatics *36*, 2628–2629.

Geluk, J.L., and Haan, L.F.M.d. (1987). Regular Variation, Extensions and Tauberian Theorems (CWI).

Gleeson, J.G., Lin, P.T., Flanagan, L.A., and Walsh, C.A. (1999). Doublecortin is a microtubule-associated protein and is expressed widely by migrating neurons. Neuron *23*, 257–271.

Gneiting, T., and Schlather, M. (2004). Stochastic models that separate fractal dimension and the Hurst effect. SIAM Rev. *46*, 269–282.

Golebiewska, A., Hau, A.C., Oudin, A., Stieber, D., Yabo, Y.A., Baus, V., Barthelemy, V., Klein, E., Bougnaud, S., Keunen, O., et al. (2020). Patient-derived organoids and orthotopic xenografts of primary and recurrent gliomas represent relevant patient avatars for precision oncology. Acta Neuropathol. *140*, 919–949.

Gonzalez, G.A., and Montminy, M.R. (1989). Cyclic-AMP stimulates somatostatin gene-transcription by phosphorylation of Creb at Serine-133. Cell *59*, 675–680.

Gritsenko, P., Leenders, W., and Friedl, P. (2017). Recapitulating in vivo-like plasticity of glioma cell invasion along blood vessels and in astrocyte-rich stroma. Histochem. Cell Biol. *148*, 395–406.

Gritsenko, P.G., Atlasy, N., Dieteren, C.E.J., Navis, A.C., Venhuizen, J.H., Veelken, C., Schubert, D., Acker-Palmer, A., Westerman, B.A., Wurdinger, T., et al. (2020). p120-catenin-dependent collective brain infiltration by glioma cell networks. Nat. Cell Biol. *22*, 97–107.

Hai, L., Hoffmann, D.C., Mandelbaum, H., Xie, R., Ito, J., Jung, E., Weil, S., Sievers, P., Venkataramani, V., Azorin, D.D., et al. (2021). A connectivity signature for glioblastoma. Preprint at. bioRxiv. https://doi.org/10.1101/2021.11.07.465791.

Hara, T., Chanoch-Myers, R., Mathewson, N.D., Myskiw, C., Atta, L., Bussema, L., Eichhorn, S.W., Greenwald, A.C., Kinker, G.S., Rodman, C., et al. (2021). Interactions between cancer cells and immune cells drive transitions to mesenchymal-like states in glioblastoma. Cancer Cell *39*, 779–792.e11.

Horstmann, H., Körber, C., Sätzler, K., Aydin, D., and Kuner, T. (2012). Serial section scanning electron microscopy (S3EM) on silicon wafers for ultra-structural volume imaging of cells and tissues. PLoS One *7*, e35172.

Huda, S., Weigelin, B., Wolf, K., Tretiakov, K.V., Polev, K., Wilk, G., Iwasa, M., Emami, F.S., Narojczyk, J.W., Banaszak, M., et al. (2018). Levy-like movement patterns of metastatic cancer cells revealed in microfabricated systems and implicated in vivo. Nat. Commun. *9*, 4539.

Humphries, N.E., Weimerskirch, H., Queiroz, N., Southall, E.J., and Sims, D.W. (2012). Foraging success of biological Levy flights recorded *in situ*. Proc. Natl. Acad. Sci. USA *109*, 7169–7174.

Iwadate, Y. (2016). Epithelial-mesenchymal transition in glioblastoma progression. Oncol. Lett. *11*, 1615–1620.

Jung, E., Osswald, M., Blaes, J., Wiestler, B., Sahm, F., Schmenger, T., Solecki, G., Deumelandt, K., Kurz, F.T., Xie, R., et al. (2017). Tweety-homolog 1 drives brain colonization of gliomas. J. Neurosci. *37*, 6837–6850.

Jung, E., Osswald, M., Ratliff, M., Dogan, H., Xie, R., Weil, S., Hoffmann, D.C., Kurz, F.T., Kessler, T., Heiland, S., et al. (2021). Tumor cell plasticity, heterogeneity, and resistance in crucial microenvironmental niches in glioma. Nat. Commun. *12*, 1014.

Kantevari, S., Gordon, G.R.J., MacVicar, B.A., and Ellis-Davies, G.C.R. (2011). A practical guide to the synthesis and use of membrane-permeant acetoxymethyl esters of caged inositol polyphosphates. Nat. Protoc. *6*, 327–337.

Lewis, W.H. (1922). Is mesenchyme a syncytium? Anat. Rec. *23*, 177–184.

Liang, W., Gao, R., Yang, M., Wang, X., Cheng, K., Shi, X., He, C., Li, Y., Wu, Y., Shi, L., et al. (2020). MARCKSL1 promotes the proliferation, migration and invasion of lung adenocarcinoma cells. Oncol. Lett. *19*, 2272–2280.

Maere, S., Heymans, K., and Kuiper, M. (2005). BiNGO: a cytoscape plugin to assess overrepresentation of gene ontology categories in biological networks. Bioinformatics *21*, 3448–3449.

Margineanu, D.G., and Wülfert, E. (1997). Inhibition by levetiracetam of a non-GABA(A) receptor-associated epileptiform effect of bicuculline in rat hippocampus. Br. J. Pharmacol. *122*, 1146–1150.

Marín, O., Valiente, M., Ge, X., and Tsai, L.H. (2010). Guiding neuronal cell migrations. Cold Spring Harbor Perspect. Biol. *2*, a001834.

Martini, F.J., Valiente, M., López Bendito, G., Szabó, G., Moya, F., Valdeolmillos, M., and Marín, O. (2009). Biased selection of leading process branches mediates chemotaxis during tangential neuronal migration. Development *136*, 41–50.

McKhann, G.M., 2nd, D'Ambrosio, R., and Janigro, D. (1997). Heterogeneity of astrocyte resting membrane potentials and intercellular coupling revealed by whole-cell and gramicidin-perforated patch recordings from cultured neocortical and hippocampal slice astrocytes. J. Neurosci. *17*, 6850–6863.

Meijering, E., Dzyubachyk, O., and Smal, I. (2012). Methods for cell and particle tracking. Methods Enzymol. *504*, 183–200.

Metzler, R., and Klafter, J. (2000). The random walk's guide to anomalous diffusion: a fractional dynamics approach. Phys. Rep. *339*, 1–77.

Middei, S., Houeland, G., Cavallucci, V., Ammassari-Teule, M., D'Amelio, M., and Marie, H. (2013). CREB is necessary for synaptic maintenance and learning-induced changes of the ampa receptor GluA1 subunit. Hippocampus *23*, 488–499.

Nadarajah, B., Alifragis, P., Wong, R.O., and Parnavelas, J.G. (2003). Neuronal migration in the developing cerebral cortex: observations based on real-time imaging. Cereb. Cortex *13*, 607–611.

Nadarajah, B., Brunstrom, J.E., Grutzendler, J., Wong, R.O., and Pearlman, A.L. (2001). Two modes of radial migration in early development of the cerebral cortex. Nat. Neurosci. *4*, 143–150.

Neftel, C., Laffy, J., Filbin, M.G., Hara, T., Shore, M.E., Rahme, G.J., Richman, A.R., Silverbush, D., Shaw, M.L., Hebert, C.M., et al. (2019). An integrative model of cellular states, plasticity, and genetics for glioblastoma. Cell *178*, 835–849.e21.

Nimmerjahn, A., Kirchhoff, F., Kerr, J.N.D., and Helmchen, F. (2004). Sulforhodamine 101 as a specific marker of astroglia in the neocortex in vivo. Nat. Methods *1*, 31–37.

Ohtaka-Maruyama, C., Okamoto, M., Endo, K., Oshima, M., Kaneko, N., Yura, K., Okado, H., Miyata, T., and Maeda, N. (2018). Synaptic transmission from subplate neurons controls radial migration of neocortical neurons. Science *360*, 313–317.

Osswald, M., Jung, E., Sahm, F., Solecki, G., Venkataramani, V., Blaes, J., Weil, S., Horstmann, H., Wiestler, B., Syed, M., et al. (2015). Brain tumour cells interconnect to a functional and resistant network. Nature *528*, 93–98.

Oudin, A., Baus, V., Barthelemy, V., Fabian, C., Klein, E., Dieterle, M., Wantz, M., Hau, A.C., Dording, C., Bernard, A., et al. (2021). Protocol for derivation of organoids and patient-derived orthotopic xenografts from glioma patient tumors. Star Protoc. *2*, 100534.

Parslow, A., Cardona, A., and Bryson-Richardson, R.J. (2014). Sample drift correction following 4D confocal time-lapse imaging. J. Vis. Exp. *12*, 51086.

Puchalski, R.B., Shah, N., Miller, J., Dalley, R., Nomura, S.R., Yoon, J.G., Smith, K.A., Lankerovich, M., Bertagnolli, D., Bickley, K., et al. (2018). An anatomic transcriptional atlas of human glioblastoma. Science *360*, 660–663.

Rahim, S., Beauchamp, E.M., Kong, Y., Brown, M.L., Toretsky, J.A., and Üren, A. (2011). YK-4-279 inhibits ERG and ETV1 mediated prostate cancer cell invasion. PLoS One *6*, e19343.

Raposo, E.P., Buldyrev, S.V., da Luz, M.G., Santos, M.C., Stanley, H.E., and Viswanathan, G.M. (2003). Dynamical robustness of Levy search strategies. Phys. Rev. Lett. *91*, 240601.

Reynolds, E.S. (1963). The use of lead citrate at high pH as an electron-opaque stain in electron microscopy. J. Cell Biol. *17*, 208–212.

Richards, L.M., Whitley, O.K.N., MacLeod, G., Cavalli, F.M.G., Coutinho, F.J., Jaramillo, J.E., Svergun, N., Riverin, M., Croucher, D.C., Kushida, M., et al. (2021). Gradient of Developmental and Injury Response transcriptional states defines functional vulnerabilities underpinning glioblastoma heterogeneity. Nat. Cancer *2*, 157–173.

Sahm, F., Capper, D., Jeibmann, A., Habel, A., Paulus, W., Troost, D., and von Deimling, A. (2012). Addressing diffuse glioma as a systemic brain disease with single-cell analysis. Arch. Neurol. *69*, 523–526.

Salem, O., Erdem, N., Jung, J., Münstermann, E., Wörner, A., Wilhelm, H., Wiemann, S., and Körner, C. (2016). The highly expressed 5'isomiR of hsa-miR-140-3p contributes to the tumor-suppressive effects of miR-140 by reducing breast cancer proliferation and migration. BMC Genomics *17*, 566.

Santra, M., Santra, S., Roberts, C., Zhang, R.L., and Chopp, M. (2009). Doublecortin induces mitotic microtubule catastrophe and inhibits glioma cell invasion. J. Neurochem. *108*, 231–245.

Schätzle, P., Wuttke, R., Ziegler, U., and Sonderegger, P. (2012). Automated quantification of synapses by fluorescence microscopy. J. Neurosci. Methods *204*, 144–149.

Schindelin, J., Arganda-Carreras, I., Frise, E., Kaynig, V., Longair, M., Pietzsch, T., Preibisch, S., Rueden, C., Saalfeld, S., Schmid, B., et al. (2012). Fiji: an open-source platform for biological-image analysis. Nat. Methods *9*, 676–682.

Schmid, B., Schindelin, J., Cardona, A., Longair, M., and Heisenberg, M. (2010). A high-level 3D visualization API for Java and ImageJ. BMC Bioinformatics *11*, 274.

Schneider, C.A., Rasband, W.S., and Eliceiri, K.W. (2012). NIH Image to ImageJ: 25 years of image analysis. Nat. Methods *9*, 671–675.

Shannon, P., Markiel, A., Ozier, O., Baliga, N.S., Wang, J.T., Ramage, D., Amin, N., Schwikowski, B., and Ideker, T. (2003). Cytoscape: a software environment for integrated models of biomolecular interaction networks. Genome Res. *13*, 2498–2504.

Siebzehnrubl, F.A., Silver, D.J., Tugertimur, B., Deleyrolle, L.P., Siebzehnrubl, D., Sarkisian, M.R., Devers, K.G., Yachnis, A.T., Kupper, M.D., Neal, D., et al. (2013). The ZEB1 pathway links glioblastoma initiation, invasion and chemoresistance. EMBO Mol. Med. *5*, 1196–1212.

Sims, D.W., Reynolds, A.M., Humphries, N.E., Southall, E.J., Wearmouth, V.J., Metcalfe, B., and Twitchett, R.J. (2014). Hierarchical random walks in trace fossils and the origin of optimal search behavior. Proc. Natl. Acad. Sci. USA *111*, 11073–11078.

Sims, D.W., Righton, D., and Pitchford, J.W. (2007). Minimizing errors in identifying Levy flight behaviour of organisms. J. Anim. Ecol. *76*, 222–229.

Sims, D.W., Southall, E.J., Humphries, N.E., Hays, G.C., Bradshaw, C.J., Pitchford, J.W., James, A., Ahmed, M.Z., Brierley, A.S., Hindell, M.A., et al. (2008). Scaling laws of marine predator search behaviour. Nature *451*, 1098–1102.

Sin, W.C., Aftab, Q., Bechberger, J.F., Leung, J.H., Chen, H., and Naus, C.C. (2016). Astrocytes promote glioma invasion via the Gap junction protein connexin43. Oncogene *35*, 1504–1516.

Stelzer, G., Rosen, N., Plaschkes, I., Zimmerman, S., Twik, M., Fishilevich, S., Stein, T.I., Nudel, R., Lieder, I., Mazor, Y., et al. (2016). The GeneCards Suite: from gene data mining to disease genome sequence analyses. Curr. Protoc. Bioinformatics *54*. 1 30 31–31 30 33.

Stuart, T., Butler, A., Hoffman, P., Hafemeister, C., Papalexi, E., Mauck, W.M., 3rd, Hao, Y., Stoeckius, M., Smibert, P., and Satija, R. (2019). Comprehensive integration of single-cell data. Cell *177*, 1888–1902.e21.

Sullivan, K.F., and Cleveland, D.W. (1986). Identification of conserved isotype-defining variable region sequences for four vertebrate beta tubulin polypeptide classes. Proc. Natl. Acad. Sci. USA *83*, 4327–4331.

Tabata, H., and Nakajima, K. (2003). Multipolar migration: the third mode of radial neuronal migration in the developing cerebral cortex. J. Neurosci. *23*, 9996–10001.

Takano, T., Tian, G.F., Peng, W.G., Lou, N.H., Libionka, W., Han, X.N., and Nedergaard, M. (2006). Astrocyte-mediated control of cerebral blood flow. Nat. Neurosci. *9*, 260–267.

Tano, K., Mizuno, R., Okada, T., Rakwal, R., Shibato, J., Masuo, Y., Ijiri, K., and Akimitsu, N. (2010). MALAT-1 enhances cell motility of lung adenocarcinoma cells by influencing the expression of motility-related genes. FEBS Lett. *584*, 4575–4580.

Thestrup, T., Litzlbauer, J., Bartholomäus, I., Mues, M., Russo, L., Dana, H., Kovalchuk, Y., Liang, Y., Kalamakis, G., Laukat, Y., et al. (2014). Optimized ratiometric calcium sensors for functional in vivo imaging of neurons and T lymphocytes. Nat. Methods *11*, 175–182.

Tsai, H.H., Niu, J., Munji, R., Davalos, D., Chang, J., Zhang, H., Tien, A.C., Kuo, C.J., Chan, J.R., Daneman, R., et al. (2016). Oligodendrocyte precursors migrate along vasculature in the developing nervous system. Science *351*, 379–384.

Valiente, M., and Martini, F.J. (2009). Migration of cortical interneurons relies on branched leading process dynamics. Cell Adh. Migr. *3*, 278–280.

Valiunas, V., Doronin, S., Valiuniene, L., Potapova, I., Zuckerman, J., Walcott, B., Robinson, R.B., Rosen, M.R., Brink, P.R., and Cohen, I.S. (2004). Human mesenchymal stem cells make cardiac connexins and form functional gap junctions. J. Physiol. Lond. *555*, 617–626.

Van de Sande, B., Flerin, C., Davie, K., De Waegeneer, M., Hulselmans, G., Aibar, S., Seurinck, R., Saelens, W., Cannoodt, R., Rouchon, Q., et al. (2020). A scalable SCENIC workflow for single-cell gene regulatory network analysis. Nat. Protoc. *15*, 2247–2276.

van der Horst, E.H., Degenhardt, Y.Y., Strelow, A., Slavin, A., Chinn, L., Orf, J., Rong, M., Li, S., See, L.H., Nguyen, K.Q., et al. (2005). Metastatic properties and genomic amplification of the tyrosine kinase gene ACK1. Proc. Natl. Acad. Sci. USA *102*, 15901–15906.

Varn, F.S., Johnson, K.C., Martinek, J., Huse, J.T., Nasrallah, M.P., Wesseling, P., Cooper, L.A.D., Malta, T.M., Wade, T.E., Sabedot, T.S., et al. (2022). Glioma progression is shaped by genetic evolution and microenvironment interactions. Cell *185*, 2184–2199.e16.

Venkataramani, V., Tanev, D.I., Strahle, C., Studier-Fischer, A., Fankhauser, L., Kessler, T., Körber, C., Kardorff, M., Ratliff, M., Xie, R., et al. (2019). Glutamatergic synaptic input to glioma cells drives brain tumour progression. Nature *573*, 532–538.

Venkatesh, H.S., Johung, T.B., Caretti, V., Noll, A., Tang, Y., Nagaraja, S., Gibson, E.M., Mount, C.W., Polepalli, J., Mitra, S.S., et al. (2015). Neuronal activity promotes glioma growth through Neuroligin-3 secretion. Cell *161*, 803–816.

Venkatesh, H.S., Morishita, W., Geraghty, A.C., Silverbush, D., Gillespie, S.M., Arzt, M., Tam, L.T., Espenel, C., Ponnuswami, A., Ni, L., et al. (2019). Electrical and synaptic integration of glioma into neural circuits. Nature *573*, 539–545.

Venkatesh, H.S., Tam, L.T., Woo, P.J., Lennon, J., Nagaraja, S., Gillespie, S.M., Ni, J., Duveau, D.Y., Morris, P.J., Zhao, J.J., et al. (2017). Targeting neuronal activity-regulated neuroligin-3 dependency in high-grade glioma. Nature *549*, 533–537.

Viswanathan, G.M., Buldyrev, S.V., Havlin, S., da Luz, M.G.E., Raposo, E.P., and Stanley, H.E. (1999). Optimizing the success of random searches. Nature *401*, 911–914.

Viswanathan, G.M., Raposo, E.P., and da Luz, M.G.E. (2008). Lévy flights and superdiffusion in the context of biological encounters and random searches. Phys. Life Rev. *5*, 133–150.

Wang, L., Babikir, H., Müller, S., Yagnik, G., Shamardani, K., Catalan, F., Kohanbash, G., Alvarado, B., Di Lullo, E., Kriegstein, A., et al. (2019a). The phenotypes of proliferating glioblastoma cells reside on a single axis of variation. Cancer Discov. *9*, 1708–1719.

Wang, Y., DelRosso, N.V., Vaidyanathan, T.V., Cahill, M.K., Reitman, M.E., Pittolo, S., Mi, X., Yu, G., and Poskanzer, K.E. (2019b). Accurate quantification of astrocyte and neurotransmitter fluorescence dynamics for single-cell and population-level physiology. Nat. Neurosci. *22*, 1936–1944.

Wefers, A.K., Haberlandt, C., Tekin, N.B., Fedorov, D.A., Timmermann, A., van der Want, J.J.L., Chaudhry, F.A., Steinhäuser, C., Schilling, K., and Jabs, R. (2017). Synaptic input as a directional cue for migrating interneuron precursors. Development *144*, 4125–4136.

Weigert, M., Schmidt, U., Boothe, T., Müller, A., Dibrov, A., Jain, A., Wilhelm, B., Schmidt, D., Broaddus, C., Culley, S., et al. (2018). Content-aware image restoration: pushing the limits of fluorescence microscopy. Nat. Methods *15*, 1090–1097.

Weil, S., Osswald, M., Solecki, G., Grosch, J., Jung, E., Lemke, D., Ratliff, M., Hänggi, D., Wick, W., and Winkler, F. (2017). Tumor microtubes convey resistance to surgical lesions and chemotherapy in gliomas. Neuro. Oncol *19*, 1316–1326.

Wick, W., Osswald, M., Wick, A., and Winkler, F. (2018). Treatment of glioblastoma in adults. Ther. Adv. Neurol. Diso *11*. 1756286418790452.

Wimmer, V.C., Nevian, T., and Kuner, T. (2004). Targeted in vivo expression of proteins in the calyx of Held. Pflugers Arch. *449*, 319–333.

Xie, R., Kessler, T., Grosch, J., Hai, L., Venkataramani, V., Huang, L., Hoffmann, D.C., Solecki, G., Ratliff, M., Schlesner, M., et al. (2021). Tumor cell network integration in glioma represents a stemness feature. Neuro. Oncol. *23*, 757–769.

Yu, K., Hu, Y.Q., Wu, F., Guo, Q.F., Qian, Z.H., Hu, W.E., Chen, J., Wang, K.Y., Fan, X.Y., Wu, X.L., et al. (2020). Surveying brain tumor heterogeneity by single-cell RNA-sequencing of multi-sector biopsies. Natl. Sci. Rev. *7*, 1306–1318.

Zaburdaev, V., Denisov, S., and Klafter, J. (2015). Levy walks. Rev. Mod. Phys. *87*, 483–530.

Zhang, H., Kelly, G., Zerillo, C., Jaworski, D.M., and Hockfield, S. (1998). Expression of a cleaved brain-specific extracellular matrix protein mediates glioma cell invasion in vivo. J. Neurosci. *18*, 2370–2376.

Zhang, W., Couldwell, W.T., Simard, M.F., Song, H., Lin, J.H., and Nedergaard, M. (1999). Direct gap junction communication between malignant glioma cells and astrocytes. Cancer Res. *59*, 1994–2003.

Zirpel, L., Janowiak, M.A., Veltri, C.A., and Parks, T.N. (2000). AMPA receptor-mediated, calcium-dependent CREB phosphorylation in a subpopulation of auditory neurons surviving activity deprivation. J. Neurosci. *20*, 6267–6275.

STAR★METHODS

KEY RESOURCES TABLE

REAGENT or RESOURCE	SOURCE	IDENTIFIER
Antibodies		
Rabbit polyclonal anti-CD44	Abcam	Cat#ab157107; RRID:AB_2847859
Chicken polyclonal anti-GFP	Abcam	Cat#ab13970 RRID:AB_300798
Rabbit polyclonal anti-phospho-CREB	Millipore	Cat#06-519: RRID:AB_310153
Mouse monoclonal anti-Nestin	Abcam	Cat#ab22035 RRID:AB_446723
Biotinylated anti-mouse antibody	Abcam	Cat#ab6788 RRID:AB_954885
Chicken Alexa488	Invitrogen	1458638 and 2304258 RRID:AB_2534096
Rabbit Alexa647	Invitrogen	1981173 and 2299231 RRID:AB_2535813
Guinea pig Alexa647	Invitrogen	Cat#A-21450 RRID:AB_141882
Chicken Alexa647	Invitrogen	Cat#A-21449 RRID:AB_2535866
Chicken polyclonal anti-S100B	Synaptic Systems	Cat#287006, RRID:AB_2713986
Rabbit polyclonal anti-EAAT2	Synaptic Systems	Cat#250203, RRID:AB_11042312
Guinea pig polyclonal anti-NeuN	Synaptic Systems	Cat#266004, RRID:AB_2619988
Mouse monoclonal anti-beta-III-tubulin	Abcam	Cat#ab7751, RRID:AB_306045
Bacterial and virus strains		
pAAV-CamKIIa-ChrimsonR-mScarlet-KV2.1 (AAV 9)	Addgene	124651-AAV9, RRID:Addgene_124651
pAAV-CaMKIIahChR2(H134R)-mCherry (AAV2)	UNC Vector Core	N/A
pAAV-CaMKIIa-mCherry (AAV2)	Addgene	114469- AAV2, RRID:Addgene_114469
pAAV-CAG-Synaptophysin-mCherry (AAV1/2)	analogous to Wimmer et al. (2004)	N/A
Biological samples		
Patient-derived xenografts (PDX)	This paper	N/A
Chemicals, peptides, and recombinant proteins		
BAPTA-AM	Sigma-Aldrich	A1076; CAS: 126150-97-8
666-15	TOCRIS	71566396; CAS: 1433286-70-4
Gabazine	Abcam	Ab120042; CAS: 104104-50-9
CNQX	Abcam	Ab12004; CAS: 479347-85-8
Tetrodotoxin citrate	HelloBio	HB1035; CAS: 18660-81-6
Perampanel	Eisai	N/A
Perampanel	BioCrick	BCC1847; CAS: 380917-97-5

(*Continued on next page*)

Continued

REAGENT or RESOURCE	SOURCE	IDENTIFIER
0.5% Trypsin-EDTA (10x)	Gibco	15400-054
Alexa Fluor 594 hydrazide sodium salt	Invitrogen	A10442
Glutamate	Sigma-Aldrich	49449-100G
NaCl	Sigma-Aldrich	S7653
KCL	Fluka	60129
NaHCO3	Fluka	71627
NaH2PO4	Fluka	71496
L-glutamine (GlutaMAX™-I (100x))	Gibco	35050-038
B-27 Supplement for neuronal co-culture	Gibco	17504-044 10ml
Poly-L-lysine solution	Sigma-Aldrich	P4832-50ml
Rhod-2,AM	Invitrogen/ ThermoFisher Scientific	R1245MP
DMEM/D12 Medium	Life Technologies	11330032
Insulin solution human	Sigma	I9278-5ML
Heparin	Sigma	H4784-1G
B27 Supplement without vitamin A for GBC culture	Gibco	12587-010 10ml
EGF	Biotechne	236-EG-200
FGF Recombinant Protein	Life Technologies	PHG0021
FGF Recombinant Protein 1mg	Life Technologies	PHG0023
Dulbecco's PBS (1x) w/o Ca&Mg, w/o Phenol Red	Capricorn scientific	CP21-4014
Dulbecco's Phosphate Buffered Saline	Sigma	RNBJ5140
Accutase Solution	Sigma	SLCH7391
Polybrene/ Hexadimethrine bromide	Sigma	H9268-10G
FBS	Life	10500064
Triton™ X-100	Sigma-Aldrich	T9284-100ML
DAB+Chromogen	Dako	K3468
Sucrose	Sigma	S0389
Vectastain ABC-kit	Linaris/Vector	PK-4000
Alpha-D-Glucose	Serva	070937
Glucose oxidase	Serva	22778.01
Cacodylic acid-Na-salt-3H2O	Serva	15540.1
Potassium ferricyanide	Serva/Sigma	107H3450
Osmium tetroxide	Serva	31253.04
Glycid Ether 100 for electron microscopy	Serva	21045.02
MNA hardener	Carl Roth	8639.2
DMP-30	Carl Roth	8621.1
DBA Härter	Carl Roth	8623.2
DDSA	SERVA	20755.02
Propylenoxide	VWR Chemicals	27165.295
Uranyl acetate	Serva	77870
SEM pin stub (0,5"/6mm length)	Agar scientific	#G301F
Acheson silver	Plano	#3692
DAPI	Sigma	D9542
PFA 4%	Roth	P087.3
PFA 4.5%	Roth	2212.6
Sulforhodamine 101 (SR101)	Sigma Aldrich	S7635
Sulforhodamine 101 (SR101)	Invitrogen	S359
Tetramethylrhodamine isothiocyanate dextran (TRITC)	Sigma Aldrich	52194-1G

(*Continued on next page*)

Continued

REAGENT or RESOURCE	SOURCE	IDENTIFIER
SlowFade™ Gold Antifade Mountant	ThermoFischer	S36936
Experimental models: Patient-derived xenograft glioblastoma cell lines and patient-derived organoid xenograft models		
S24	This paper	N/A
BG5	This paper	N/A
BG7	This paper	N/A
P3XX	This paper	N/A
T269	This paper	N/A
P8	Golebiewska et al., 2020	N/A
P3	Golebiewska et al., 2020	N/A
P13	Golebiewska et al., 2020	N/A
T101	Golebiewska et al., 2020	N/A
T16	Golebiewska et al., 2020	N/A
T347	Golebiewska et al., 2020	N/A
T470	Golebiewska et al., 2020	N/A
T192	Golebiewska et al., 2020	N/A
T233	Golebiewska et al., 2020	N/A
Experimental models: Organisms/strains		
NMRI-Foxn1 nu/nu	Charles River and Janvier	BL210203171
WISTAR	Janvier	N/A
Recombinant DNA		
Plasmid: mGFP	Dondzillo et al., 2010	N/A
Plasmid: GCamp7-tdTomato	Dana et al., 2019	N/A
Plasmid: Twitch3A	Thestrup et al., 2014	N/A
Plasmid: GFP	Osswald et al., 2015	N/A
Plasmid: tdTomato	Osswald et al., 2015	N/A
Plasmid: dominant negative GluA2 tdTomato	Venkataramani et al., 2019	N/A
Software and algorithms		
ImageJ/Fiji	Schneider et al., 2012	https://imagej.nih.gov/ij/
NIS-Elements AR Analysis 5.30.01 64-bit	Nikon	https://www.microscope.healthcare.nikon.com/products/software
Ilastik 1.3.3 post3	Berg et al., 2019	https://www.ilastik.org/development.html
Arivis Vision4D 3.5.0	arivis AG, Munich, Germany	https://imaging.arivis.com/en/imaging-science/arivis-vision4d
R Studio 1.4	RStudio Team, 2020	N/A
AquA	(Wang et al., 2019b)	N/A
PATCHMASTER Igor Pro 6.21	HEKA	N/A
GraphPad Prism Version 9.2.0	GraphPad	N/A
Adobe Illustrator 25.4.1	Adobe	N/A
Adobe Photoshop	Adobe	N/A
ProCreate	Apple	N/A
DaVinciResolve 17	Blackmagicdesign	https://www.blackmagicdesign.com/de/products/davinciresolve/
Autodesk 3ds max	Autodesk	https://www.autodesk.de/products/3ds-max/overview
Leica Application Suite X	Leica Microsystems CMS GmbH	https://www.leica-microsystems.com/de/produkte/mikroskop-software/p/leica-las-x-ls/

(*Continued on next page*)

Continued

REAGENT or RESOURCE	SOURCE	IDENTIFIER
Zen Blue 3.5	Zeiss	https://www.zeiss.com/microscopy/int/products/microscope-software/zen.html
Zen Black 2.3 SP1	Zeiss	https://www.zeiss.com/microscopy/int/products/microscope-software/zen.html
IMOD 4.11	University of Colorado, Boulder	https://bio3d.colorado.edu/imod/
Image J 3D Viewer	Schmid et al., 2010	N/A
TrakEM	Cardona et al., 2012	N/A
Atlas 5.3.0.25	Zeiss	N/A
Single-cell and bulk RNA-sequencing datasets		
Human single-cell RNA-sequencing glioblastoma dataset	Neftel et al., 2019	GSE131928
Human single-cell RNA-sequencing glioblastoma dataset	Yu et al., 2020	GSE117891
Human bulk RNA-sequencing glioblastoma datasets	Puchalski et al., 2018	GSE107558
Xenograft single-cell RNA-sequencing gliolastoma datasets	Hai et al., 2021	N/A
Other		
FACSAria Fusion 2 Bernhard Shoor	BD	N/A
FACSAria Fusion Richard Sweet	BD	N/A

RESOURCE AVAILABILITY

Lead contact

Further information and requests for resources should be directed to and will be fulfilled by the lead contact, Frank Winkler (frank.winkler@med.uni-heidelberg.de).

Materials availability

This study did not generate new unique reagents.

Data and code availability

- Single-cell RNA-seq data used in this study are listed with accession numbers in the key resources table.
- This paper does not report original code.
- Any additional information that support the findings of this study are available on request from the lead contact.

EXPERIMENTAL MODEL AND SUBJECT DETAILS

Male NMRI nude mice and NSG (NOD scid gamma) mice (age 8-12 weeks) were used for all animal studies involving human patient-derived primary GBCs. All animal procedures were performed in accordance with the European Directive on animal experimentation (2010/63/EU) and institutional laboratory animal research guidelines after approval of the Regierungspräsidium Karlsruhe, Germany and the Animal Welfare Structure of the Luxembourg Institute of Health. Efforts were made to minimize animal suffering and to reduce the number of animals used according to the 3R principles. Mice were clinically scored and if they showed marked neurological symptoms or weight loss exceeding 10-20%, experiments were terminated. No maximum tumor size was defined for the invasive brain tumor models. Human tissues were used from patients having given informed consent and after approval of the local regulatory authorities (Ethic Committees at the Mannheim and Heidelberg Medical Faculty of the University Heidelberg, protocols (S-206/2005, S-207/2005, S-306/2019, 2018-614N-MA, 2018-843R-MA), the National Committee for Ethics in Research (CNER) Luxembourg (201201/06) and the regionale komiteer for medisinsk og helsefaglig forskningsetikk at the Helse Bergen (protocol 2013/720/REK vest). Diagnoses were molecularly confirmed with IDH1-R132H and ATRX stainings and the Illumina 850k methylation array (Department of Neuropathology, University of Heidelberg). Human patient samples were pseudonymized manually.

Patient-derived primary GBC and Illumina 850k methylation array characterization

Patient-derived tumor cell lines from resected GB were cultivated as previously described (Jung et al., 2017; Osswald et al., 2015; Venkataramani et al., 2019; Weil et al., 2017) in DMEM/F-12 under serum-free, non-adherent, 'stem-like' conditions, which includes B27 supplement (12587-010, Gibco), insulin, heparin, epidermal growth factor, and fibroblast growth factor as described previously (Osswald et al., 2015). The molecular classification of glioblastoma xenograft models used in this study can be found in Table S1. The Illumina Infinium Methylation EPIC kit was used to obtain the DNA methylation status at >850,000 CpG sites in all GBC lines, according to the manufacturer's instructions at the Genomics and Proteomics Core Facility of the German Cancer Research Center in Heidelberg, Germany, as described previously (Capper et al., 2018). The GB stem-cell lines were transduced with lentiviral vectors for membrane-bound GFP with the pLego-T2-mGFP construct based on Dondzillo et al. (2010), for calcium imaging with the pLego-T2-GCaMP7b-tdTomato based on Dana et al. (2019), Twitch3A as described previously (Osswald et al., 2015) and for dominant-negative AMPA receptor expression with the EGFP-dnGluA2 construct (Venkataramani et al., 2019; Venkatesh et al., 2019). Transduced cells were sorted regularly by FACS with either FACSAria Fusion 2 Bernhard Shoor or FACSAria Fusion Richard Sweet. The BL 530/30 filter was used for FACS-sorting GFP and Twitch3A. For tdTomato, the YG 586/15 filter was used.

METHOD DETAILS

Surgical procedures

Surgical procedures were performed as described previously (Osswald et al., 2015; Venkataramani et al., 2019). Cranial window implantation in mice was done in a modification of what we had previously described, including a custom-made titanium ring for painless head fixation during imaging. 500-900 nl of AAV viral particle for either one of the following constructs were injected cortically in 450 μm depth: neuronal channelrhodopsin expression (pAAV-CaMKIIa-hChR2(H134R)-mCherry (AAV2), UNC Vector Core or pAAV-CamKIIa-ChrimsonR-mScarlet-KV2.1 (AAV9), Addgene 124651), a viral construct used as control (pAAV-CaMKIIa-mCherry (AAV2), Addgene 114469) or pAAVCAG-Synaptophysin-mCherry (AAV1/2) (analogous to Wimmer et al., 2004) 1 to 3 weeks after cranial window implantation, 50.000-100.000 tumor cells were stereotactically injected into the mouse cortex at an approximate depth of 500 μm. Alternatively, the tumor cell injection was done in one procedure with the cranial window implantation.

General *in vivo* multiphoton laser scanning microscopy (MPLSM) and analysis

For MPLSM imaging, male NMRI nude mice older than 8 weeks (Charles River and Janvier) were operated to implant chronic cranial windows and were injected with tumor cells as described before (Osswald et al., 2015; Venkataramani et al., 2019). The tumors were intravitally observed from 3 weeks after tumor implantation with a Zeiss 7MP microscope (Zeiss), a Zeiss LSM 980 with Airyscan2 and a TriM Scope II microscope (LaVision BioTec GmbH). All microscopes were equipped with a pulsed Ti:Sapphire laser (Chameleon II ultra; Coherent). SR101, GFP, tdTomato and TRITC dextran were imaged using 850 nm and 960 nm wavelengths respectively. Twitch3A reporter GBCs were imaged at an excitation wavelength of 860 nm. Emitted fluorescence was split with a 560 nm dichroic. The Zeiss 7MP and the Zeiss LSM 980 setup were equipped with bandpass filter sets of 500 - 550 nm and 575 - 610 nm. For the TriM Scope II setup, filter sets with bandpass 500 - 570 nm and longpass 590 nm were used. For FRET imaging, only the TriM Scope II was used. Emitted fluorescence was split with a 495 nm dichroic and filtered with bandpass 460 - 500 nm and bandpass 500 - 570 nm. A 20x, 1.0 NA, apochromatic, 1.7 mm working distance, water immersion objective (Zeiss) was used for imaging at the Zeiss 7MP and the Zeiss LSM 980 setup. The TriM Scope II set up contained a 16x, 0.8 NA, apochromatic, 3 mm working distance, water immersion objective and a 25 x, 1.1 NA, apochromatic 2 mm working distance, water immersion objective (both Nikon). Fluorescence emission was detected with low-noise high-sensitivity photomultiplier tubes.

Isoflurane gas was diluted in 100 % O2 to a concentration between 0.5 - 4.0% depending on the experiment. For the induction of anesthesia, the mouse was exposed to 3-5% isoflurane, which was lowered to 0.5-3% depending on the experiment for anesthesia maintenance and monitored based on the breathing rate of the mice. Eye cream was applied to the mice after anesthesia induction. During imaging, the body temperature of the mice was monitored and kept at 37°C using a temperature sensor and a heating plate. Anesthesia was regularly evaluated during image acquisition by checking postures and breathing rates. TRITC-dextran (fluorescent conjugated tetramethylrhodamine isothiocyanate-dextran, 500.000 g/mol) was dissolved in 0.9% NaCl-solution at 10 mg/ml. Before imaging, 100 μl of TRITC solution was injected into the lateral tail vein for blood vessel visualization. Connected$^{TUM/AC}$ GBCs were classified as such if there was at least one end-to-end connected TM to another GBC manually analyzed in 3D or showed uptake of SR101. Otherwise, GBCs were classified as unconnected$^{TUM/AC}$ GBCs.

Deep learning-enabled intravital subcellular timelapse imaging (DeepISTI) workflow

An imaging and image processing pipeline was designed to enable high temporal and spatial resolution at low phototoxicity for three-dimensional *in vivo* two-photon time-lapse imaging. This workflow was developed to visualize and quantify *in vivo* GBC invasion on a subcellular level. The workflow consists of three layers: deep learning-based restoration microscopy, machine learning-based segmentation and subsequent post-processing analyses for further image enhancement and intensity normalization over time and subsequent quantification of GBC dynamics. For the deep learning-based image restoration we used the Nikon enhance.ai deep learning tool, analogous to the previously published CARE algorithms (Weigert et al., 2018). To train the enhance.ai model, pairs of 3D image stacks were acquired with low and high signal-to-noise ratios. High signal-to-noise ratio imaging stacks were imaged with a pixel

dwell time of 3.14 μs at a pixel size of 0.59 μm whereas low signal-to-noise ratio imaging stacks were imaged with the same resolution, with a pixel dwell time of 0.79 μs. For high signal-to-noise-ratio imaging stacks laser powers between 5-17 mW were measured at the objective. The laser powers used were adapted according to the z-depth. For the low signal-to-noise ratios the laser powers were reduced by 10 %. These data were used in the NIS-Elements AR Analysis software suite to train the enhance.ai model with 1000 iterations. Similar imaging conditions to the low signal-to-noise ratio imaging stacks were then routinely acquired as time-lapse imaging experiments and the enhance.ai inference was applied to restore the low signal-to-noise image stacks. Further improvement of the signal-to-noise ratio and intensity normalization over time was achieved by training the ilastik pixel classification classifier using a combination of raw images and the restored data. Indeed, both pairs of images were used to train the pixel classification workflow and obtained as a prediction the probability map of the foreground pixels (Berg et al., 2019). The ilastik probability maps trained on the combination of raw and enhanced images show the highest signal-to-noise ratio and allow analysis of subcellular structures such as TM or even small processes of GBCs *in vivo* over time. These data can then be further processed and for instance be used for tracking TM dynamics or to perform somatokinetic measurements as described below.

In vivo 3D time-lapse experiments with isoflurane anesthesia experimental paradigms using MPLSM

Tail veins were injected with TRITC-dextran under isoflurane anesthesia. Before time-lapse imaging, a stable respiratory rate (RR) was established by manual monitoring of breathing over 15 seconds with an application (Tap BPM https://www.beatsperminuteonline.com/). Deep anesthesia corresponded to a mean respiratory rate < 60 bpm, while light anesthesia corresponded to a mean respiratory rate > 100 bpm. Once a stable respiratory rate was established, a field of view with a volume of 607.28μm x 607.28μm x 100μm, was selected and the image stack was repetitively imaged over 4h every 5 min resulting in a total of 48 time points. The laser power was chosen at 90% of the optimal amount according to the built-in range indicator function of Zen to reduce laser power and avoid phototoxicity. Visible drift during time-lapse imaging was corrected manually after image acquisition of each stack in xyz directions. The respiratory rate was monitored after each stack as described above and the isoflurane concentration was adapted if needed to adjust the respective breathing rates as readout for anesthesia depth. After imaging, the mice were observed carefully until they woke up and injected s.c. with 1 ml 0.9% NaCl-Glucose-solution for the prevention of dehydration.

The 48 stacks for each time point were hyperstacked and registered in Fiji via the vessel signal and by using the plugin Correct 3D drift (Parslow et al., 2014).

Intravital neuronal channelrhodopsin stimulation and GBC imaging

To analyze the effect of neuronal stimulation on TM dynamics and GBCs, neurons infected with AAV particles expressing CaMKIIahChR2-mCherry (experimental group) or CaMKIIa-mCherry (control group) (see 'Surgical procedures') were stimulated with 473 nm laser light (Shanghai Laser & Optics Century Co. Ltd, China) via an optical fiber (Laser Components, Item 3016347). Cells were stimulated 15 times at 20 Hz for 30 s using 90 s pause intervals as described previously (Venkatesh et al., 2015). The PMT shutter of the TriM II MPLSM was closed during stimulation. Stimulation and shutter were controlled using a PulsePal device and a custom written MATLAB script (Venkataramani et al., 2019). Afterwards, the same tumor microregions were repetitively imaged every five minutes for four hours in analogy to the above-described experimental paradigm using isoflurane anesthesia.

SR101 *IN VIVO* IMAGING

For all SR101 *in vivo* imaging, SR101 dissolved in 1x phosphate buffered saline (Sigma) was injected intraperitoneally at a dosage of 0.12 mg per g bodyweight as described previously (Xie et al., 2021). To determine SR101 uptake in GBCs, four experimental paradigms were used. In the first experimental paradigm, *in vivo* 3D time-lapse stacks of GBCs over the course of four hours were acquired (see '*In vivo* 3D time-lapse experiments with isoflurane anesthesia experimental paradigms using MPLSM'). SR101 was intraperitoneally injected directly after the experiment and a 3D stack of the respective tumor microregion was acquired after six to eight hours. The 3D stack (3.15 μs pixel dwell time, 0.59 μm pixel size) was acquired in the same field of view (FoV) as for the previous time-lapse experiment. These stacks were then concatenated with the time-lapse images from the invasion experiment to clearly identify the same cells for subsequent analysis.

To analyze dynamic SR101 uptake in GBCs and glial cells, SR101 was injected into the mice at the same dosage stated above and after approximately 1.5h, the chosen FoV was imaged once every 5 min for 4 h (volume of FoV = 607.28 um x 607.28 μm x 100 μm, pixel size 0.59 μm, 0.79 μs pixel dwell time). A mean respiratory rate of >100/min was aimed for and the respiratory rate was monitored after each stack. The isoflurane concentration was adapted accordingly. After imaging, mice were injected s.c. with 1 ml 0.9% NaCl-Glucose-Solution and observed until awake. The stacks were hyperstacked and registered as described above.

In the third experimental paradigm, uptake of SR101 in GBCs was weekly determined. SR101 was injected each week as described above six to ten hours prior to two-photon microscopy imaging.

In the fourth experimental paradigm, SR101 uptake in GBCs and its inhibition by the gap junction inhibitor carbenoxolone was determined by direct injection of SR101 into tumor regions.

Specifically, 50 nl of 100 μM SR101 and 100 μM carbenoxolone (CBX, Sigma-Aldrich, C4790) were injected under isoflurane anesthesia through a thin glass pipette into the selected tumor regions with similar tumor density > 90 days after tumor injection. For the control experiments, CBX was omitted. The images were acquired 120 minutes after the microinjection.

SR101 signal intensity was measured in 3D image stacks by selecting the cell soma boundary in Fiji (Schindelin et al., 2012) with the Polygon selection-tool in a slice with maximum extension in the x/y-axis and measuring the mean grey value in the SR101 channel.

For the SR101 intensity analyses, the results measured over time for GBCs and astrocytes were either normalized by subtracting the mean background intensity per time point, mean SR101 intensity values were normalized per dataset by dividing by the mean background intensity measured in various positions of the 3D image stack or by subtracting a filtered image of the raw data (Gaussian Blur with a sigma (radius)=20) from the raw data.

In vivo imaging of synaptophysin and GBCs

For the synaptophysin punctae tracking, 500-900 nl of AAV particles expressing the presynaptic vesicle marker synaptophysin (pAAV-CAG-Synaptophysin-mCherry (AAV1/2)) were injected into the mouse cortex at a depth of 400 μm prior to tumor cell injection during the chronic cranial window implantation as described above. Synaptophysin is a synaptic vesicle marker and allows to reliably identify presynaptic boutons that can be distinguished with confocal microscopy as punctae in the range of 0.4-4 μm (Fantuzzo et al., 2017). Three to six weeks after surgery, experiments were performed. Imaging of GBCs and respective synaptophysin punctae was repeated, with a minimal time interval of 1 hour between the first and the last time point (pixel size = 0.21 μm, pixel dwell time = 4.73 μs).

After image acquisition, the images were denoised using Denoise.ai within Nikon NIS- Elements AR Analysis. To determine putative neurogliomal synapses, we first segmented GBC that were fluorescently labeled with mGFP as well synaptic boutons with interactive machine learning (Berg et al., 2019) and a subsequent watershed algorithm in Arivis Vision 4D. Next, we used the direct overlap of signal coming from the segmented synaptic boutons and GBCs which allows the identification of putative neurogliomal synapses. Usually, distance thresholds commonly used for determining synaptic connectivity in *ex vivo* analyses with confocal imaging 0.7-2.5 μm (Fogarty et al., 2013; Schätzle et al., 2012). Thus, the chosen workflow should enable a more reliable identification of putative neurogliomal synapses.

In vivo calcium imaging with Rhod2-AM

For simultaneous *in vivo* calcium imaging of GBCs and astrocytes, the following small molecule calcium indicators were applied to the brain surface for 45 minutes as described before (Osswald et al., 2015) based on previous published protocols (Kantevari et al., 2011; Takano et al., 2006): for GFP-transfected tumor cells, 2 mM Rhod-2AM (Life Technologies, R-1244); for RFP-transfected, 2 mM Fluo-4AM (Life Technologies, F-14201). Subsequent *in vivo* calcium imaging was performed as described previously (Osswald et al., 2015).

In vivo imaging of dominant-negative AMPAR and control GBCs

In vivo imaging of dominant-negative AMPAR and control GBCs was performed as described previously (Venkataramani et al., 2019).

Previously, we validated the dominant-negative AMPAR in HEK cells transfected with GluA2-eGFP and dominant-negative GluA2-tdTomato as compared to cells transfected with GluA2-eGFP alone. As previously described, glutamate-induced peak currents were significantly inhibited when HEK cell were transfected with both GluA2-eGFP and dominant-negative GluA2-tdTomato (Venkataramani et al., 2019).

3D *in vivo* calcium imaging with intravital MPLSM and image analysis

3D *in vivo* calcium imaging was performed to cover whole GBC calcium dynamics with a sufficient time resolution to capture calcium microdomains, whole cell and multicellular calcium events. Cells were centered in the field of view and their maximum z range was determined. The piezoelectric objective z-actuator was used to repetitively acquire z stacks over a range of 15-25 μm with a z step size between 3-5 μm and a frequency of 0.3-0.5 Hz.

To analyze the effect of neuronal stimulation on GBC calcium dynamics, neurons expressing CaMKIIahChR2-mCherry or CamKIIa-ChrimsonR-mScarlet after AAV infection (see 'Surgical procedures') were stimulated with 473 nm laser light (Shanghai Laser & Optics Century Co. Ltd, China) via an optical fiber (Laser Components, Item 3016347). For 3D *in vivo* calcium imaging, regions were stimulated at 40 Hz for 1 s with 1 min intervals between stimulations for five minutes. Baseline activity was recorded for five minutes beforehand. Pulsed illumination at 40 Hz for 1 s was an effective trigger for calcium transients in GBCs as described previously (Venkataramani et al., 2019).

The maximum intensity projection (MIP) of the z-stack was used for further analysis. The time-lapse MIP stack was motion corrected using the ImageJ/Fiji plugin moco (Dubbs et al., 2016). Calcium events in motion-corrected stacks were analyzed using AquA (Astrocyte Quantification and Analysis) (Wang et al., 2019b).

General image processing

Image processing was primarily performed in ImageJ/Fiji (e.g. to reduce and remove unspecific background by subtraction of different channels, filtering with a median filter or the 'Remove Outlier') (Schindelin et al., 2012).

Arivis Vision 4D and ImageJ/Fiji were used for 3D and 4D Image visualization. Image restoration was performed using the enhance.ai tool within the Nikon NIS-Elements AR Analysis software v5.30.01 (Nikon GmbH Germany/Laboratory Imaging) as described above. Confocal Laser Scanning Microscopy (CLSM) images and *in vivo* imaging data were denoised using the denoise.ai

pretrained model and enhance.ai (see 'Deep learning-enabled intravital subcellular time-lapse imaging (DeepISTI) workflow') in the Nikon NIS-Elements AR software v5.30.01 (Nikon GmbH Germany/Laboratory Imaging). Videos were produced in DaVinci Resolve 17.

Dynamics measurement and directionality change analysis of GBC processes

Tumor microtube dynamics were tracked using MTrackJ (Meijering et al., 2012). Each tumor cell process was tracked separately for all time points, and subsequent TM dynamics quantification was performed using custom-written scripts in RStudio (Version 1.2.5033). The directionality change of the leading TM was calculated by comparing the direction of the leading TM at time point 0 and after 4 hours. The directions of the TMs were used as vectors. The angle between the two vectors was determined with ImageJ/Fiji (Schindelin et al., 2012).

Somatokinesis measurement

Measurement of somatokinesis was performed in ImageJ/Fiji (Schindelin et al., 2012). Cells were cropped and registered using the 3D Drift Correction plugin in ImageJ/Fiji (Parslow et al., 2014). The cell somata were outlined and the center point of the selection was determined using the centroid function. The distance between the center points of two time points was divided by the experimental observation time to calculate the somatokinetic speed.

Measurement of TM turnover

The tips of TMs were manually tracked over time with MTrackJ (Meijering et al., 2012). Subsequently, the steps between each time point of these tracks were extracted. The TM turnover per single TM was determined by adding up the distances between the single steps and dividing this number by the experimental observation time and referred to as TM turnover per TM to sum up the dynamics of single TMs. The TM turnover per GBC was determined by tracking all TMs of a cell, adding single steps up and divide this number by the experimental observation time and the number of TMs. The total TM turnover per GBC was determined by tracking all TMs of a cell, adding single steps up and divide this number by the experimental observation time.

TM turnover per TM was used to investigate the heterogeneity of TM dynamics in blind TMs as compared to 4 connected TMs. To characterise the TM turnover of the three different invasion phenotypes, the total TM turnover per GBC was analyzed. For this purpose, the TM turnover of all TMs per cell was added up. To determine the effects of neuronal stimulation, effects on TM dynamics of whole GBCs were determined. As neuronal stimulation also increased branching TM generation, TM turnover was normalized in addition to the TMs per cell.

Classification of TM

The TMs of GBCs were analyzed in three-dimensional imaging stacks to determine whether they were connected or ended blindly: Only end-to-end connections between TMs or TM connected with GBC somata were classified as connected TMs, all other TMs were classified as blindly ending TMs.

Classification of GBC small processes

Filopodial structures were defined as structures shorter than 10 μm and thinner than 1.25 μm. Structures that were shorter than normal TMs (10 μm), but exhibiting TM diameters from 1.25 μm to 3 μm were classified as TM-like structures. Short structures that were thicker than normal TM (> 3 μm) were classified as lamellipodia like structures.

FACS sorting and scRNA Seq

To distinguish between connected$^{TUM/AC}$ and unconnected$^{TUM/AC}$ GBCs in fluorescent (GFP) PDX models, 0.12 mg/g body weight SR101 injected i.p. into tumor bearing mice prior to perfusion as described previously (Xie et al., 2021). The perfused brain was dissolved into a single cell suspension by using the brain tumor dissociation kit and device by Miltenyi as described before (Xie et al., 2021). The samples were stained with a dead cell marker (TO-PRO3) and a live cell marker (Calcein Violet 450 AM) to identify the vital cell population. The single cell suspension was sorted with a FACSAria Fusion 2 Bernhard Shoor or a FACSAria Fusion Richard Sweet (BD Biosciences). Tumor cells were identified by the GFP signal measured with the filter BL-530/30 and the SR101 signal was determined with the filter YG-586/15. Lasers with wavelengths of 488 nm, 561 nm and 640 nm were used for this purpose. Tumor cells were gated into connected$^{TUM/AC}$ (SR101 high) and unconnected$^{TUM/AC}$ (SR101 low) groups as described previously (Xie et al., 2021).

Xenograft single-cell RNA-seq data generation and processing

Xenograft single-cell RNA-sequencing data were taken from Hai et al. (2021). Gene expression count matrices were generated and aligned with Cell Ranger (v.2.1.1, 10X Genomics). Quality controls were performed as described previously (Hai et al., 2021).

Human scRNA-seq datasets

The Yu dataset (Yu et al., 2020) was obtained from the Gene Ontology Omnibus (GSE117891). Cells that were classified as tumor cells as described previously (Garofano et al., 2021) were used for the subsequent analysis presented in this manuscript. Data was

normalized and scaled in Seurat (Stuart et al., 2019). Principal components were calculated using RunPCA. The Neftel dataset (Neftel et al., 2019) was obtained from the Gene Ontology Omnibus (GSE131928).

Definition of single-cell invasivity signature and AMPAR scores

Cell cycle scoring was performed on the three PDX models and their scores were regressed out in Seurat. After scaling and centering, principal component analysis was performed. Data was visualized with UMAP using the first ten principal components. Using Monocle3 (1.0.0) (Cao et al., 2019), cells were clustered and the graph was learned based on the reduced dimensions using the learn graph function. Subsequently, cells were ordered using the order_cells function where root nodes were set to the unconnected$^{TUM/AC}$ cells of each cell line. Pseudotime was inferred for each cell. For all genes, expression was correlated to pseudotime using the stats::cor function. For each cell line, genes whose absolute value of their correlation coefficient was higher than 0.2 were further analyzed. Genes that were correlated or anticorrelated in the same direction in two cell lines were kept. The expression levels for correlated and anticorrelated genes were calculated separately by using the AddModuleScore function for each group of genes. For each cell, the score calculated for the correlated genes was subtracted from the score calculated for the anticorrelated genes to compute the invasivity score. For further validation of the gene sets defining the invasivity score, GeneCards information was downloaded from GeneCards using batch inquiries at GeneALaCart (Stelzer et al., 2016).

For the AMPAR gene expression score all four AMPAR genes GRIA1, GRIA2, GRIA3 and GRIA4 were used using the AddModuleScore function in Stuart et al. (2019).

Validation of the Invasivity Score

Nine patient-derived orthotopic xenograft (PDOX) models representing invasive, intermediate and angiogenic growth phenotypes were derived as described in Golebiewska et al. (2020) following the protocol presented in Oudin et al. (2021). Shortly, primary organoids were derived from mechanically minced IDH-wildtype GB tumor tissue. Organoids were cultured shortly in DMEM medium, 10% FBS, 2mM L-Glutamine, 0.4 mM NEAA, and 100 U/ml Pen–Strep (all from Lonza) for maximum 12 days. Organoids were implanted intracranially to immunodeficient mice and tumor development was monitored by MRI. Tumor development was validated by IHC using an anti-vimentin antibody (Thermo Fisher Scientific, Mab3400), vasculature was monitored with mouse-specific anti-CD31 antibody (Millipore, CBL1337). Tumors were dissociated with the MACS Neural Dissociation kit (Miltenyi Biotec). Human tumor cells were purified with FACS (as human-specific CD90$^+$ cells) or MACS with Mouse Cell Depletion kit (Miltenyi Biotec). Single cell RNA-seq based on Drop-seq or 10xGenomics technology was performed on purified human tumor cells as described before (Dirkse et al., 2019) and according to the manufacturer's protocol. scRNA-seq data is available at Omnibus repository (https://www.ncbi.nlm.nih.gov/geo/) under accession number GSE128195.

GO Term Analysis and GO Term Clustering

Gene sets of differentially expressed genes based on anatomic regions were used from previously published work (Puchalski et al., 2018). Gene sets were analyzed in Cytoscape (Version 3.8.2, Java 11.0.6) (Shannon et al., 2003) using the Biological Networks Gene Ontology tool (BiNGO, Version 3.0.4) (Maere et al., 2005). Overrepresented GO Terms within the Biological Process Ontology were calculated by using a hypergeometric test as statistical test and the Benjamini & Hochberg False Discovery Rate (FDR) Correction to correct for multiple testing. Additional GO term analyses were performed using ShinyGO (Ge et al., 2020).

Transcription factor analysis using SCENIC

Transcription factor analysis was performed using the python implementation of SCENIC (Van de Sande et al., 2020). Gene regulatory networks were inferred using the GRNBoost2 algorithm of SCENIC. Enriched motifs were identified and regulon prediction was performed using the CLI ctx function. The enrichment of regulon activity for each cell was calculated using the AUCELL algorithm. Results were integrated into Seurat (Stuart et al., 2019).

In vitro co-culture

Primary cultures of rat cortical neurons and astrocytes were prepared as described previously (Venkataramani et al., 2019). In brief, the cells were cultivated from E19 embryos and plated at a density of 90,000 cells/cm^2 on 12 mm coverslips in 24-well plates coated with poly-L-lysine and maintained in neurobasal medium (Invitrogen) supplemented with B27 supplement (50x) (2% v/v) and L-glutamine (0.5 mM). After 7 days *in vitro* (DIV), mechanically dissociated, patient-derived primary GBCs (1000 per well) were added and co-cultured in medium. For electrophysiology and live-cell imaging GBCs (DIV 4-28) were used.

Drug treatment in co-cultures with neurons, astrocytes and GBCs

After seeding 1000 GBC onto E19 rat cortex neurons (DIV 7) in 24 well plates and waiting 4-7 days, they were incubated with BAPTA-AM (Sigma-Aldrich; reaching a culture medium concentration of 1,2 μM), 666-15 (Tocris, reaching a culture medium concentration of 1μM) or DMSO as control. After 12-hour incubation, well plates were imaged using a LSM 710 confocal microscope with a 10x (NA 0.3) objective in 37 degrees Celsius and 5% CO_2 every 10 minutes for a period of 9-12 hours.

For live-cell imaging experiments, gabazine (Abcam, reaching a culture medium concentration of 4μM) was added prior to imaging to inhibit $GABA_A$ receptor activity, thus disinhibiting neuronal activity and leading to neuronal stimulation and epileptiform neuronal activity (Margineanu and Wulfert, 1997).

Seeding of S24 GBCs was done as described before, with S24tdTomato and S24GluA2Q dominant negative tdTomato cells (Venkataramani et al., 2019). 5-10 days after seeding, cells were imaged in baseline live cell (5% CO_2, 37 degrees Celsius) conditions using a Zeiss LSM 710 confocal microscope with a 10x (NA 0.3) objective. After 4 hours, perampanel (BioCrick, reaching a culture medium concentration of 60μM) was applied and imaged for the same time period.

All images were acquired with a pixel size of 346nm in xy with a fully open pinhole and subsequently analyzed manually with ImageJ/Fiji (Schindelin et al., 2012).

Simultaneous *in vitro* co-culture calcium imaging and time-lapse imaging of GBC

For *in vitro* calcium imaging the genetically encoded calcium indicator jGCaMP7b (Dana et al., 2019) was used. GBCs in our co-cultures were identified by the tdTomato signal.

For live cell imaging, co-culture coverslips (DIV 5-12) were immersed in 2ml neurobasal medium supplemented with L-glutamine (0.5 mM) and B27 supplement (50x). Coverslips were imaged for 100 minutes at 37 degrees Celsius with 5% CO2 using a 20x objective of Leica TCS SP8 confocal microscope with a numerical aperture of 0.75. Images were acquired with a pixel size of 445,63 nm in xy with a fully open pinhole and an image frequency of 1 Hz in a bidirectional acquisition mode.

Glutamate puffing and simultaneous calcium imaging

1000 GBCs were seeded onto rat cortical neurons (DIV 7). After 5-12 days, coverslips were transferred to an upright confocal setup and perfused with carbonated aCSF at 35°C. Simultaneous calcium imaging and puffing was performed. For image acquisition, a TCS SP5 Leica microscope equipped with a 20x water immersion objective (NA 1,0) and a Luigs and Neumann stage was used. Images were acquired with a pixel size of 0,2 μm and 1,3 μm with a frequency of 1,56 Hz in a bidirectional xyt acquisition mode. For simultaneous puffing and calcium imaging, Patchmaster software (HEKA) was used for triggered puff recordings, with a puff applied every 45 s. Puffs were generated at 10-15 PSI using a Picospritzer. Pipettes for puffing were fabricated from borosilicate capillaries (World Precision Instruments) and had resistances of 2-7 MΩ. For all co-culture experiments, aCSF with 1 μM tetrodotoxin (TTX) was used to exclude that action potentials of neurons are evoked by the puffing of glutamate. Puffing was performed as follows: Glutamate puffing, aCSF puffing, drug wash-in for 7 min 30 s, i.e. CNQX (Abcam; reaching an aCSF concentration of 20 μM) /TTX (HelloBio; reaching an aCSF concentration of 1 μM) or BAPTA-AM (Sigma-Aldrich; reaching an aCSF concentration of 1,2 μM) /TTX (HelloBio; reaching an aCSF concentration of 1 μM)) respectively, calcium imaging under pharmacologically altered conditions, CNQX/TTX wash-out (7min 30 s) and in the case of CNQX/TTX calcium imaging after wash out with continuous glutamate puffing after aCSF puffing control. Total recording time per imaging series was 3 min 45 s with 5 puff stimulations. Data were analyzed using ImageJ/Fiji (Schindelin et al., 2012) and AQuA (Wang et al., 2019b). Correlated calcium transients were defined as transients occurring within 20 s or less after glutamate stimulation. GBCs in which ACSF puffing could evoke calcium transients were excluded from the analysis.

In vitro co-culture imaging of synaptophysin and GBCs

For the *in vitro* synaptophysin punctae tracking, cortical rat neurons (DIV 7) were transduced with 1μl of AAV particles expressing the presynaptic vesicle marker synaptophysin (pAAV-CAG-Synaptophysin-mCherry (AAV1/2)). Three days after neuronal infection, S24GFP GBCs were seeded onto cortical neurons.

Seven days after seeding, these co-cultures were imaged in glass bottom dishes using a TCS SP8, Leica with a 40x objective (NA 1.1) and pixel size of 94,7 nm in xy. They were observed over a period of two hours with a 15-minute interval.

Image processing and analysis were done as described above for the *in vivo* imaging analysis (see '*In vivo* imaging of synaptophysin and GBCs').

Sample preparation, microscopy and analysis for correlative light and scanning electron microscopy (SEM)

For *ex vivo* analyses of PDX models the mice were anesthetized with either ketamine/xylazine or pentobarbital i.p. First, mice were perfused transcardially with PBS followed by 4-4,5% PFA (w/v) in 1x PBS. After the removal of the brain, it was postfixed in 4% PFA overnight and kept in PBS at 4°C. Serial sections of 70-100 μm were cut with a semiautomatic vibratome (Leica VT1000s). The expression of fluorescence (mGFP or cytosolic GFP) in the GBCs of the PDX models was checked under a wide field fluorescence microscope (Leica DM6000) and slabs of ~400 μm x 400 μm in size were dissected.

For the nestin antibody staining, the human slices were put into 10% (w/v) sucrose (Sigma) dissolved in PBS for 10 minutes. Subsequently, the concentration was increased and slices were stored in 30% sucrose solution for 12-15h. To prepare the infiltration of the antibody, slices were freeze-thawed in liquid nitrogen twice for 5 seconds. As a blocking solution, 5% FBS in PBS was used for 1 hour at RT. The slices were incubated overnight at 4°C with human-specific mouse anti-nestin antibody in blocking solution and washed three times in PBS. The samples were stained in 3,3'-diaminobenzidine (DAB) precipitate. For the DAB precipitate labeling, slices were incubated for 12-15h at 4°C with secondary AB, a biotinylated anti-mouse AB (Abcam (ab6788), 1:500, in blocking solution). Slices were washed in PBS three times and then incubated in Vectastain ABC-kit (Linaris) for 1h at RT. Incubation in glucose-

DAB-solution (glucose: 2mg/ml, DAB: 1.4mg/ml, dissolved) followed. After another hour of incubation in glucose-DAB oxidase solution (glucose oxidase: 0.1 mg/ml, Serva) the electron dense precipitate could be assessed under a wide field light microscope.

For correlative light and electron microscopy (CLEM), the sections were stained with DAPI (1:1000) for 1 hour and subsequently imaged under a Leica TCS SP8 confocal microscope with a 63X objective (NA 1.4) and a 20X (NA 0.75) a with a pixel size of 200 nm in a z-stack taking an image at every 520 nm with a scanning speed of 400-600Hz. The sections were washed in PBS and in cacodylic buffer (100 mM, pH 7.4, (Serva)) (SERVA#15540.1 Cacodylic acid-Na-salt-3H2O, 100mM, pH 7.4) at 4°C. For post-fixation and contrasting it was incubated in 1.5% potassium ferricyanide (Serva) and 2% osmium tetroxide (Serva) for 1h on ice. Next, the sections were rinsed three times with dH2O and then put on a spinning wheel for 30 minutes. The sections were dehydrated in solutions of increasing ethanol concentrations (70%/95%/100%). The samples were subsequently embedded in resin as described previously (Horstmann et al., 2012). The self-produced Epon consisted of 455.8 mg/ml Glycidether 100/E812, 308.6 mg/ml DDSA, 235.4 mg/ml MNA hardener and 0,015 ml/ml DMP-30/BDMA. Sections were then infiltrated in a 1:1 mixture of propylenoxide and Epon (Serva) for 12-15h at 4°C, followed by three times rinsing in fresh Epon 100% and embedding in epoxy resin. The sample blocks were polymerized at 60°C for at least 24 hours. Afterwards, the blocks were trimmed with the Leica EM-trim and fine trimming into a trapezoid form was performed with a razor blade. For CLEM, the whole tissue block was cut with a custom-modified ultramicrotome (Ultracut S, Leica) using a diamond knife (DIATOME Ultra 45°) (Horstmann et al., 2012). Serial sectioning of the whole sample (70-100 um) with 40-70 nm slices resulted in up to 30 wafers with up to 100 sections per wafer. While cutting, the bottom side of the trapezoid-shaped sample was coated with a thin layer of Patex glue (Henkel, Düsseldorf, Germany) and Xylene (1:3) to give the long ribbon more stability and connectivity on the water surface in the knife boat.

After drying, the wafers were poststained with uranyl acetate (3%) in a closed dark reaction tube for 16 minutes followed by rinsing shortly in dH2O for three times. A modified Reynolds-procedure was used as previously described (Horstmann et al., 2012; Reynolds, 1963; Venkataramani et al., 2019). Here, wafers were incubated with a lead citrate solution for 8 minutes at room temperature in a closed reaction tube to avoid contact with carbon dioxide. Subsequently, the wafers were dried at 60°C for 30 min. The wafers were mounted on SEM pin stubs (0,5''/6mm length #G301F; agar scientific, Essex UK) with Acheson silver (#3692, Plano, Wetzlar, Germany).

For the correlation of GBCs with light microscopy and electron microscopy, overview images of single sections were acquired with scanning electron microscopy to locate the corresponding level in the light microscopy stack. Fluorescent GBCs were identified by the cell/nucleus morphology and the spatial arrangement of the DAPI signal. The exact light microscopic level was unequivocally identified with an overlay of EM and LM with TrakEM2 (Cardona et al., 2012).

For image acquisition, a LEO Gemini 1530 scanning electron microscope (Zeiss) and an Auriga (Zeiss) scanning electron microscope were used in combination with an ATLAS scan generator (Zeiss). The working distance was set to 2-3 mm and the aperture to 20 μm. The acceleration voltage was set to 2 kV. For the 3D reconstructions, images were taken at the same spot in consecutive slices. A stack was created with extensions in z with steps of 70-280 nm. Pixel sizes between 2 and 5 nm, a pixel dwell time of 12.8 μs and FoVs ranging from 100 μm^2 to 2400 μm^2 were used as imaging parameters. The acquisition time differed from 3 to 75 minutes. For larger overview images, the FoV size was increased up to 1 mm^2 with a pixel size of 30 nm. Connected$^{TUM/AC}$ and unconnected$^{TUM/AC}$ cells were defined based on morphological connectivity. Direct synaptic contacts formed onto GBCs were counted as such if 2 out of 3 criteria were met: (1) synaptic vesicle cluster present, (2) synaptic cleft visible, (3) postsynaptic density (PSD) apparent. For the analysis of the synapses, EM-sections were reacquired at 2 nm pixel size on each 70nm-section. Manual segmentation of the synaptic bouton was performed in TrakEM2 (Cardona et al., 2012). Ultrastructural morphometric synaptic features were analyzed using custom-written scripts in ImageJ/Fiji. The diameter of the synaptic vesicles was measured at the maximum extent in the 2D-section. The boundaries of the cells/synaptic boutons were manually segmented and imported as area lists on consecutive EM-sections in TrakEM2 (Cardona et al., 2012). 3D visualization of the structures was performed in Fiji 3D Viewer (Schmid et al., 2010). Meshes were smoothed and the areas were interpolated in z-dimension. The smoothed model was exported to Autodesk 3DS MAX for further visualization.

Sample preparation and immunohistochemistry for confocal imaging of PDX mice

Following deep anesthesia with isoflurane, xenograft mice were transcardially perfused with 4% (w/v) PFA dissolved in 1x phosphate buffered saline (PBS, Sigma or Gibco) after >3 months of tumor growth or showing of symptoms. Brains were collected and postfixed in 4% PFA overnight before transfer to a DAPI (1:10000) solution in PBS. Preparation of serial 80 μm thick tissue sections was performed using a Leica VT000S vibratome.

Permeabilization of sections was performed with 5% (v/v) fetal bovine serum (FBS) and 1% (v/v) Triton X-100, shaking, for 2 hours at RT. Following, primary antibodies were applied in a 1% FBS and 0,2% Triton X-100 blocking solution and incubation at 4° Celsius overnight, shaking. Before applying appropriate secondary antibodies, 3x washing steps for 15 min with a 2% FBS solution at RT was performed. Secondary antibodies were then coupled to chicken Alexa488 (Invitrogen) and rabbit Alexa647 (Invitrogen) with a dilution of 1:500 (same solution as the primary antibodies) and incubated for 3 hours. Before mounting, the sections were washed first 3x with a 1% FBS solution and then three times with PBS for 10 minutes at RT. Mounting was performed with ''SlowFade Gold'' solution.

Images were acquired using a 63x immersion oil objective with a numerical aperture of 1.4 at a confocal laser-scanning microscope (TCS SP8, Leica microsystems and LSM710 ConfoCor3, Zeiss). The pixel size of the acquired images was 141 nm or 220 nm and the z step size was 300 nm.

Validation of CREB phosphorylation in co-cultures

To validate the phosphorylation of CREB (Gonzalez and Montminy, 1989) in GBCs after neuronal stimulation, DIV5-12 GBC co-cultures were incubated with gabazine (Abcam, reaching a medium concentration of 4μM), CNQX (Abcam, reaching a medium concentration of 20μM) together with TTX (HelloBio, reaching a medium concentration of 1μM) or DMSO for 4 hours. Next, the coverslips were fixated in methanol at -20° Celsius for 5 minutes and subsequently blocked in 5% (v/v) fetal bovine serum FBS solution for 10 minutes at RT. Following,the primary antibody (anti-phospho-CREB, Millipore, 1:100 dilution) was applied in a 5% FBS solution and incubated for 1 hour at RT, shaking. Before applying appropriate secondary antibodies, 3x washing steps for 5 min with a 5% FBS solution at RT were performed. 1:500 diluted appropriate secondary antibodies were applied in a 5% FBS solution and incubated for 1 hour at RT, shaking. Before mounting, the coverslips were washed first 3x with a 5% FBS solution and then three times with PBS for 5 minutes at RT, shaking. Mounting was also performed with "SlowFade Gold" and DAPI (1:10000 dilution in PBS). Confocal images were acquired as described for PDX brain sections.

Sample preparation of human tissue for immunohistochemistry

Human biopsy tissue was immersion fixed with 4% PFA overnight as previously described (Venkataramani et al., 2019). Afterwards, the tissue was washed in PBS and subsequently serially cut to 100 μm thick tissue sections using a Leica VT000S vibratome and stored in PBS. The staining of the sections was done as described above. To visualize tumor cells a mouse anti-nestin antibody (Abcam, ab22035) was used. A secondary antibody coupled with Alexa 488 against mouse was subsequently used. Sections were stained with DAPI to simultaneously visualize nuclei. Images were acquired using a 40x immersion oil objective of a confocal laser scanning microscope (LSM710 ConfoCor3, Zeiss) with a numerical aperture of 1.3. Images were acquired with a pixel size of 350 nm and a z step size of 390 nm.

Morphometric analysis of somata and TM in human tissue and PDX mice

3D rendering and analysis of the *in vivo* two photon microscopy images of PDX mice and confocal microscopy images of fixed human GB tissue were done using Arivis Vision 4D. Tumor cells were semiautomatically segmented using the 'Magic Wand' function. Somata and TMs were manually split and annotated using the 'Splitting Tool'. Features, such as volume and surface area, were exported for further morphometric comparison.

Morphometric interaction analysis of somata and TMs with neurons

First, each channel of the confocal images was segmented with a machine-learning based pixel classification using ilastik (Berg et al., 2019). 3D Rendering and image analysis were done using Arivis Vision 4D. A custom pipeline was built from existing analysis features to automatically threshold and segment the beta-III-tubulin signal, a pan-neuronal marker (Sullivan and Cleveland, 1986), from immunohistochemistry. The tumor cells of interest were segmented manually into somata and TMs, and annotated accordingly as described above. Afterwards, the direct overlap of tumor cell signal to neuron signal was automatically determined. Features such as volume and surface area of the detected contacts were exported for further comparisons.

Acute brain slice preparation

Brain tumor-bearing mice were deeply anesthetized, rapidly decapitated, and the brain was removed in ice-cold slicing solution containing (in mM) 125 NaCl, 2.5 KCl, 25 NaHCO3, 1.25 NaH2PO4, 10 glucose, 75 sucrose, 0.5 CaCl2, 7 MgCl2, adjusted to ~340 mOsm, and aerated with carbogen (5% CO2in O2). 300 μm thick coronal slices were prepared on a vibratome (VT1200S; Leica) and stored in the same solution for 30 min at 37°C. Afterwards, acute slices were transferred into a custom-made incubation system, where slices were slowly cooled down to 16°C and the circulating slicing solution was irradiated with UV light, to extend slice viability as described previously (Venkataramani et al., 2019). 30 minutes before electrophysiological recordings, slices were warmed up to RT in artificial cerebrospinal fluid (aCSF) containing (in mM) 87 NaCl, 2.5 KCl, 25 NaHCO3, 1.25 NaH2PO4, 13 glucose, 2 CaCl2, 1 MgCl2, aerated with carbogen (5% CO2in O2).

Electrophysiology

All experiments were performed on a Leica TCS SP5 Confocal Microscope equipped with a Luigs and Neumann stage and a water-immersion objective (20x, NA 1.0) as previously described (Venkataramani et al., 2019). GBCs were unequivocally identified by their endogenous EGFP or tdTomato-fluorescence, respectively, and subsequently targeted for whole-cell patch-clamp recordings. Acute brain slices and co-cultured plates were constantly perfused with artificial cerebrospinal fluid (aCSF), containing (in mM): 125 NaCl, 2.5 KCl, 25 NaHCO3, 1.25 NaH2PO4, 13 glucose, 2 CaCl2, 1 MgCl2. The aCSF was permanently aerated with carbogen and heated to 35°C. For the analysis of epileptiform, neuronal activity in co-cultures of neurons, astrocytes and GBCs, gabazine (4 μM) was perfused in aCSF and subsequently neurons were targeted with whole-cell patch-clamp electrophysiology. For the analysis of anti-epileptic effects of perampanel (Chen et al., 2014) on neuronal activity in co-culture, epilepsy induced by 4 μM gabazine was compared to neuronal activity under 4 μM gabazine together with 50 μM perampanel.

Patch pipettes were fabricated from borosilicate capillaries (World Precision Instruments) and mounted on Luigs and Neumann-micromanipulators. Pipettes had resistances ranging from 3 to 7 MΩ when put in aCSF and filled with an internal solution containing (in mM): 130 K gluconate, 4 KCl, 5 Na-phosphocreatine, 10 HEPES, 0.1 EGTA, 4 Mg-ATP (pH set to 7.2).

An EPC10 amplifier (HEKA Elektronik, Lambrecht, Germany) controlled by Patchmaster software (HEKA) was used for acquisition of electrophysiological recordings. Currents were digitized at sampling rates of 25 kHz, filtered at 10 kHz, and Bessel-filtered at 2.9 kHz. The holding potential in the voltage clamp mode was set to -71 mV to correct for the liquid junction potential. Recordings were performed without series resistance compensation.

Electrophysiological data were analyzed using custom written macros in MATLAB and Igor Pro (Wavemetric Inc., Lage Oswego, OR, USA).

Electrophysiological validation of neuronal channelrhodopsin activation

To validate the ability of neuronal channelrhodopsin to reliably elicit action potentials, electrophysiological recordings of neurons in co-culture with astrocytes and GBCs were performed. For this purpose, neurons (DIV 7) were infected with 1 μl AAV particles (pAAV-CaMKIIa-mCherry (AAV2)) prior the addition of GBCs to the co-culture model. Infected neurons were subsequently targeted with whole-cell patch-clamp recordings. Neurons were stimulated with 473 nm laser light (Shanghai Laser & Optics Century Co. Ltd, China) via an optical fiber (Laser Components, Item 3016347) with blue light at a frequency of 10 Hz for 1 - 2 s. Currents produced by the opening of voltage-gated channels in the course of an action potential could be reliably elicited.

Perampanel treatment effects on GBC morphology over time

Perampanel treatment in two xenograft models was performed as described before (Venkataramani et al., 2019). Ten to 100 days prior to imaging, S24 Twitch3A cells or BG5 GFP cells were injected according to the method described above. In vivo MPLSM image z-stacks were acquired at 3 time points (0, 7, 14d). Identical tumor microregions, identified by vascular and other landmarks, were recorded at all 3 time points in every mouse. Imaging parameters for stacks were set to a pixel size of 0.59 μm and to a field of view with a volume of 607.28 μm x 607.28 μm x 240 μm with 81 slices at an interval of 3 μm. On day 0, food pellets of the mice in the treatment group were exchanged by pellets containing 320 mg per kg perampanel (Eisai) and offered ad libitum throughout the time lapse over fourteen days. In a dose escalation study for the GBC line BG5, we applied several amounts of perampanel ranging from 320 mg per kg to 960 mg per kg. Mice in the control group were offered their normal food ad libitum.

Validation of the invasivity score

For further validation of the invasivity score, we looked at the genes and gene sets that were enriched in the invasivity score. Here, we could clearly see that genes associated with physiological migration of neurons as well as genes associated with tumor cell motility could be found in the 20 genes with the highest invasivity score (Figure S4). Interestingly, the gene for the protein doublecortin (DCX) was among the high invasivity score genes. Doublecortin is a master regulator of physiological neuronal migration (Gleeson et al., 1999) but has also been already described to be involved in GB migration (Santra et al., 2009). Another example is the gene MARCKSL1 encoding for the MARCKS-like protein 1. MARCKS-like protein 1 is predominately expressed in the immature brain. Genetic disruption resulted in defects of cranial neural tube closure and neural tube defects where mechanisms such as neuronal migration are critical. Furthermore, MARCKS-like protein 1 has been also reported to play a role for cancer cell migration in breast cancer and lung adenocarcinoma (Liang et al., 2020; Salem et al., 2016). This further substantiates the concept of parallels between neuronal progenitor migration and tumor cell invasion. In addition, several genes associated with high invasivity have been shown to be involved in either brain tumor cell motility (e.g. BCAN; Zhang et al., 1998) or tumor cell motility across various entities (e.g. MALAT1 [Tano et al., 2010], ETV1 [Rahim et al., 2011], TNK2 [van der Horst et al., 2005]).

Further analysis revealed that the gene set for the invasion score is enriched for GO terms involving migration, motility and movement (Figure S4).

Lévy-like walk analysis of GB motility

In the past decades, Lévy walks have been used to analyze a wide range of mechanisms, e.g., in finance, biology, ecology or physics (Zaburdaev et al., 2015). For example, it has been controversely discussed if Lévy walks can be associated with an efficient search pattern in animal foraging (Sims et al., 2007; Zaburdaev et al., 2015). Recently, this movement pattern has been hypothesized to be a characteristic property of metastatic cancer cells (Huda et al., 2018). In the statistical analysis of stochastic processes, the differences between processes in discrete time and in continuous time should be carefully considered. While it can be useful to use a discrete index set to account for the finite number of sampling times and disregard the behavior in between these observations, there is no reason for most biological settings to assume that the actual process does not move continuously in time. This can lead to profound consequences. For example, it is sometimes attempted to determine the distribution of a process X by estimating the exponential parameter of the mean-squared displacement (MSD) $\langle X(t)\rangle \sim t^{\alpha}$ for $\alpha > 0$ and $t \to \infty$, which, even within the class of Gaussian processes, does not uniquely determine the process (Gneiting and Schlather, 2004; Zaburdaev et al., 2015). We accommodate the two model settings by introducing a time-continuous Lévy walk, which also allows the existence of second moments. In general, it should be noted that the sole analysis of the MSD as a metric to determine the distribution of a stochastic process is insufficient and has

significant weaknesses. While it can be used to decide if the process diffuses anomalously (i.e., slower of faster than a Brownian motion) and is a useful tool to analyze the scaling behavior of self-similar processes, the scaling parameter α in general does not determine the behavior of X on short time scales and for Lévy walks and for stable Lévy processes with stability index smaller than 2 the MSD is not even finite.

Moreover, the MSD relies on a sufficient number of data points at each time step. Specifically, due to the complexity ofdata collection, our dataset comprises a small number of tracks which persist through the whole time horizon. This is a possible explanation for the deteriorating fit of the log-log-linear regression for later stages in the experiment (see Figures S6D–S6K). Furthermore, it is sometimes criticized that, from a visual point of view, the log-log scale makes relationships seem more linear (Sims et al., 2007).

As an alternative, we consider the case of an anomalously diffusive Lévy process $(X_t)_{t \geq 0}$ with a stability parameter $\alpha > 0$ which moves through time with an acceleration factor $c > 0$. Then,

$$\mathbb{E}\left[(X_{ct} - X_0)^2\right] = (ct)^{\alpha}.$$

For equidistant observation times $t_0 = 0, t_1 = \Delta, ..., t_N = N\Delta$ with $N \in \mathbb{N}, \Delta > 0$, it then holds that

$$\frac{1}{n}\mathbb{E}\left[\sum_{i=1}^{n}\left(X_{t_i} - X_{t_{i-1}}\right)^2\right] = \Delta^{\alpha},$$

for $n = 1,...,N$. If the underlying process X is indeed a Lévy process, we get for independent trajectories $X^{(1)}, ..., X^{(M)}$ of X through the law of large numbers

$$\frac{1}{M}\sum_{k=1}^{M}\frac{1}{N}\sum_{i=1}^{N}\left(X_{t_i}^{(k)} - X_{t_{i-1}}^{(k)}\right)^2 \approx \Delta^{\alpha},$$

with a higher number of independent data points involved in the calculation. This quantity can be interpreted as an approximation of the mean-squared variation. By plugging in the MSD estimates for c and α, we can compare the two approaches. We see in see Figures S6D–S6K that the estimation is rather rough and the mean-squared variation does not converge, indicating that the assumption of independent, stationary increments might be violated.

Due to a lack of observable drivers of TM growth, we do not specify a stochastic process to model the expansion of TMs. In particular, there is no physiological justification to assume self-similarity. We observe that there is little to no movement in the TMs for a significant fraction of the observed sampling times of the process, interspersed with time frames of large growth. Since the empirical step size distribution is not atomless, a maximum-likelihood approach would yield flawed results. Instead, we rely on nonparametric methods from the field of extreme value theory to capture the behavior of the process and use estimators for the generalized extreme value index to demonstrate that the flight distribution between sampling times is indeed heavy-tailed. We depict the Hill plot generated by the Hill estimator (Bruce, 1975)

$$\widehat{\gamma}_{k,n}^{(H)} = \frac{1}{k}\sum_{i=0}^{k-1}\left(\log\left(X_{(n-i):n}\right) - \log\left(X_{(n-k):n}\right)\right), \quad k = 1, ..., n,$$

and the Dekkers-Einmal-de Haan plot generated by the corresponding estimator (Arnold and Laurens De, 1989)

$$\widehat{\gamma}_{k,n}^{(DEdH)} = \widehat{\gamma}_{k,n}^{(H)} + 1 - \frac{1}{2}\left(1 - \frac{\left(\widehat{\gamma}_{k,n}^{(H)}\right)^2}{\frac{1}{k}\sum_{i=0}^{k-1}\left(\log\left(X_{(n-i):n}\right) - \log\left(X_{(n-k):n}\right)\right)^2}\right)^{-1}, \quad k = 1, ..., n,$$

in see Figures S6D–S6K, where $X_1, ..., X_n$ are the step sizes and $X_{k:n}$ denotes the k-th order statistic. Though we are not able to determine a high-confidence estimate for the generalized extreme value index of the max-domain of attraction, it becomes clear that the step sizes follow a heavy-tailed distribution. Furthermore, the empirical autocorrelation function for the step sizes in Figure 4H seems to support the hypothesis of long-range dependence. We show the positive part of the empirical tail function (i.e., the excess tail function in 0) in see Figures S6D–S6K, which shows a polynomial decay.

Sensitivity analysis of Lévy-like walk analysis

As discussed above, we do not assume the structure of a specific stochastic process. Still, it is clear from our analysis that the analyzed TMs exhibit an anomalous diffusion behavior. Since the collection of *in vivo* data is complex, we rely on a limited number of TM observations, that is, between 50 and 100 tracks per setting. To analyze the effect of small sample sizes on the estimation, we simulate different stochastic processes with a diffusion behavior which is similar to the observed data. We use moment estimators to derive estimates of the stability parameter and the acceleration factor.

In the following, we first analyze several stochastic processes which diffuse anomalously with an (approximately) log-log-linear mean squared displacement. Afterwards, we simulate independent copies of these processes and analyze the behavior of the moment estimates, in particular in the setting of small sample sizes. While for certain processes consistency results for these estimators can be shown, we restrict ourselves to numerical experiments.

Fractional Compound Poisson Process

Let $(N(t), t \geq 0)$ be a fractional Poisson process with intensity $\lambda > 0$ and stability parameter $\nu \in (0, 1]$ as defined in Cahoy et al. (2010). Furthermore, let $(X_k)_{k \in \mathbb{N}_0}$ be a sequence of independent, identically distributed random variables with probability distribution $P_{X_1} = \frac{1}{2}\delta_{-1} + \frac{1}{2}\delta_1$, independent of N. Define the fractional compound Poisson process $(Z_t)_{t \geq 0}$ with drift $\mu > 0$ as $Z_t = \mu t^{\nu/2} + \sum_{i=0}^{N(t)} X_k$. It then holds that

$$\begin{aligned}
\mathbb{E}\left[Z_t^2\right] &= \sum_{n=0}^{\infty} \mathbb{E}\left[\left(\mu t^{\nu/2} + \sum_{k=1}^{n} X_k\right)^2 1_{N(t)=n}\right] \\
&= \mu t^{\nu} + \sum_{n=0}^{\infty} \mathbb{E}\left[\left(2\mu t^{\nu/2} \sum_{k=1}^{n} X_k + \sum_{j,k=1}^{n} X_k X_j\right) 1_{N(t)=n}\right] \\
&= \mu t^{\nu} + \sum_{n=0}^{\infty} P(N(t) = n) \cdot n \cdot \mathbb{E}\left[X_1^2\right] \\
&= \mu t^{\nu} + \mathbb{E}[N(t)] = \left(\frac{\lambda}{\Gamma(\nu+1)} + \mu\right) t^{\nu}.
\end{aligned}$$

Therefore, we get that

$$\log\left(\mathbb{E}\left[Z_t^2\right]\right) = \nu \log(t) + \log\left(\frac{\lambda}{\Gamma(\nu+1)} + \mu\right).$$

Fixing either $\lambda > 0$ or $\mu > 0$, we obtain a model for which moment estimators are derivable and for a fixed number of observations $t_0, \ldots, t_n$ we set

$$\widehat{\nu} = \frac{1}{n} \sum_{i=1}^{n} \frac{\log\left(\widehat{\mathbb{E}\left[Z_{t_i}^2\right]}\right) - \log\left(\widehat{\mathbb{E}\left[Z_{t_{i-1}}^2\right]}\right)}{\log(t_i) - \log(t_{i-1})}$$

and estimate the constant $c = \log(\lambda / \Gamma(\nu + 1) + \mu)$ through plug-in estimation. For fixed $\lambda > 0$, we then use the estimator $\widehat{\mu} = e^{\widehat{c}} - \lambda / \Gamma(\widehat{\nu} + 1)$.

Following Cahoy et al. (2010), we simulate the inter-arrival times of the fractional Poisson process N with rate $\lambda > 0$ by

$$T^d = \frac{|\log(U_1)|^{1/\nu}}{\lambda^{1/\nu}} \frac{\sin(\nu\pi U_2)(\sin((1-\nu)\pi U_2))^{1/\nu - 1}}{(\sin(\pi U_2))^{1/\nu} |\log(U_3)|^{1/\nu - 1}},$$

for independent $U_1, U_2, U_3 \sim \mathcal{U}[0, 1]$. We use this fact to simulate the paths of a fractional compound Poisson process.

Note that the log-log-linear MSD of a compound Poisson process follows as a special case with $\nu = 1$.

Fractional Brownian Motion

Let $B^H = (B_t^H)_{t \geq 0}$ be a fractional Brownian motion with Hurst parameter $H \in (0, 1)$. Then the MSD of the process $Z_t = \mu t^H + B_t$ for $t \geq 0$ is given by

$$\mathbb{E}\left[Z_t^2\right] = \mu^2 t^{2H} + 2\mu t^H \mathbb{E}[B_t] + \mathbb{E}\left[B_t^2\right] = \left(\mu^2 + 1\right) t^{2H}.$$

Therefore, the MSD of the process Z is again log-log-linear. We simulate trajectories of this process by generating a sample of a multivariate normal distribution with the appropriate covariance structure.

Other Gaussian processes

In general, the Karamata Representation Theorem (see, e.g., Theorem 1.5 in Geluk and Haan, 1987) yields that for any process with deterministic start point X_0 and second moments of the form

$$\mathbb{E}\left[Z_t^2\right] = c(t) \exp\left(\int_0^t \frac{a(s)}{s}\, \mathrm{d}s\right),$$

for all $t \geq 0$ and functions $c, a : (0, \infty) \to \mathbb{R}$ with existing limits $\lim_{t\to\infty} c(t) \in (0, \infty)$, $\lim_{t\to\infty} a(t) =: \alpha > 0$, the MSD is asymptotically monomial with exponent α, i.e., $\langle X(t) \rangle \sim t^{\alpha}$ for $t \to \infty$, the characteristic of anomalous diffusion (Metzler and Klafter, 2000). Hence, it is straightforward to construct superdiffusive processes for which the MSD on a limited time scale is not log-log-linear. Yet, the empirically observed process has the desired property on the observation interval and, using the models from Gneiting and Schlather (2004), we investigate the estimation stability for the α index in small sampling sizes if the long-term scaling limit differs from the short-term behavior.

Numerical Experiments

For the numerical analysis of the moment estimators for the MSD, we simulated 50 trajectories of the different stochastic processes and calculated the estimates for the intercept and slope in the log-log-linear relationship. This was repeated 1000 times and the mean and standard deviation of the respective values were calculated. The number of time steps 40 and the number of trajectories 50 were chosen to reflect the worst-case settings of the real-world experiment. We illustrate the results of the analysis in Figure 4H. In general, it can be observed that for the processes in consideration the average intercept and slope only mildly deviates from the true values. The empirical standard deviation, however, depends on the respective process, with a larger variance for the estimates for the fractional compound Poisson process.

QUANTIFICATION AND STATISTICAL ANALYSIS

The results of all quantifications were transferred to GraphPad Prism (GraphPad Software) or R to test the statistical significance with the appropriate tests (data were tested for normality using the D'Agostino & Pearson normality). Statistical significance was assessed by the two-sided Students' t-test for normally distributed data. Otherwise, a Mann–Whitney test was used for non-normal distributions. For more than 2 groups a one-way ANOVA test was used for normally distributed data and a Kruskal-Wallis test or the Friedman test (paired data) for non-normal distributed data. Results were considered statistically significant if the P value was below 0.05. Quantifications were done blinded by 2 independent investigators. Animal group sizes were as low as possible and empirically chosen and longitudinal measurements allowed a reduction of animal numbers by maintaining an adequate power. No statistical methods were used to predetermine sample size. Quantifications were depicted as dot plots with mean ± standard error of means or as violin plots.

Supplemental figures

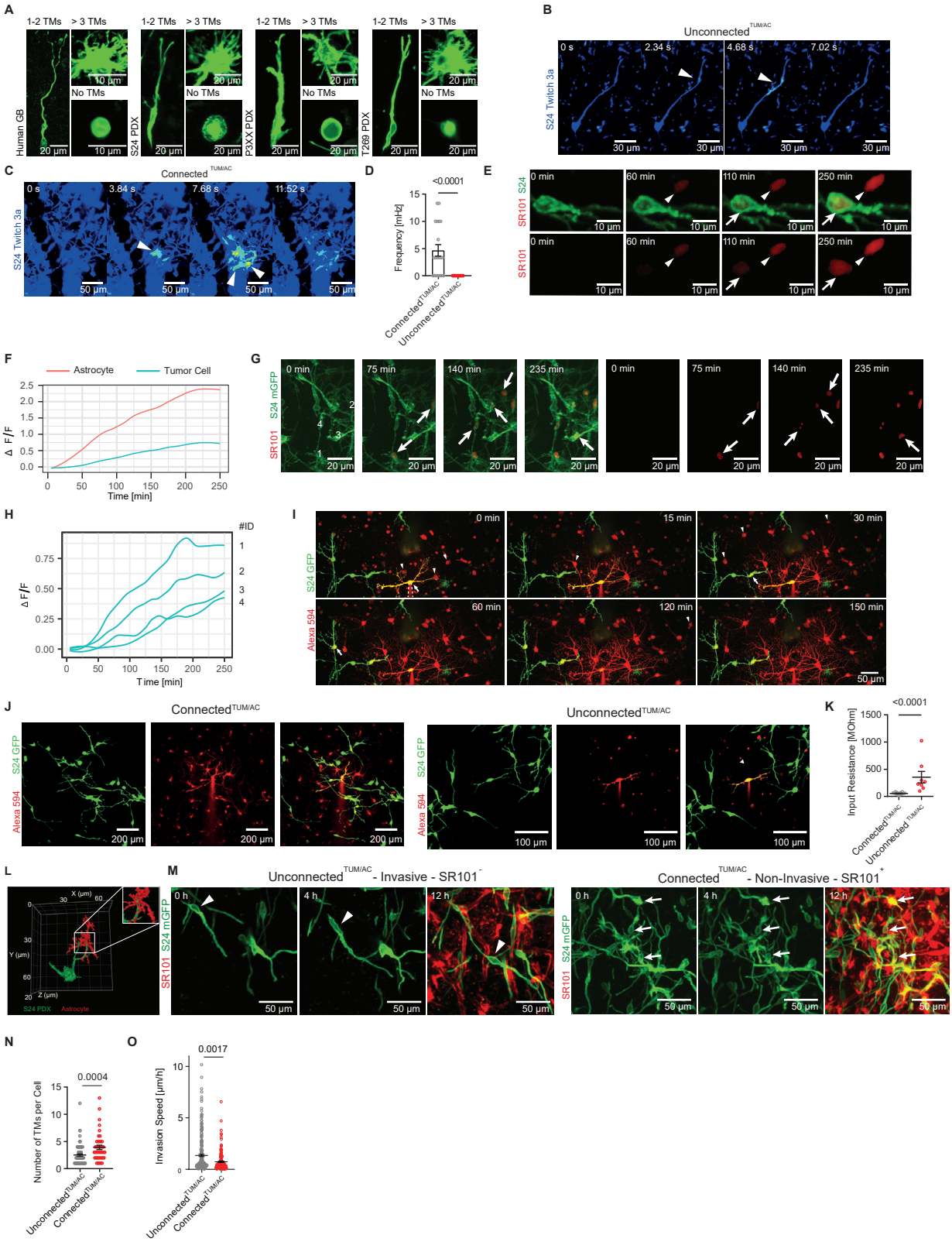

(legend on next page)

Figure S1. Functional differences between connected$^{TUM/AC}$ and unconnected$^{TUM/AC}$ brain tumor cells, related to Figure 1

(A) Representative images of morphologically different tumor cell subtypes with different number of TMs in resected human GB with anti-Nestin immunostaining (far left, *ex vivo* imaging with confocal microscopy) and in three different PDX models using *in vivo* two-photon microscopy expressing endogenous mGFP.

(B and C) Intracellular calcium events are seen in tumor-cell-unconnected GBCs whereas tumor-cell-connected GBCs (connectivity based on morphology) show multicellular calcium events.

(B) Arrowheads point to a subcellular calcium event in a TM.

(C) Arrowheads point to a multicellular calcium event in tumor-cell-connected GBCs.

(D) Quantification of the multicellular event frequency in connected$^{TUM/AC}$ GBCs and unconnected$^{TUM/AC}$ GBCs (n = 37 cells from 5 S24 PDX mice, Mann-Whitney test, connectivity based on morphology).

(E) Exemplary time-lapse IV2PM of SR101 uptake dynamic in S24 PDX GBC *in vivo* after intraperitoneal application at t = 0 min. Astrocyte shown in red (arrowhead), GBC shown in green (arrow). Raw images were post-processed with denoise.ai. Background of SR101 signal was subtracted.

(F) Mean SR101 intensity uptake in GBC (blue) and astrocytes (red) measured in single slices of a z stack over time (n = 17 GBCs and n = 18 astrocytes from 3 S24 PDX mice).

(G) IV2PM time-lapse of SR101 distribution in connected$^{TUM/AC}$ GBCs (connectivity based on SR101 uptake) showing how the dye is dynamically distributed between GBCs after intraperitoneal SR101 application at t = 0 min.

(H) Fluorescence intensity traces showing SR101 signal intensity at the regions of interest (ROIs) shown in (A) of four GBCs (left panel of G).

(I) Confocal *in vitro* co-culture time-lapse images of S24 connected$^{TUM/AC}$ GBCs with endogenous GFP fluorescence (green). One connected$^{TUM/AC}$ GBC is filled with Alexa 594 (red), and the dye gets distributed to surrounding astrocytes (red) and GBC (yellow) indicating connections to GBCs and astrocytes.

(J) Confocal *in vitro* co-culture images of the exemplary connected$^{TUM/AC}$ GBC of Figure 1F (top) and an exemplary unconnected $^{TUM/AC}$ GBC (bottom) with the left panel showing the endogenous GFP fluorescence of the S24 GBCs (green), the middle panel showing the astrocytes and GBCs filled with Alexa 594 (red) and right panel showing the composite images. The Alexa 594 dye remains mostly within the unconnected$^{TUM/AC}$ S24 GBC and gets distributed to the astrocytes in the connected$^{TUM/AC}$ GBCs.

(K) The electrophysiologically measured input resistance of connected$^{TUM/AC}$ GBCs in co-cultures is significantly lower than the input resistance of unconnected$^{TUM/AC}$ GBCs indicative of extensive gap junctional coupling of connected$^{TUM/AC}$ GBCs, connectivity was morphologically determined (n = 15 connected$^{TUM/AC}$ and 8 unconnected$^{TUM/AC}$ S24 GBCs, Mann-Whitney test). Data represented as mean ± SEM.

(L) An exemplary *ex vivo* 3D Rendering of a PDX model showing an anatomical connection between a GBC (green) and an astrocyte (red) (n = 4 connected$^{TUM/AC}$ GBCs in n = 3 S24 PDX mice) through a combined staining with antibodies against EAAT2/S100B.

(M) IV2PM time-lapse of an unconnected$^{TUM/AC}$, invasive cell that does not take up SR101 (above) and non-invasive tumor cell network taking up SR101 (below). Raw images were post-processed with enhance.ai.

(N) TMs per GBC acquired with IV2PM in connected$^{TUM/AC}$ and unconnected$^{TUM/AC}$ GBCs showing significantly more TMs in connected$^{TUM/AC}$ GBCs (n = 121 cells in 9 S24 PDX mice, Mann-Whitney test, connectivity based on SR101 uptake).

(O) GBC invasion speed compared for a timespan over 4 h for connected$^{TUM/AC}$ and unconnected$^{TUM/AC}$ GBCs (n = 394 cells from 9 S24 PDX mice, Mann-Whitney test, connectivity based on morphology).

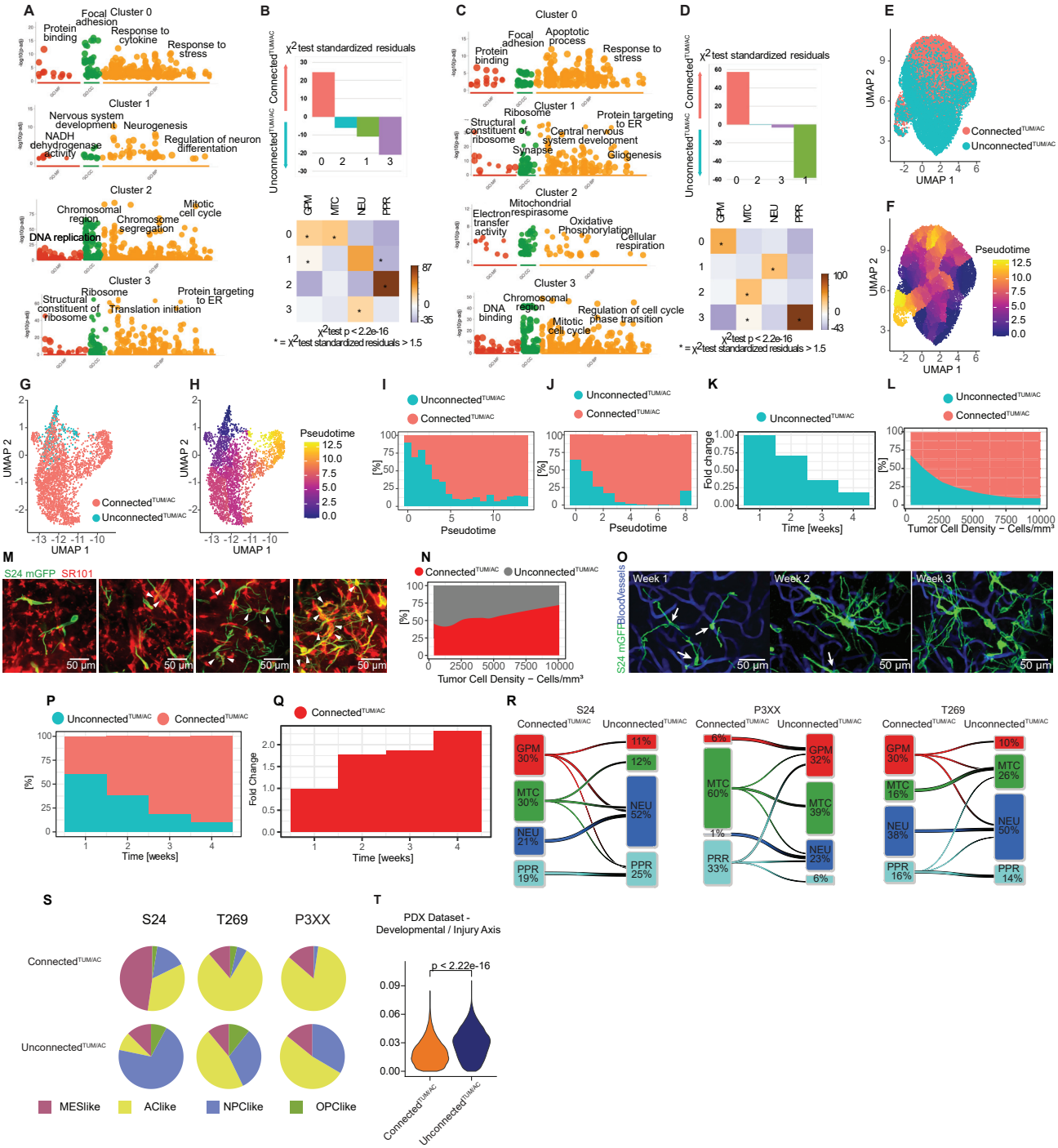

Figure S2. Single-cell RNA sequencing analyses of connected$^{TUM/AC}$ and unconnected$^{TUM/AC}$ brain tumor cells, related to Figure 2

(A–D) GO over-representation analysis (biological process: GO:BP; molecular function: GO:MF; cellular component: GO:CC) of differentially expressed genes of S24 (left) and T269 (right) PDX(min.pct = 0.25, logfc.threshold = 0.25) in each cluster using gProfiler (FDR < 0.01). Representative pathways are reported.

(B–D) Enrichment of connected$^{TUM/AC}$ and unconnected$^{TUM/AC}$ cells in each cluster seen in (A) and (C). Reported are the standardized residuals from the chi-squared test. Enrichment of the four functional subtypes in each cluster is shown. Reported are the standardized residuals from the chi-squared test. * = standardized residuals > 1.5. S24 PDX (B), T269 PDX (D).

(E) Uniform manifold approximation projection (UMAP) plot of the T269 PDX model in which GBCs are colored based on their connectivity$^{TUM/AC}$ (n = 17,178 cells, connectivity based on SR101 uptake.).

(F) UMAP plot of the T269 PDX model in which GBCs are colored based on their pseudotime (n = 17,178 cells, connectivity based on SR101 uptake.).

(G) UMAP plot of the P3XX PDX model, cells are colored based on their connectivity $^{TUM/AC}$ (n = 3,015 cells, connectivity based on SR101 uptake.).

(legend continued on next page)

(H) UMAP plot of the P3XX PDX model, cells are colored based on their pseudotime (n = 3,015 cells, connectivity based on SR101 uptake.).
(I) Distribution of connected$^{TUM/AC}$ and unconnected $^{TUM/AC}$ T269 GBCs plotted based on their pseudotime (n = 17,178 cells, connectivity based on SR101 uptake.).
(J) Distribution of connected$^{TUM/AC}$ and unconnected$^{TUM/AC}$ P3XX GBCs plotted based on their pseudotime (n = 3,015 cells, connectivity based on SR101 uptake.).
(K) Panel shows the fold change of unconnected$^{TUM/AC}$ cells, determined by normalization of the percentage over 4 weeks to the value determined in the first week, connectivity based on SR101 uptake (n = 1,592 cells in 16 datasets of 4 S24 PDX mice, connectivity based on morphology).
(L) Distribution of unconnected$^{TUM/AC}$ and connected$^{TUM/AC}$ S24 GBCs plotted based on their tumor cell density, connectivity based on morphology (n = 4,425 cells in 47 datasets in 18 S24 PDX mice). Data points are plotted with a smoothing function.
(M) IV2PM images with different tumor cell density of connected$^{TUM/AC}$ (arrowhead) and unconnected$^{TUM/AC}$ S24 GBCs. Connected $^{TUM/AC}$ GBCs take up SR101 (red). Raw images were post-processed with enhance.ai.
(N) Distribution of unconnected$^{TUM/AC}$ and connected$^{TUM/AC}$ S24 GBCs plotted based on their tumor cell density (n = 4,425 cells in 47 datasets in 18 S24 PDX mice). Data points are plotted with a smoothing function (stat_smooth() in R with a span of 0.55).
(O) Intravital imaging of identical tumor microregions at days 0, 9, 15, and 22 of S24 PDX mice (MIP [z = 30 μm]). GBCs are colored in green while blood vessels are colored in blue. Unconnected$^{TUM/AC}$ cells are marked with arrows, connectivity based on morphology. Representative series out of 5 such series taken in 5 S24 PDX mice. Raw images were restored in enhance.ai and the vessel channel was post-processed with the "remove outliers" function in ImageJ/Fiji.
(P) Average distribution of connected$^{TUM/AC}$ and unconnected$^{TUM/AC}$ cells (n = 3,502 cells) in the same region at 2–6 time points in 5 S24 PDX mice, connectivity based on morphology.
(Q) Bar plot of the fold change of connected$^{TUM/AC}$ S24 GBCs in tumor regions followed up over 4 weeks (n = 3,169 cells in 24 datasets of 6 S24 PDX mice). Datasets are normalized by division of the value at the first time point.
(R) River plots of three PDX models (S24, T269, and P3XX) of each cell line for the pathway-based classification (glycolytic/plurimetabolic [GPM, red], mitochondrial [MTC, green], neuronal [NEU, dark blue], and proliferative/progenitor [PPR, light blue]) for connected$^{TUM/AC}$ and unconnected$^{TUM/AC}$ GBCs.
(S) Distribution of gene-based cell states for S24 (n = 15,629 cells), T269 (n = 17,178 cells), and P3XX (n = 3,015 cells), connectivity based on SR101 uptake.
(T) Gene expression score along the developmental/injury axis in three PDX datasets, connectivity based on SR101 uptake (n = 35,822 cells).
(S and T) Enrichment of connected$^{TUM/AC}$ and unconnected$^{TUM/AC}$ cells in each cluster. Reported are the standardized residuals from the chi-squared test. Enrichment of the four functional subtypes in each cluster. Reported are the standardized residuals from the chi-squared test. * = standardized residuals > 1.5. S24 PDX (S), T269 PDX (T).

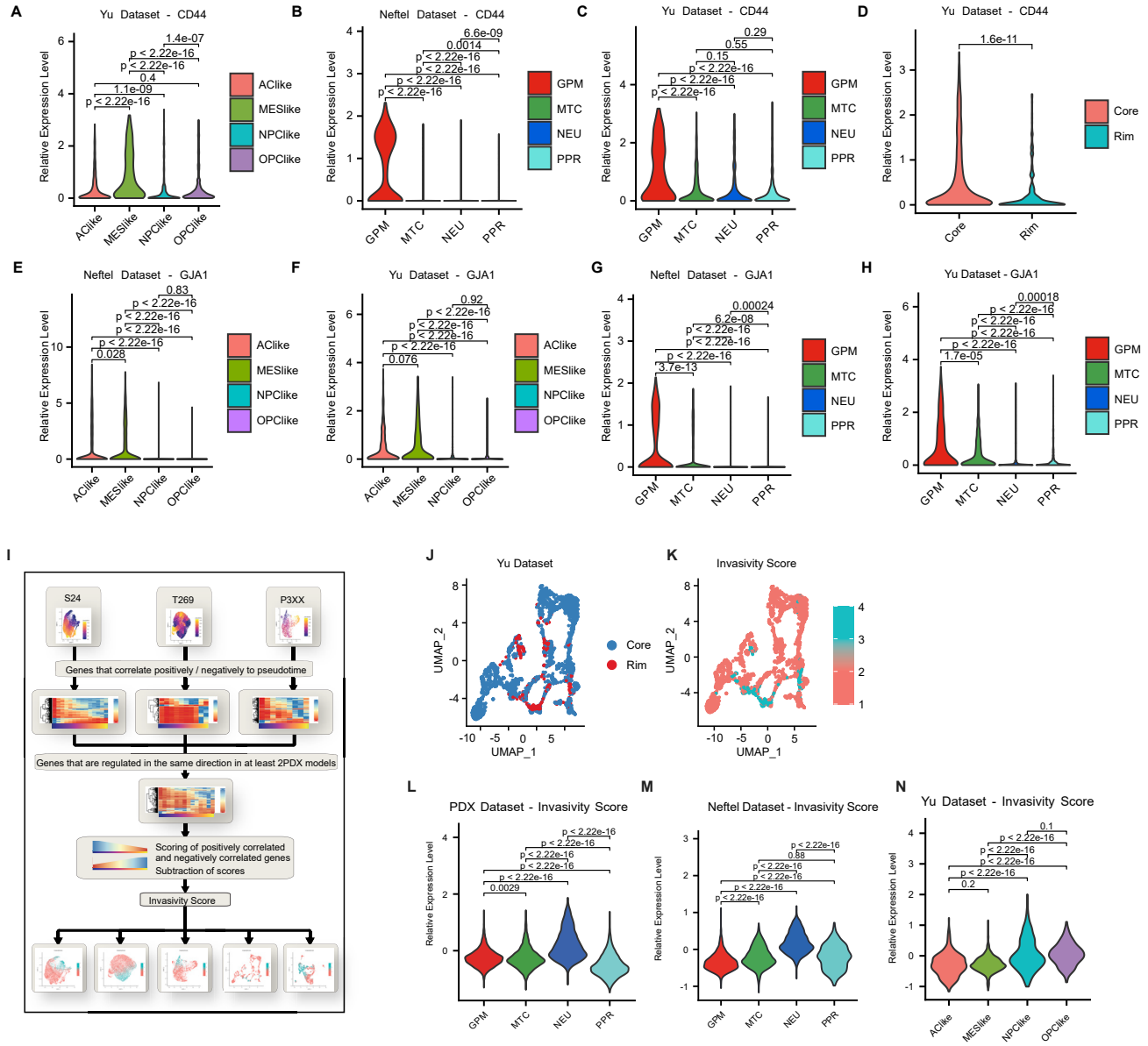

Figure S3. Single-cell RNA sequencing analyses of glioblastoma cell states and relation to the invasivity score, related to Figure 2

(A) Violin plot displaying CD44 gene expression of GBCs in the Yu dataset split by gene-based cell state assignment (n = 2,795 cells).

(B) Violin plot displaying CD44 gene expression of GBCs in the Neftel dataset split by gene-based cell state assignment (n = 6,576 cells).

(C) Violin plot displaying CD44 gene expression of GBCs in the Yu dataset split by the pathway-based cell state assignment (n = 2,795 cells).

(D) Violin plot displaying CD44 gene expression of GBCs in the Yu dataset split by sample localization of rim and core regions (n = 2,795 cells).

(E) Violin plot displaying GJA1 gene expression of GBCs in the Neftel dataset split by gene-based cell state assignment (n = 6,576 cells).

(F) Violin plot displaying GJA1 gene expression of GBCs in the Yu dataset split by gene-based cell state assignment (n = 2,795 cells).

(G) Violin plot displaying GJA1 gene expression of GBCs in the Neftel dataset split by pathway-based cell state assignment (n = 6,576 cells).

(H) Violin plot displaying GJA1 gene expression of GBCs in the Yu dataset split by pathway-based cell state assignment (n = 2,795 cells).

(I) Schematic of the analysis workflow with which the invasivity score for GBCs was determined.

(J and K) UMAP plot of GBCs in the Yu dataset. GBCs are colored based on their localization in the core and rim of the tumor (J). A UMAP plot of GBCs of the Yu dataset is shown in which cells are colored based on their invasivity score (K) (n = 2,795 cells).

(L) Violin plot of GBCs in the PDX dataset displaying the invasivity score expression split by the gene-based cell state assignment (n = 35,822 cells).

(M) Violin plot of GBCs in the Neftel dataset displaying the invasivity score expression split by the pathway-based cell state assignment (n = 35,822 cells).

(N) Violin plot in the Yu dataset displaying the invasivity score expression split by the gene-based cell state assignment (n = 6,576 cells).

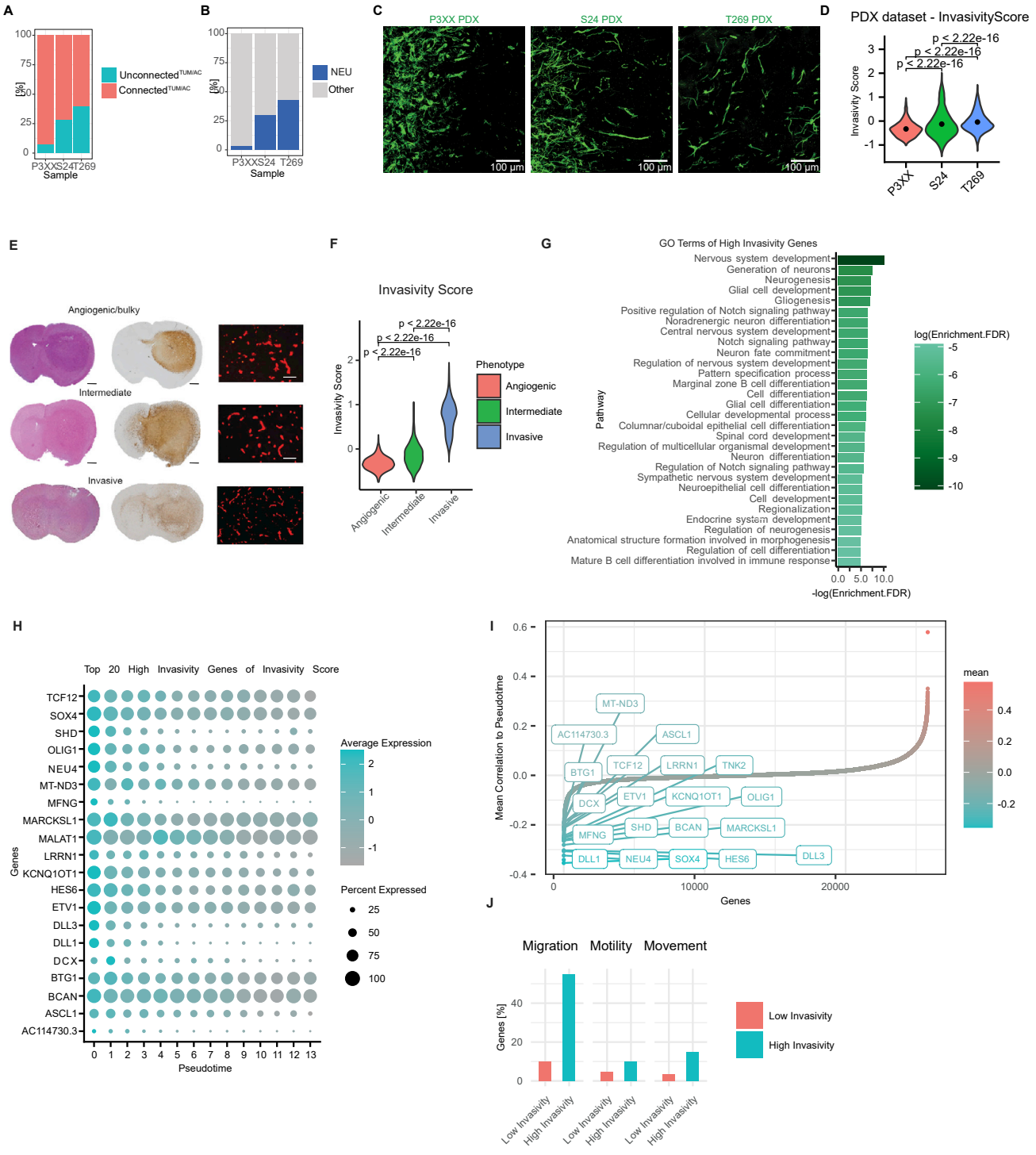

Figure S4. Characterization of the invasivity score, related to Figure 2

(A) Percentage of connected$^{TUM/AC}$ and unconnected$^{TUM/AC}$ in P3XX, S24, and T269. Connected$^{TUM/AC}$ GBCs were based on their SR101 uptake (n = 3,015, n = 15,629, and n = 17,178 cells, respectively).

(B) Percentage of NEU cells in S24 and T269 (n = 3,015, n = 15,629, and n = 17,178 cells, respectively), based on the pathway-based classification.

(C) Representative *ex vivo* confocal imaging of the three different PDX cell lines expressing mGFP (maximum intensity projection of z = 46 μm). Raw images were post-processed with denoise.ai and the "remove outliers" function in Fiji/ImageJ.

(D) Invasivity score based on different phenotypes of PDXs models (n = 35,822 cells from 3 PDX models [P3xx, S24, T269]).

(legend continued on next page)

(E) Histopathological characteristics of PDOX models. Hematoxylin and eosin, human-specific stainings with antibodies against vimentin and mouse-specific CD31 stainings are shown for PDXs representative for three histopathological types on the left side: angiogenic (P13), intermediate (T16), and invasive (T347). Scale bars represent 1 mm (black) and 100 μm (white).
(F) Invasivity score based on different phenotypes of PDOXs models, exemplary stainings are shown in (E) (n = 8,837 cells from 9 PDOX models [P13, P3, P8, T101, T16, T192, T233, T347, T470]).
(G) Top GO terms of high invasivity genes (n = 30 GO terms). Enriched GO terms were determined using ShinyGO.
(H) Dot plot showing the expression of top 20 high invasivity genes along pseudotime in the PDX dataset (n = 35,822).
(I) Correlation of genes to pseudotime, top 20 anticorrelating genes are shown (PDX dataset n = 35,822 cells).
(J) Percentage of GeneCards descriptions of high and low invasivity genes that contain the terms "migration," "motility," or "movement" in the GeneCards "summaries"-table (n = 172 genes).

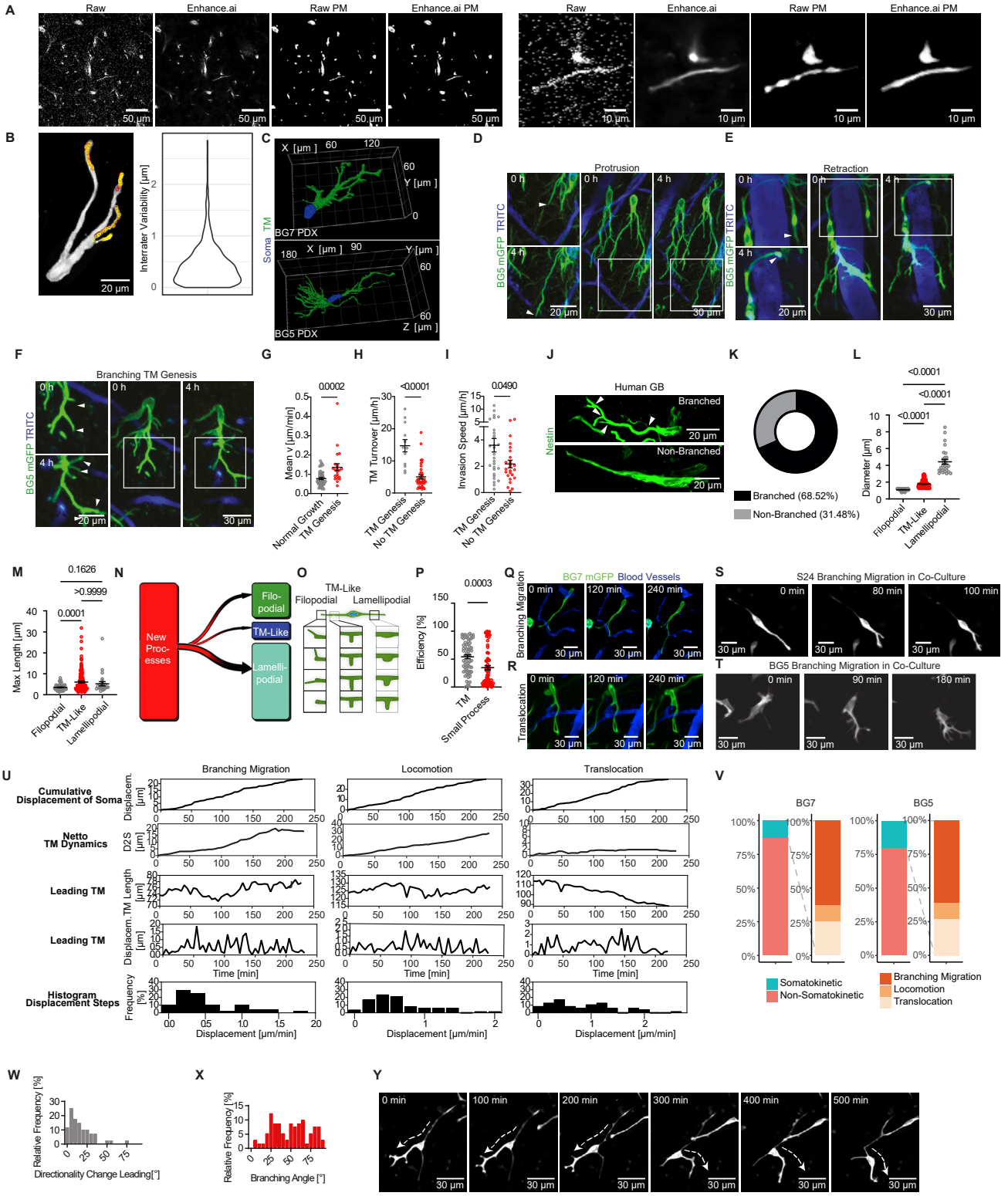

(legend on next page)

Figure S5. Mechanistic characterization of subcellular components driving GBC invasion, related to Figures 3 and 4

(A) Comparison of raw IV2PM images to restored images with enhance.ai and subsequent processing with a pixel classification workflow in ilastik.

(B) TM tracks (left side) that were manually tracked by two independent investigators projected onto an exemplary IV2PM image exemplifying the interrater variability and robustness of the TM tracking workflow (see STAR Methods). Quantification of interrater variability for manual TM tracking of intravitally imaged GBCs on the right side.

(C) 3D rendering of segmented GBCs from two PDX models (BG7, BG5) imaged with IV2PM. TMs are shown in green while the GBC somata are shown in blue.

(D–F) Protrusion, retraction and branching examples of TMs in the BG5 PDX model captured with IV2PM. Blood vessels are shown in blue while the GBCs are green. Arrow heads indicate dynamic blind-ending TMs. Raw images were post-processed with enhance.ai, and background was removed with the "remove outlier" function in ImageJ/Fiji.

(G) Mean TM growth speed of TMs with normal growth compared with the subgroup of TMs with TM genesis (n = 72 TMs from 31 somatokinetic GBCs from 4 S24 PDX mice, Mann-Whitney test).

(H) TM turnover of GBCs with TM genesis as compared with GBCs without TM genesis (n = 51 cells from 4 S24 PDX mice, Mann-Whitney test).

(I) Invasion speed of GBCs with TM genesis compared with GBCs without TM genesis (n = 55 cells from 4 S24 PDX mice, Mann-Whitney test).

(J) Representative confocal microscopy of branching (above) and non-branching (below) GBC in resected patient material. Arrowheads point to the branching points.

(K) Relative abundance of branching versus non-branching GBC (n = 54 uni- or bipolar cells from 6 patients). Data in (G) and (K)–(M) are represented as mean ± SEM.

(L and M) Diameter (L) and maximum length (M) comparison between the three different small process classes (n = 291 processes from 8 S24 PDX mice, Kruskal-Wallis test).

(N) Transition plot of newly developing GBC processes (n = 210 processes from 8 S24 PDX mice).

(O) Scheme showing different classes of small process GBC dynamics.

(P) Quantification of TM growth efficiency (netto growth divided by overall traveled track distance) between TMs and small processes (n = 138 TMs from 8 S24 PDX mice, Mann-Whitney test).

(Q and R) IV2PM example of invasion phenotypes in BG7 GBCs (green) over 4 h. Blood vessels are colored in blue. Raw images were post-processed with enhance.ai, and background signal was removed with the "remove outliers" plugin in ImageJ/Fiji.

(S and T) Branching migration examples in two GBC lines (S24 in S and BG5 in T) in co-cultures with astrocytes and neurons. Raw images were post-processed with denoise.ai.

(U) Quantitative comparison of different invasive mechanisms *in vivo* of cumulative displacement of somata, netto TM dynamics, TM length of the leading TM and displacement of the TM length and the histogram of the displacement steps of exemplary S24 GBCs.

(V) Percentages of somatokinetic GBCs and distribution of invasion phenotypes for the BG7 and BG5 PDX model (BG7: n = 108 non-somatokinetic cells and 25 somatokinetic GBCs in 2 mice. BG5: n = 60 non-somatokinetic cells and n = 8 somatokinetic GBCs in 2 mice). Data in (C) are represented as mean ± SEM.

(W and X) Histogram of the angle of directionality change in the leading TM (W) as compared with the histogram of the branching angles (X) (n = 66 TMs [M] and n = 85 TMs [N]).

(Y) *In vitro* live cell time-lapse imaging of a S24 branching migrating GBC with a directionality change mediated by branching. The timespan shown here covers 500 min. Raw images were post-processed with denoise.ai.

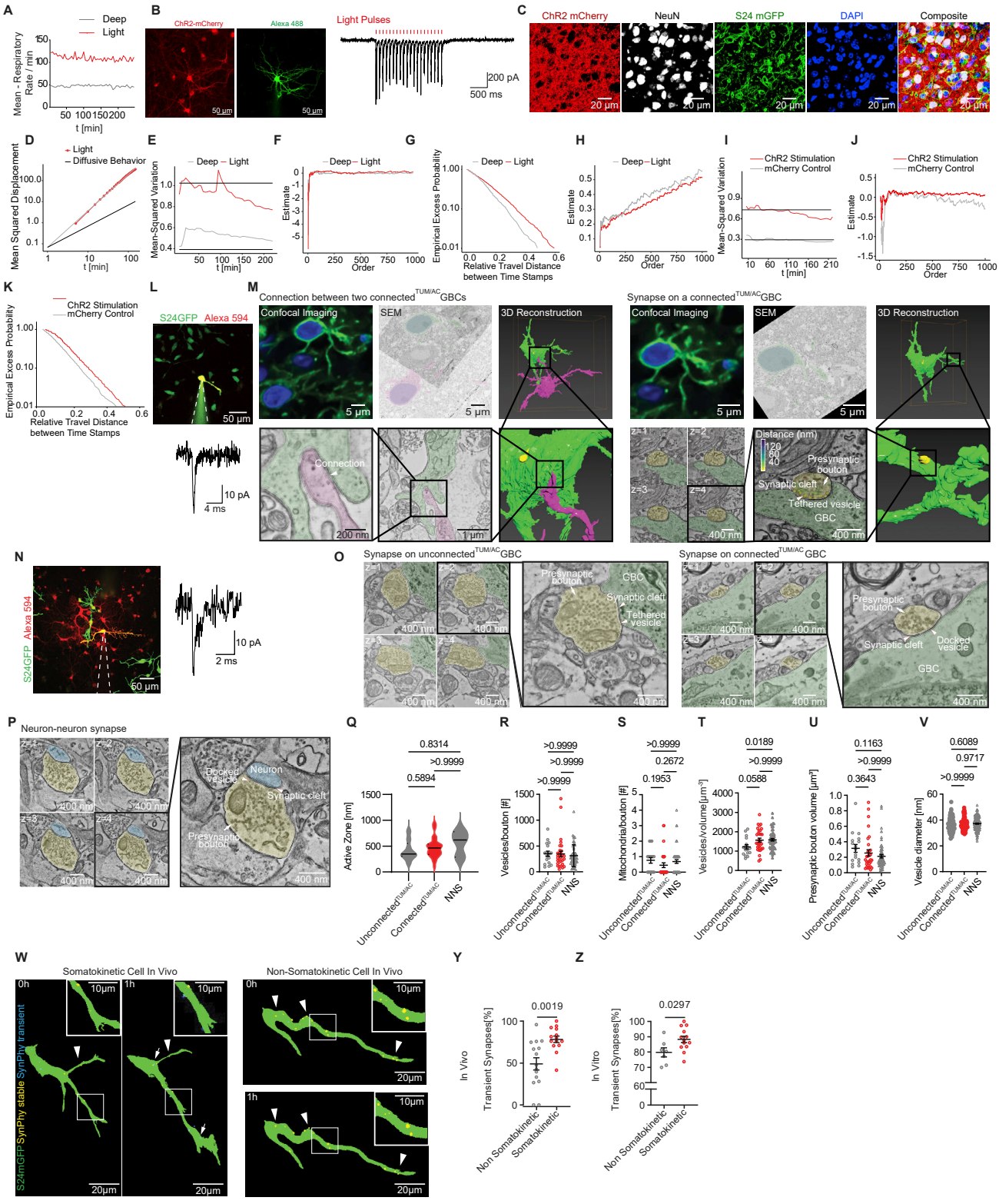

(legend on next page)

Figure S6. Neuronal activity-driven TM dynamics and neurogliomal synaptic input, related to Figure 5

(A) Exemplary monitoring of deep and light anesthesia with isoflurane based on the breathing rate (n = 49 time points in 10 PDX mice).

(B) Validation of the channelrhodopsin construct (mChR2-H134) in AAV-infected neurons in co-cultures with astrocytes and GBCs stimulated with blue light followed by currents produced by the opening of voltage-gated channels in the course of an action potential after optogenetic stimulation. Upper panels: images of neurons in co-cultures with astrocytes and GBCs infected with AAV-mCherry-ChR2-H134 virus. On the left side infected neurons expressing mCherry can be seen. On the right side, a patched neuron filled via the patch pipette with Alexa 488 can be seen. Lower panel: the red bars indicate light pulses and the trace below shows the current trace of the neuron that was patched in voltage-clamp mode reliably showing currents produced by the opening of voltage-gated channels in the course of an action potential after optogenetic stimulation with 10 Hz.

(C) Expression of CaMKIIahChR2(H134R)-mCherry (AAV2) in the infiltration zone. Confocal maximum intensity projection (z = 10 μm) of a representative S24 PDX mouse brain slice infected with CaMKIIahChR2(H134R)-mCherry (AAV2) (red). The tumor cells express mGFP (green), neurons were stained with NeuN (white), and all nuclei were stained with DAPI (blue) (n = 3 S24 PDX mice).

(D) Mean-squared displacement of TM movement steps under light and deep anesthesia conditions. Red line: mean-squared displacement of GBC TM tracks in the light isoflurane paradigm, indicating a superdiffusive behavior. Gray line: best-fit linear regression. Black: mean-squared displacement of a diffusive process.

(E) Mean-squared variation plot for the control and light isoflurane paradigm. The black lines indicate the expected behavior under independent and stationary increments.

(F) Dekkers-Einmal-de Haan plot of TM movement steps under deep and light anesthesia conditions.

(G) Tail functions of positive travel distance under light and deep anesthesia conditions.

(H) Hill plot of TM movement steps under deep and light anesthesia conditions in S24 PDX mice.

(I) Mean-squared variation plot for the mCherry control and the ChR2 stimulation paradigm. The black lines indicate the expected behavior under independent and stationary increments.

(J) Dekkers-Einmal-de Haan plot of TM movement steps under neuronal channelrhodopsin-mCherry-stimulated and control conditions.

(K) Tail functions of positive travel distance of TM movement steps under neuronal channelrhodopsin-mCherry-stimulated and control conditions.

(L) Confocal image of neuronal/astrocytic co-culture with S24 GBCs (green). A pipette filled with Alexa 594 (red) is used for patch-clamp of GBC. The unconnected$^{TUM/AC}$ GBC is filled with Alexa 594 (red) while other GBCs stay green, and no astrocytes are filled with the red dye.

(M) The left panel shows correlative light and electron microscopy (CLEM) of two connected$^{TUM/AC}$ GBCs (mGFP-positive GBCs shown in green and nuclei stained with DAPI in blue) with 3D-reconstruction of the connection and scanning electron microscopy image of the connection. One GBC is colored in green, the other one in magenta. The right panel shows CLEM imaging of a connected$^{TUM/AC}$ GBC with a 3D reconstruction of the cell using manual segmentation of 153 2D-EM-sections. The lower part of the right panel shows series of 2D-sections of a synaptic contact on the connected$^{TUM/AC}$ GBC with zoom-in and 3D-EM-reconstruction. 3D reconstructions were performed in TrakEM2 and visualized in Autodesk 3ds max.

(N) Confocal image of neuronal/astrocytic co-culture with S24 GBCs (green). A pipette filled with Alexa 594 (red) is used for patch-clamp of GBC. The connected$^{TUM/AC}$ GBC is connected to other tumor cells and astrocytes, which are filled with the gap-junction-permeable Alexa 594.

(O) Scanning electron microscopy image of a synaptic contact on an unconnected$^{TUM/AC}$ GBC, connectivity based on morphology. GBC is shown in green, neuronal presynaptic bouton in yellow (left side). Scanning electron microscopy image of a synaptic contact on a connected$^{TUM/AC}$ GBC, connectivity based on morphology (right side).

(P) Scanning electron microscopy image of a healthy neuron-neuron-synapse, presynaptic part colored in yellow, post-synaptic part in blue.

(Q–V) Quantification of morphometric parameters of synapses on unconnected$^{TUM/AC}$ versus connected$^{TUM/AC}$ GBCs versus neuron-neuron synapses (NNSs). Unconnected$^{TUM/AC}$ and connected$^{TUM/AC}$ GBCs were identified via correlative light and electron microscopy. Unconnected$^{TUM/AC}$ GBCs do not have connections to other tumor cells. Connected$^{TUM/AC}$ GBCs exhibit at least one connection to other GBCs. (n = 17 synapses on 5 unconnected$^{TUM/AC}$ GBCs from 3 S24 PDX mice; n =31 synapses on 8 connected$^{TUM/AC}$ GBCs from 3 S24 PDX mice, connectivity based on morphology; n = 55 neuron-neuron synapses from 4 PDX S24 mice; Kruskal-Wallis test).

(W) A somatokinetic and a non-somatokinetic S24 PDX GBC *in vivo* are shown together with putative neurogliomal presynaptic bouton. Putative neurogliomal presynaptic boutons are shown in blue (arrows) that are transient over time. Stable synaptic boutons are shown in yellow (arrowheads).

(Y) Percentage of transient putative neurogliomal presynaptic boutons (see STAR Methods) compared between somatokinetic and non-somatokinetic PDX GBCs (n = 14 somatokinetic GBCs and n = 15 non-somatokinetic GBCs and of 3 PDX mice, Mann-Whitney test).

(Z) Percentage of transient putative neurogliomal presynaptic boutons compared between somatokinetic and non-somatokinetic S24 GBCs in co-culture with neurons and astrocytes (n = 13 somatokinetic GBCs and n = 7 non-somatokinetic GBCs, unpaired t test).

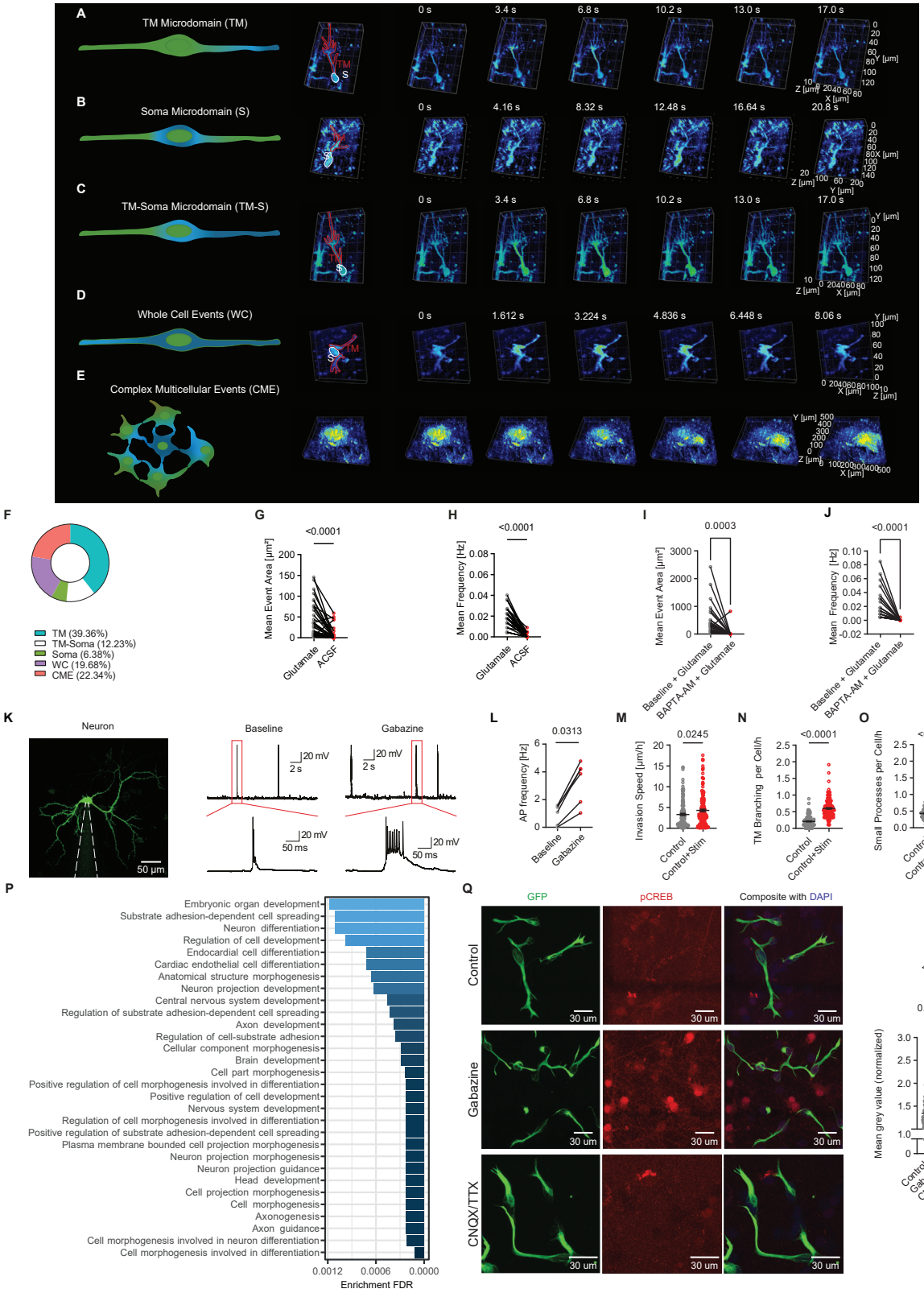

(legend on next page)

Figure S7. Classification of calcium events in GBC *in vivo* with 3D calcium imaging, related to Figure 6

(A) Example of a calcium event restricted to a TM as seen with *in vivo* 3D calcium imaging.
(B) Example of a calcium event restricted to a GBC soma as seen with *in vivo* 3D calcium imaging.
(C) Example of a calcium event restricted to TM and GBC soma as seen with *in vivo* 3D calcium imaging.
(D) Example of a calcium event encompassing the whole cell as seen with *in vivo* 3D calcium imaging.
(E) Example of a calcium event in the GBC network termed multicellular events (CME) as seen with *in vivo* 3D calcium imaging.
(F) Distribution of classes of calcium events in GBCs *in vivo* shown in Figure S6 with 3D calcium imaging (n = 272 GBCs from 4 S24 PDX mice).
(G) Mean event area of calcium transients in BG5 GBCs *in vitro* during glutamate puffing and aCSF puffing (n = 45 pairs, two-tailed Wilcoxon test).
(H) Mean frequency of calcium transients in BG5 GBCs *in vitro* during glutamate puffing and aCSF puffing (n = 45 pairs, two-tailed Wilcoxon test).
(I and J) Mean event area and mean event frequency in S24 GBCs, baseline glutamate puffing compared with BAPTA-AM wash-in (n = 27 cells).
(K) Confocal image of a neuron in co-culture filled with Alexa 488. Patch pipette is indicated by dashed lines (left). Representative recordings of neurons in co-culture before and after 4 μM gabazine wash-in (right).
(L) Quantification of AP frequency before and after wash-in of gabazine (two-sided Wilcoxon matched-pairs test, n = 6 cells).
(M–O) Invasion speed (M), TM branching events (N), and small process dynamics (O) per GBC per hour under gabazine treated conditions compared with control conditions with DMSO (n = 147 control and n = 163 gabazine treated conditions in n = 4 independent experiments, Mann-Whitney test).
(P) Enriched GO terms for the genes that are regulated by the CREB1 regulon. pySCENIC analyses are based on the Yu dataset (n = 30). Terms are sorted and colored by enrichment.
(Q) Confocal images of neuronal and astrocytic co-cultures with S24 GBCs (green) stained against phosphorylated CREB (pCREB) under control conditions, neuronal stimulation with gabazine and incubation with CNQX and TTX (left). Quantification of normalized mean gray value under different conditions (right) (n = 159 GBCs under control, n = 199 GBCs under gabazine, and n = 157 GBCs under CNQX/TTX condition, Kruskal-Wallis test).
Data in (L)–(N) and (Q) are represented as mean ± SEM.

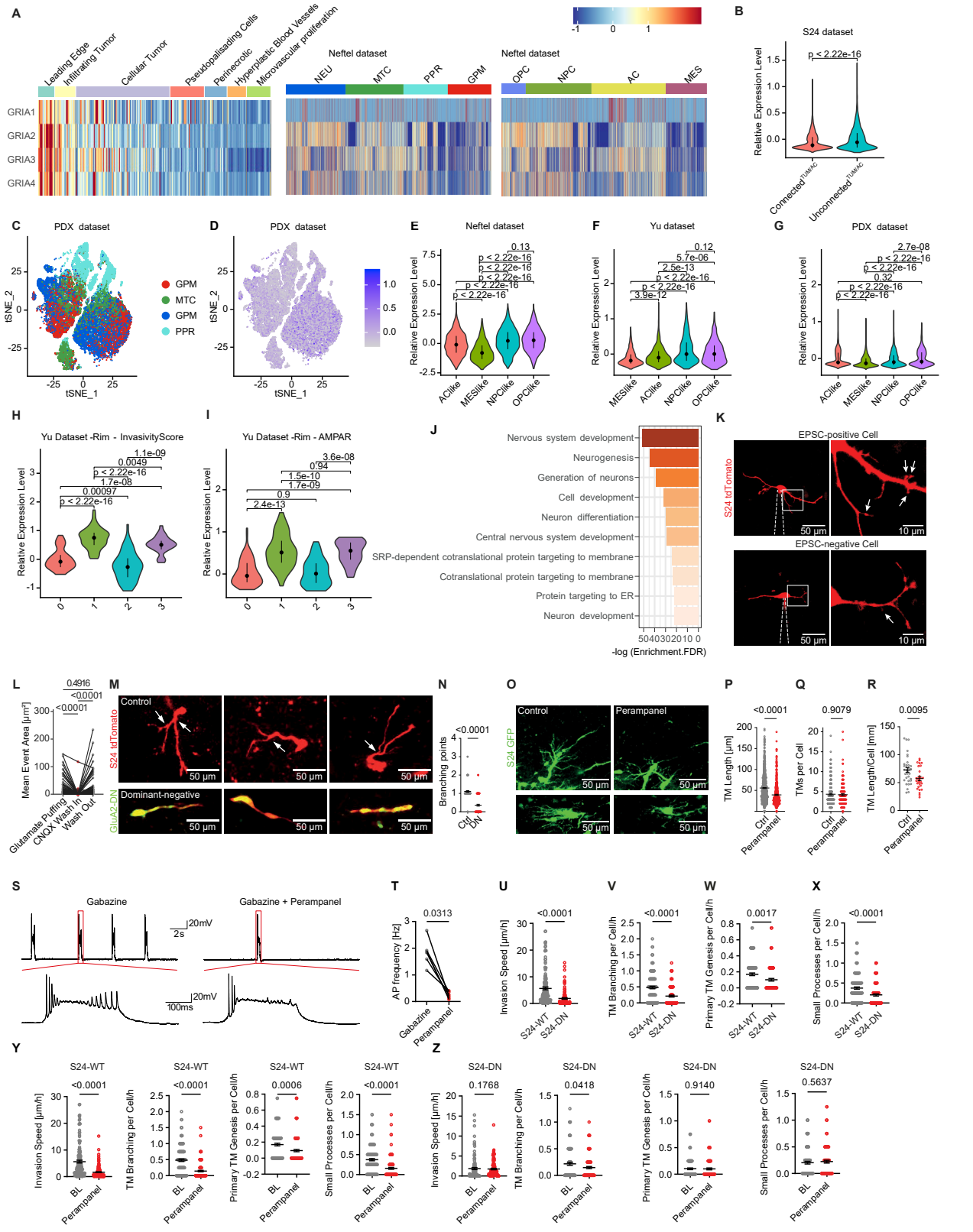

(legend on next page)

Figure S8. AMPA receptors inhibition *in vivo* and in co-cultures reduces TM generation and TM growth, related to Figure 7

(A) Heatmap displaying gene expression of AMPAR genes in Ivy Glioblastoma dataset (n = 270 samples) (left panel). Heatmap displaying gene expression of AMPAR genes in Neftel dataset, grouped based on the pathway-based classification (n = 6,576 cells) (middle panel). Heatmap displaying gene expression of AMPAR genes in Neftel dataset, grouped based on gene-expression-based classification (n = 6,576 cells) (right panel).

(B) AMPAR gene expression score in connected$^{TUM/AC}$ and unconnected$^{TUM/AC}$ GBCs of the S24 PDX dataset (n = 15,629 cells).

(C) tSNE plot of all PDX cells. Cells are colored based on the pathway-based cell state classification (n = 35,822 cells).

(D) Expression of AMPAR gene expression scores on a tSNE plot of PDX cells (n = 35,822 cells).

(E) Violin plot displaying the AMPAR gene expression score in the Neftel dataset sorted by the gene-based cell states (n = 6,576 cells).

(F) Violin plot displaying the AMPAR gene expression score in the Yu dataset sorted by the gene-based cell states (n = 2,795 cells).

(G) Violin plot displaying AMPAR gene expression scores in the PDX dataset sorted by the gene-based cell states (n = 35,822 cells).

(H) Invasivity signature score in clusters of rim cells in the Yu dataset (n = 239 cells).

(I) Expression of AMPAR score signature in clusters of rim cells of Yu dataset (n = 239 cells).

(J) Enriched GO terms of marker genes of rim cluster 1 (n = 10), (as seen in J and K).

In all panels, connectivity is based on SR101 uptake.

(K) Exemplary images of S24 GBCs in co-cultures with astrocytes and neurons of EPSC-positive (top) and EPSC-negative cells (bottom). Arrows show branching points. Dotted line indicates the patch pipette.

(L) Mean event area of BG5 GBCs under glutamate puffing, CNQX wash-in and wash-out (n = 70 cells, Friedman test).

(M) Exemplary IV2PM images of control S24 GBCs and dominant-negative AMPAR construct expression. Arrows show branching points in S24 control GBCs only expressing tdTomato without the dominant-negative AMPAR construct.

(N) Quantification of branching points per GBC of control S24 GBCs and dominant-negative AMPAR construct expressing cells *in vivo* (n = 211 from 4 S24 PDX mice, Mann-Whitney test).

(O) Representative images of BG5 GBC under control conditions and treatment with perampanel *in vivo*.

(P–R) (P) TM length (n = 1,426 TMs from 6 BG5 PDX mice, Mann-Whitney test), (Q) TMs per cell (n = 429 TMs from 4 BG5 PDX mice, Mann-Whitney test), and (R) TM length per cell (n = 62 GBCs from 4 BG5 PDX mice, unpaired t test) under control conditions and perampanel treatment. Data in (E) and (G)–(I) are represented as mean ± SEM.

(S) Representative recordings of neurons in co-culture under 4-μM gabazine (left) and under gabazine plus 50-μM perampanel (right).

(T) Quantification of AP frequency under gabazine and under gabazine plus perampanel (two-sided Wilcoxon matched-pairs test, n = 6 cells).

(U–X) Invasion speed per hour (U), TM branching events per hour (V), primary TM genesis events per hour (W), and small process turnover per hour (X) compared between S24tdTomato (S24-WT) and S24-tdTomato-EGFP- dominant-negative GluA2 (S24-DN) under baseline condition (n = 137 GBCs in S24-WT and n = 112 GBCs in S24-DB in n = 3 independent experiments, Mann-Whitney test).

(Y) Invasion speed per hour, TM branching events per hour, primary TM genesis events per hour, and small process turnover per hour in S24-WT after treatment with perampanel (n = 137 GBCs in S24-WT in n = 3 independent experiments, Wilcoxon test).

(Z) Invasion speed per hour, TM branching events per hour, primary TM genesis events per hour and small process turnover per hour in S24-DN after treatment with perampanel (n = 112 GBCs in S24-DN in n = 3 independent experiments, Wilcoxon test). Effects of perampanel were largely abrogated in S24-DN GBCs as compared to S24-WT GBCs.

Data in (C)–(N) are represented as mean ± SEM.